Karlsruher Institut für Technologie

Liquid metal route for creation of metal matrix composites (MMCs)

Zur Erlangung des akademischen Grades eines

Doktors der Ingenieurwissenschaften (Dr.-Ing.)

bei der KIT-Fakultät für Maschinenbau des
Karlsruher Instituts für Technologie (KIT)

angenommene

Dissertation

von

M.Sc. Mārtiņš Sarma

Tag der mündlichen Prüfung:	17. September 2020
Hauptreferent:	Prof. Dr.-Ing. Robert Stieglitz Karlsruhe Institut für Technologie
Korreferent:	Prof. Dr.-Ing. Egbert Baake Leibniz Universität Hannover

Acknowledgements

This work has been conducted at the Magnetohydrodynamics (FWDH) department of the Institute of Fluid Dynamics of the Helmholtz-Zentrum Dresden - Rossendorf (HZDR). The financial support of the Helmholtz Alliance “Liquid Metal Technologies – LIMTECH” is gratefully acknowledged. I would also like to express my sincere gratitude to everyone who assisted in this research.

First and foremost, I am most grateful to my supervisor Dr. Gunter Gerbeth (HZDR) for his constant support and encouragement throughout this project. Only under his insightful guidance this work could be completed. I am thankful to Dr. Sven Eckert (HZDR) for ensuring an excellent work environment and providing all the necessary support and tools to successfully conduct various experiments.

I would like to express my deepest appreciation to Prof. Dr.-Ing. Robert Stieglitz (Karlsruher Institut für Technologie) for the given opportunity of submitting this work to KIT. Without his comprehensive and rigorous feedback this work would not be publishable. I am also thankful to Prof. Dr.-Ing. Egbert Baake (Leibniz Universität Hannover) for finding the time and patience to be a reviewer.

I am grateful to Dr. Ilmārs Grants (Institute of Physics of University of Latvia) for providing a well defined initial starting point as well as many research ideas throughout the study. His assistance with the theoretical part was invaluable. Furthermore, I am thankful to the team of MHD technology laboratory in Riga: Dr. Andris Bojarevičs, Dr. Toms Beinerts and Reinis Baranovskis as well as Dr. Mihails Ščepanskis (CENOS LLC) with whom the neutron experiments were conducted. Additionally, I am thankful to Dr. Ivars Krastiņš for the many scientific debates. The support by the NEUTRA team in the Paul Scherrer Institute is also greatly acknowledged.

The main results would not be achieved without the extensive and generous support by Dr. Thomas Herrmannsdörfer and the team of Dresden High Magnetic Field Laboratory to whom I am greatly indebted. The provided access to the superconducting magnet system was crucial. I am thankful to Stefan Findeisen from the Department of Mechanical Engineering (FWFM) for the cooperation in the construction of the experimental set-up.

I gratefully acknowledge the assistance of colleagues in the Department of Structural Materials (FWOM) for providing access to sample preparation facilities as well as investigative equipment.

My sincere gratitude goes to various colleagues from FWDH, but I am especially thankful to Bernd Willers and Dr. Dirk Räbiger for their help with different metallurgical tasks and experiments as well as introducing the basics of metallography. Furthermore, I am grateful to Thomas Gundrum, Stefanie Sonntag and Dr. Klaus Timmel for their assistance with preparation and assembly of various experimental activities. I thank Tobias Lappan for never rejecting requests for help and involving me in his research. I am grateful to the best roommate Paolo Personnettaz for the many fruitful discussions.

Lastly, I thank my family and friends for providing the motivation and support throughout this work.

Zusammenfassung

In der vorliegenden Arbeit wird die Möglichkeit der kontaktlosen Erzeugung von Kavitation in Metallen und Legierungen mit hohem Schmelzpunkt wie Eisen, Stahl und Nickel untersucht. Bei diesem Verfahren wird ein konstantes Magnetfeld mit einem magnetischen Wechselfeld überlagert, wodurch Druckoszillationen in der Schmelze entstehen. Im Mittelpunkt der Untersuchungen steht der Einfluss dieser Druckoszillationen auf die Bildung und Stabilität von Mikropartikel-Dispersionen in metallischen Werkstoffen. Metallmatrix-Verbundwerkstoffe (engl. metall matrix composite, MMC) sind vielversprechende Materialien, deren Eigenschaften für den jeweiligen Anwendungszweck maßgeschneidert werden können. Bisher ist die Herstellung solcher Verbundwerkstoffe aufgrund des hohen Schmelzpunkts des Matrixmetalls auf pulvermetallurgische Fertigungsrouten beschränkt. Diese sind zum einen kostenintensiv, und zum anderen mit zusätzlichen Einschränkungen hinsichtlich der Form und der Größe der herstellbaren Werkstücke verbunden. Um neuartige Konstruktionswerkstoffe wie oxid-dispersionsverfestigte (engl. Oxide dispersion strengthend, ODS) oder hochelastische Stähle (engl. high modulus steel, HMS) erfolgreich auf den Markt zu bringen, müssen schmelzmetallurgische Prozesse entwickelt werden. Die Hauptschwierigkeit der schmelzmetallurgischen Fertigungsrouten liegt hierbei in der Agglomeration der mikroskopisch kleinen Partikel im erstarrten Werkstoffgefüge. Mit Ultraschall erzeugte Kavitation in der Schmelze kann Partikel-Agglomerationen verhindern bzw. bestehende Agglomerate aufbrechen. Allerdings ist die Verwendung herkömmlicher Ultraschall-Wandler in hochreaktiven und -korrosiven Hochtemperaturschmelzen praktisch nicht möglich. Daher besteht ein großes Interesse an der Entwicklung eines kontaktlosen Verfahrens zur berührungslosen Kavitation in partikelbeladenen Metallschmelzen.

In der vorliegenden Arbeit werden zunächst die zugrundeliegende Theorie und das Prinzip des Verfahrens erörtert. Anschließend werden praktische Fragestellungen bezüglich der Agglomeration von Partikeln, einschließlich des Einbringens und Dispergierens in der Metallschmelze, untersucht. Insitu-Untersuchungen mittels Neutronen-Radiographie geben hierbei einen visuellen Einblick und folglich ein besseres Verständnis für das Partikelverhalten in einer Metallschmelze. Es werden systematische Experimente zur berührungslosen Kavitation mit dem vorgeschlagenen Versuchsaufbau durchgeführt. Die interessierenden Kavitationseffekte werden in verschiedenen Metallschmelzen, u.a. Zinn, Aluminium und Stahl, beobachtet, und mittels Auswertung der akustischen Signale, welche die kollabierenden Blasen aussenden, eindeutig nachgewiesen. Ferner werden, unter Variation der eingesetzten Magnetfelder, Experimente zum Dispergieren von verschiedenen keramischen Partikeln in Metallschmelzen durchgeführt. Um eine hohe magnetische Flussdichte von bis zu 8 T zu erreichen, werden auch supraleitende Magnete eingesetzt. Die in den Kavitations-Experimenten hergestellten Proben werden metallographisch präpariert und analysiert. Für wachsende Amplituden der kontaktlos erzeugten Druckoszillationen zeigt sich eine klare Tendenz zur verbesserten Dispergierbarkeit der keramischen Partikel in der Metallschmelze.

Abstract

This work investigates the feasibility of a contactless sonication of high melting point melts, such as steel, iron and nickel, using superposition of alternating and steady magnetic fields, focusing on the viability of micro-particle dispersion in these metals. Metal matrix composites (MMCs) are highly prospective materials as their properties can be tailored for specific purposes. Currently production of high melting point composites is limited to solid state routes which are costly with additional limitations of the producible shapes and sizes. To bring new structural materials, such as oxide dispersed strengthened (ODS) steels or high modulus steels (HMS), into the market, liquid state processing must be developed. The main difficulty of the liquid route is particle agglomeration which can be prevented using ultrasonic cavitation. However, the conventional way of using ultrasonic transducer is impractical due to the extreme and reactive environment in the case of high melting point metals. Therefore, it is of high interest to develop a contactless cavitation treatment.

In this work a theoretical argument for the contactless cavitation generation is presented. Furthermore, practical problems regarding particle agglomeration, admixing as well as dispersion are investigated in-situ using neutron radiography giving a better understanding of the particle behaviour in a liquid metal. Then, using the proposed contactless cavitation set-up, cavitation onset is clearly observed in different melts, including tin, aluminium, steel and others, by recording and analysing the signal emitted by the collapsing bubbles. Experiments to disperse various ceramic reinforcements in high melting point metals are conducted in different magnetic fields, employing also a superconducting magnet to reach 8 T. The produced samples are prepared and analysed, and a clear tendency of particle dispersion improvement due to the applied contactless cavitation is shown.

Contents

Nomenclature

Symbols	Description	Unit
$\mathbf{B}$	steady magnetic field	T
$\mathbf{b}_i$	induced magnetic field	T
$\mathbf{F}_B$	flow braking force density	$\mathrm{N\,m^{-3}}$
$\mathbf{F}_{stream}$	streaming force density	$\mathrm{N\,m^{-3}}$
$\mathbf{F}_{osc}$	oscillating force density	$\mathrm{N\,m^{-3}}$
F_r	radial component of the oscillating force density	$\mathrm{N\,m^{-3}}$
F	dimensionless driving force parameter	-
f_r	radial component of the steady force density	$\mathrm{N\,m^{-3}}$
f	frequency	Hz
f_0	fundamental driving frequency	Hz
Ha	Hartmann number	-
I_{AC}	alternating current	A
J_α	Bessel function of first kind	-
$\mathbf{j}_i$	induced current density	$\mathrm{A\,m^{-2}}$
l_c	coil length	m
$\mathbf{n}$	outward directed normal	-
P_A	pressure amplitude	Pa
p	pressure	Pa
p_0	ambient pressure in liquid	Pa
p_v	vapour pressure	Pa
R	time dependent radius of a bubble	m
R_0	initial bubble radius	m
R_B	Blake's radius	m
Re	Reynolds number	-
r_0	radius of the sample	m
r_c	coil radius	m
S	ratio of radius against skin-depth	-
t	time	s
$\mathbf{u}$	velocity vector	$\mathrm{m\,s^{-1}}$
$\mathbf{u}'$	oscillating flow velocity	$\mathrm{m\,s^{-1}}$
u_r, u_ϕ, u_z	cylindrical velocity components	$\mathrm{m\,s^{-1}}$
z_0	height of the sample	m
γ	surface tension	$\mathrm{N\,m^{-1}}$
δ	skin depth	m
η	dynamic viscosity	Pa s

κ	polytropic index	-
$\mu_{n,x}$	attenuation coefficient for neutrons or x-rays	m^{-1}
μ	magnetic permeability of a medium	$\mathrm{H\,m}^{-1}$
μ_r	relative permeability, $\mu_r = \mu\mu_0^{-1}$	-
μ_0	magnetic permeability of free space	$\mathrm{H\,m}^{-1}$
ν	kinematic viscosity	$\mathrm{m}^2\,\mathrm{s}^{-1}$
ξ	coefficient of magnetic field deviation	-
ρ	density	$\mathrm{kg\,m}^{-3}$
σ	specific electrical conductivity	$\mathrm{S\,m}^{-1}$
τ	Reynolds stress	Pa
ψ	unknown potential	-
ω	angular frequency	s^{-1}
ω_0	resonance frequency	s^{-1}

Abbreviations

AC	alternating current
CNR	contrast-to-noise ratio
CTE	coefficient of thermal expansion
DC	direct current
EDX	energy-dispersive X-ray spectroscopy
EMAT	Electromagnetic Acoustic Transduction
FEM	finite element method
FEMM	Finite Element Method Magnetics
HLD	Hochfeld-Magnetlabor Dresden
HMF	high magnetic field
HMS	high modulus steel
HZDR	Helmholtz-Zentrum Dresden - Rossendorf
IFAM	Fraunhofer-Institut für Fertigungstechnik und Angewandte Materialforschung
IPUL	Institute of Physics University of Latvia
LMF	low magnetic field
MHD	magnetohydrodynamics
MMC	metal matrix composite
ODS	oxide dispersed strengthened
PIV	particle image velocimetry
PM	powder metallurgy
PSI	Paul Scherrer Institute
SEM	scanning electron microscopy
SINQ	Swiss Spallation Neutron Source
SPS	spark plasma sintering
UDV	ultrasound Doppler velocimetry
UTS	ultimate tensile strength
YS	yield strength

1. Metal matrix composites - materials of the future

Metal matrix composites (MMCs) first emerged as technologically significant materials in the 1960s in response to a search for improved structural materials for the aerospace industry [1]. Although existing for some time, there is no single and clear definition for a MMC. In general it consists of at least two distinct phases – one being the metal matrix and the other a reinforcement which can be in various shapes, types and sizes [2] – joined together at a "sufficiently fine scale that the result can be considered a material with properties of its own" [3].

The importance of MMCs lies in the high degree of tailorability of the obtainable material properties – they can combine the beneficial features of metals (high electric and thermal conductivity, good mechanical properties and good endurance in harsh environments) with those of the ceramic reinforcement (high strength and stiffness, excellent wear resistance and lower coefficient of thermal expansion). Thereof the industrial usage potential of composites appears endless. Depending on the used reinforcements, additional effects can be obtained, e.g. addition of B_4C does not only improve the mechanical properties, but also adds a high neutron absorption which is relevant in the nuclear industry [4]. This advantage of adjusting the properties of a composite to specific purposes has brought them into attention, and while full market potential is not yet reached they have found a way into many different areas of engineering. Composite materials span from laboratory scale model systems to proper industrial applications. The current as well as potential commercial uses are summarized in Table 1.1.

Composite production methods include powder metallurgy (PM), infiltration as well as spray deposition among others. PM and infiltration have achieved industrial scale usage while most other approaches are limited to experimental and pilot scale set-ups [5]. However, all of the methods have disadvantages and lack the simplicity of casting, which, compared to the other routes, has a significant advantage of low production costs and near-net shape products. Therefore, producing a composite by simply mixing the reinforcement with liquid metal is the most desirable approach. Unfortunately, one cannot simply sprinkle particles on the liquid metal surface and obtain a composite. Such approach is constrained by the fundamental issue of particle agglomeration due to the unfavourable wetting by most liquid metals.

Ultrasonic cavitation treatment during stir casting has been shown to solve the problem of particle clustering [6], [7]. The responsible phenomenon is termed acoustic cavitation. Acoustic cavitation, which is induced by an alternating pressure propagating trough a liquid, differs from hydrodynamic cavitation where the motion of the fluid can lead to a reduction in pressure to the vapour tension level [8] (in this work only the former phenomenon is considered). Generally, cavitation is a periodic expansion and rarefaction,

growth and collapse of cavities inside the melt due to an oscillating pressure field. The event of collapsing can generate extreme local conditions that can break up particle clusters, remove oxide layers as well as force the melt into the small crevices on particle surfaces improving the wetting behaviour in general. The vibrations of the melt are usually induced by a piezoelectric transducer through a metallic or ceramic sonotrode immersed in the liquid metal.

While ultrasonic treatment can be relatively simply applied to light metals, introducing it into a high temperature melt, such as steel, is challenging – any sonotrode inserted into liquid steel will simply dissolve. This has hindered the transfer from experimental to industrial scale of two prospective materials – oxide dispersion strengthened (ODS) steel and high modulus steel (HMS). ODS steels exhibit an excellent microstructural stability for prolonged time in radioactive environments, an essential material property for use in nuclear power plants [16]. HMS can allow to reduce the weight of different transportation systems by increasing the specific stiffness while retaining the strength and ductility [17], thus, reducing the energy consumption, be it electric or combustion. Significant research effort has been made to reduce the production costs and complexity and enable industrial manufacturing of these materials, however, considerable challenges remain.

Table 1.1.: Overview of current industrial applications of MMCs. Table adapted from [9].

Application	Required properties	Main material systems
Aerospace (aeronautical and space systems)		
– Stringers, ventral fins, blade sleeve and swash plate in helicopters, support struts, fan exit guide vanes [4]	High specific strength and stiffness, resistance against thermal and mechanical loads, fretting resistance	continuous – Ti/SiC and discontinuous – Al/SiC
– Frame and rib struts, landing gear in Space Shuttle, high-gain antenna boom for Hubble telescope [1]	High specific strength and stiffness, low thermal expansion coefficient, good electrical conductivity	continuous – Al/B, Al/C and discontinuous Al/SiC
Ground transportation (automotive and railroad)		
– Pistons, cylinder liners, driveshafts, piston connecting rods, intake and exhaust valves, brake drums, disks and rotors [10],[11]	High specific strength, stiffness and modulus, wear and fatigue resistance, reduced thermal expansion with increased thermal conductivity	Al and its alloys/SiC-Al_2O_3, Al/Si/Al_2O_3, Ti/TiB_2 – both continuous and discontinuous
Electric power and electronic industry		
– Power transmission cables [12]	Vibration and fatigue resistance, high electrical and thermal conductivity	Al/Al_2O_3 continuous fibres with Al-Zr wires
– Electronic packaging and thermal management, e.g. microwave packaging, thermal cores, heat sinks, power semiconductor modules etc. [4],[13]	Tailorable thermal expansion and high thermal conductivity, low density	continuous – Al/C, Cu/C, Al/B discontinuous – Al/SiC, Cu/SiC, Al/BeO, Be/BeO
– High magnetic field applications, e.g. high field research, thermonuclear fusion reactors, levitation, magnetic resonance [2]	Superconductivity (higher operating temperature is advantageous)	Cu/Nb_3Sn, Cu/Ti-Nb
Other applications		
– Recreational and sporting goods [2],[14]	Increased specific stiffness, increased wear resistance	Al alloys/Al_2O_3, Al/SiC
– Wear resistant materials for processing, e.g. drilling, cutting etc. [2]	High wear resistance	Metal with carbide particles – WC, TiC, TaC
– Smart composites, i.e. internal damage detection, performance monitoring etc. [15]		Optical fibre in Al/SiC

1.1. Objectives of the current work

To reach the goals of a sustainable future, new, high performance materials are a necessity. Steel being the main structural material and used in various industries, from transport systems to energy production, can particularly be modernized – improving its functional properties while reducing the density is an especially desirable outlook. Furthermore, future prospects of fusion reactors demand high-performance materials that can sustain the extremely high temperature and oxidative environments. Innovation of production methods is the key in bringing these materials to the market. In this thesis first steps are taken to make an alternative steel composite production method a reality. This brings to three research questions, starting from understanding the fundamentals.

1) How ceramic particles behave in a liquid metal flow and what affects their dispersion and entrapment in the matrix?

The high melting temperatures and opaqueness of liquid metals limit the investigation possibilities of particle laden flows. In such cases X-ray imaging can be used, however, a high density ratio between the liquid and the particle is needed to have a good contrast. Yet, to answer the first question, it is of significant interest to understand how lower density particles (the reinforcement phase) interact with the liquid metal flow (the matrix phase). Neutron radiography is a promising imaging technique that fulfills the necessary requirements and can provide an insight into the required conditions for good particle dispersion, particle capturing during solidification and the flow conditions for particle admixing. Therefore, in this work neutron radiography is employed to obtain a better understanding of particle behaviour in liquid metal flows.

2) Can ultrasonic cavitation be created in a contactless way in high melting point metals?

A set-up that can generate cavitation in a contactless way has been presented by Grants et al. [18]. A steady 0.5 T strong magnetic field was applied axially to a cylindrical workpiece that is heated by electromagnetic induction. Superposition of both magnetic fields induces an alternating radial magnetic body force in the melt resulting in an oscillating pressure field. This pressure variation is responsible for the cavitation activity. The set-up has been demonstrated on a proof-of-concept scale. Now systematic experimental research is performed to investigate the possibility of extending the use of the proposed set-up to high melting point metals, such as steel, iron and nickel, and generate cavitation in them.

3) How does the cavitation influence the particle dispersion in high melting point metals?

Different composites using various particle-matrix pairs have been produced using the cavitation treatment. Special emphasis is put on Ti- and Zr- compounds as part of the ultra-high-temperature ceramics family. In addition, a new set-up is constructed for use in a superconducting magnet with a theoretical limit of 19 T. This provides an increase of the achievable acoustic pressure amplitude in the melt by a factor of 30 compared to the initial experiments. The produced samples using different cavitation intensities are compared and a general tendency can be postulated allowing to show the potential of the proposed contactless cavitation treatment. It must be noted that a more narrow scope of the whole composite family has been chosen – the reinforcement phase is limited to micron-sized particulates. Nanoparticles are excluded in this first step, as it would introduce an additional level of complexity. Nevertheless, if the approach is proven to be successful, then also nanocomposites, in principle, can be produced in the same manner.

1.2. Organisation of the thesis

Chapter 1 introduces the motivation of the work and postulates the research objectives of the thesis. Furthermore, a brief overview of the field of MMCs, their applications and challenges in fabrication thereof is given.

Chapter 2 provides a review of the state of the art regarding MMCs properties (with focus on particulates) and production methods. Furthermore, introduction to the acoustic cavitation phenomenon and its usage in MMC production is given. The problems regarding cavitation introduction in high temperature melts are identified and a possible solution in the form of contactless sonication is presented.

Chapter 3 gives a theoretical argument for the feasibility of the proposed system. This part describes and provides estimates for the electromagnetic forces, magnetohydrodynamics and bubble dynamics in the system. Simplified solutions are sought where possible.

Chapter 4 is dedicated to introducing neutron radiography as means of visualizing the multi-phase flow and particle entrapment by the matrix. Two different sets of experiments are presented and discussed. Firstly, conditions for successful particle admixing are investigated, followed by the analysis of melt solidification and the entrapment of the particles in the matrix.

Chapter 5 presents the used contactless cavitation set-ups, the concept of cavitation recording and the signal analysis. It then continues with testing the principle of cavitation recording, presents a visible example of the cavitation effect in the form of flux-less soldering and discusses different experiments where cavitation treatment is applied during processing of MMCs.

Chapter 6 gives the rationale of specific particle/matrix choices and the sample characterization procedure. The last sections are devoted to presenting and comparing some of the produced composites and identifying the main tendencies of the impact of cavitation treatment on high melting point metal matrix composite production.

Chapter 7 presents a summary of the work highlighting the main conclusions and giving recommendations for future research on the topic.

2. Beneficial properties and fabrication routes of metal matrix composites

2.1. Properties of MMCs

The addition of high modulus reinforcement to a metal matrix can change and improve its physical properties. The important advantage is that, if the reinforcement phase has lower density than the matrix, the composite's density will be reduced as well. Heat capacity can be described the same way. In fact, these physical properties follow a simple rule of mixtures, e.g. $\rho_c = \rho_m V_m + \rho_r V_r$ where ρ and V are density and volume fraction of matrix m and reinforcement r phase, respectively. For an overview of similar formulas for conductivity and thermal expansion one can refer to [19]. In general, as these properties have higher values for metals than ceramics, addition of the second phase decreases the respective property with increased volume percent.

Still, the most important features for structural applications are strength and stiffness, as well as ductility. The four main mechanisms that explain the improvement of mechanical properties, assuming perfect wetting between the reinforcement and matrix, are quench strengthening, Orowan strengthening, grain strengthening and increased work hardening [20], [21].

Since ceramic reinforcements and the metal matrix have a large difference in coefficient of thermal expansion (CTE), when the composite is cooled, slip dislocations are generated at the interfaces. Orowan strengthening relates to resistance of bypassing the dislocations by closely spaced particles – a larger applied stress is required to force a dislocation around a precipitate (or a ceramic particle) than without any reinforcement. However, it is negligible if particles are larger than 1 μm and have large interspatial distances. Grain boundaries hinder the movement of dislocations which contributes to the yield strength (YS). During crystallization of the matrix, the particulates may act as nuclei sites, and, in theory, it can be assumed that each particle nucleates one grain. Additionally, particles can pin the grains. The presence of particulates increases the amount of generated dislocations during work hardening as they tend to form between the interfaces of the matrix and second phase particles. Lastly, ductility will be reduced with increased volume fraction of the reinforcement (as a brittle phase is introduced in a ductile matrix), but the effect can be diminished using smaller reinforcements as they tend to cavitate less. Some examples of composites showing substantial improvement in mechanical properties over the corresponding matrix material are given below.

Sharifi et al. [22] have studied the mechanical and tribological properties of B_4C nanoparticle reinforced pure Al. With hot pressing the powders, bulk nanocomposite samples with 5, 10 and 15 wt% B_4C have been prepared. It has been shown that the mechanical

properties follow the general trend – increased content of the reinforcement increases the hardness and ultimate compressive strength while decreasing the ductility. Using the third hardest room temperature ceramic with density of only 2.5 $g\,cm^{-3}$, an impressive increase of hardness to 164 HV and compressive strength to 485 MPa compared to 33 HV and 130 MPa of pure Al, respectively, has been reported.

Thermal management components need a low CTE and high thermal conductivity. Copper has excellent thermal conduction properties, yet its CTE is four times higher than for silicon. However, SiC or diamond reinforcements can be used to adjust the properties of copper. This is exactly what Schubert et al. [23] have done – 40% Cu/SiC and diamond composites have been successfully produced by using hot pressing of the powders. Using SiC particles the CTE has been lowered from 17 to $11 \cdot 10^{-6}\ K^{-1}$, while the thermal conductivity decreased from 380 to $300\,W\,m^{-1}\,K^{-1}$. With diamond the CTE has been similarly lowered to $11 \cdot 10^{-6}\ K^{-1}$, but the thermal conductivity increased to a stunning $639\,W\,m^{-1}\,K^{-1}$.

The mechanical properties of Ti can also be improved. For example, Gorsse et al. [24] have successfully produced 20 and 40 wt% TiB whisker reinforced Ti-6Al-4V alloy in-situ using hot isostatic pressing, both with randomly aligned and directional (obtained with extrusion) whisker reinforcement. While unreinforced alloy has a Young's modulus of around 109 GPa, the reinforced composite reaches remarkable 169 GPa (20 wt%) and 205 GPa (40 wt%) along the extrusion direction.

Chen et al. [25] have managed to create a Mg alloy composite with a dense and uniform 14 vol% high concentration of 60 nm large SiC nanoparticles by evaporating a Mg-6Zn ingot with 1 vol% SiC. Surprisingly no clustering of SiC has been observed due to particle self-stabilization – while van der Waals forces would try to keep the particles clustered, the high thermal energy of the nanoparticles allows them to escape the attracting force. A spectacular increase in YS (716 MPa compared to 500 MPa for unreinforced) and in Young's modulus (86 GPa compared to 44 GPa) has been reported. The strengthening, most likely, is due to the high density of the nanoparticles and the very strong interfacial bonding (1250 MPa) between the particles and the matrix.

A new class of nano-structured steels have been presented by Springer et al. [17]. Roughly 50 – 200 nm large TiB_2 nanoparticles have been successfully synthesized inside liquid Fe, which then is spray formed and hot rolled. The composite shows greatly improved mechanical properties due to the refined particles and the small grain size (around 400 nm). The obtained mechanical properties are astonishing - YS reaches 800 MPa, while Young's modulus 236 GPa with a reduced density compared to conventional steels.

In general, steel has a high Young's modulus and YS, which, combined with a low production cost (see material property charts in [26]), makes it an important structural material. However, steels also have a high density. Clearly, if one looks for a strong, but light part, and if the price is not the main drawback, e.g. for sophisticated products in defence and aerospace industries, then Al MMCs can outperform steels by a large margin. Still, if successful dispersion of less dense particles would be possible, steel becomes increasingly more attractive. The material property Figure 2.1, adapted from [26], can help visualize the possible improvements – Young's modulus is shown for particle reinforced MMCs and different alloys. For comparison, the previously reported nano-structured steel

[17] as well as values for different vol% TiB_2 reinforced steels reported in [27] are added as well.

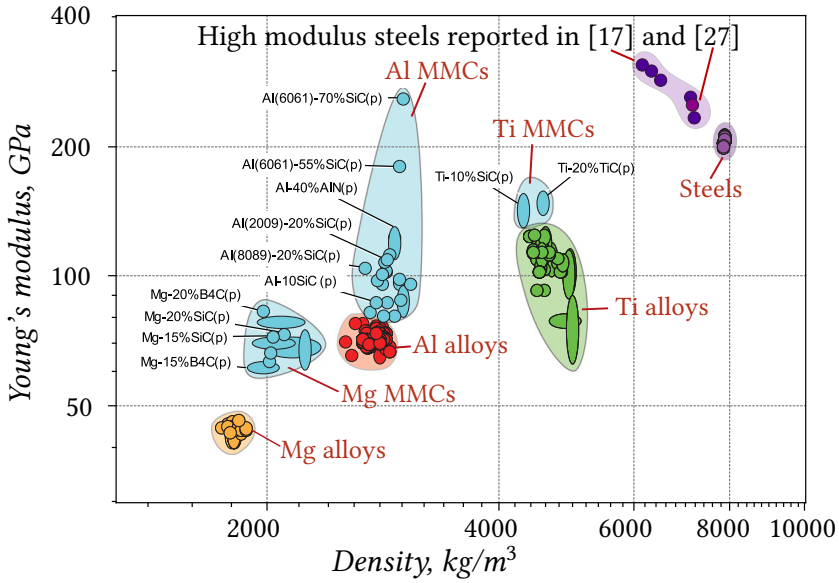

Figure 2.1.: A comparison of the Young's modulus versus density of MMCs with other structural materials [26]. Values from particle strengthened steels reported in [17] and [27] are shown as well.

The material class introduced last is termed high modulus steels (HMS). The interest stems from the automotive industry, where there is a demand to reduce the weight of the vehicles in order to reach the new emission targets of CO_2. The main challenge is to increase the strength while reducing the density. However, in the automotive industry, most parts are produced to support load without plastic deformation, thus ultimate tensile strength (UTS) becomes less important than YS. Additionally, stiffness becomes important, which usually is lowered with the presence of strengthening defects [17]. Adding lightweight, but stiff particles to a metal matrix is a solution, e.g. TiB_2 which has stiffness of 565 GPa, but density of 4.52 g cm^{-3}. The main problem is the particle microstructure and dispersion. For example, if particles are created in-situ, then size, morphology and dispersion can be affected by solidification kinetics, alloying conditions or changing the microstructure of matrix itself. These changes, however, can decrease the stiffness [28]. In order for HMS to become industrially more competitive with light metal alloys, it is important to improve production processes and, essentially, find a way to disperse the particles in steel.

A different material class is precipitation hardened metals, where dislocation motion is impeded by forcing them to bow around an obstacle, thus, higher load is needed for deformation. Usually the impediments are nano-sized oxide particles. In this case, an additional advantage is increased creep strength for the composite since oxide particles have high thermal stability. If the matrix is steel, then an ODS steel is produced. With its excellent mechanical properties and structural stability in elevated temperatures, it is considered the most promising material for use in the next generation nuclear power

environments. As a reinforcement, usually yttria (Y_2O_3) is suggested, as it is one of the thermodynamically most stable materials. On a laboratory scale, materials with good properties have been produced. For example, using the PM route it is possible to obtain uniform dispersion of 5 nm 0.3 wt% Y_2O_3 in a steel matrix [29]. However, the production routes are a clear obstacle for commercialization. While the PM route works on a small laboratory scale, a production process to create a 2m x 2m large panel can only be theorized [30]. Different production routes besides PM are proposed – from physiochemical to additive manufacturing to internal oxidation. Yet, it is clear that a pure casting route, if possible, would be the best for upscaling to industrial production [31].

2.2. Processing of MMCs

Processing of MMCs can be divided in three parts – pre-processing, primary processing and secondary processing. Pre-processing involves preparing the metal matrix (in bulk for melting or powder form for PM routes) and the reinforcements, and for some processes it also means arranging the reinforcements, e.g. prior infiltration. Primary processing is the main phase of creating a composite – it is the act of combining both materials, i.e. the reinforcement and the matrix material, together and it can be done by different means. The secondary processing is the last step in which the composite is shaped, hardened, deformed, machined, etc. The two main MMC fabrication methods are liquid state and solid state processing [3].

2.2.1. Solid state processes

The main advantage of the solid state processes is the minimal chemical interaction between the matrix and the reinforcement. This allows mixing of reactive metals, e.g. Ti, and high melting temperature metals, like Fe or Ni, with reinforcements which otherwise would possibly react or diffuse. Other benefits include possibility to combine various reinforcements in the same matrix, use non-equilibrium matrix alloys and easily achieve high volume fraction of the reinforcement [32]. Usually the production also aims for near net-shape end products.

As the solid matrix material must be placed in-between every pair of the reinforcement, production of composites using a solid state route is complex. At first the reinforcement has to be blended together with the matrix using ball milling, followed by densification of the mixture with cold (isostatic) pressing and sintering or hot (isostatic) pressing and finalized by some sort of forming, i.e. extrusion, forging, rolling. The reinforcement phase slows down the densification as the ceramics do not sinter at the same temperature as metal sinters. Speeding up the process is possible by partly melting the matrix, but that creates additional problems with possible chemical reactions. Many different and complicated approaches for production exist, but discussing all of them is beyond the scope of this work. For general overview of processing, the reader is referred to [32] and [33].

Besides the complexity, solid state routes have other critical shortcomings, such as

- high costs of the production,

- high costs of the bulk material and its storage,
- many intermediate steps, e.g. blending, degassing, compacting with sintering during or after, extrusion,
- hard to produce composites with anisotropic reinforcements because of possible fractures (and impossible with continuous reinforcements),
- difficulty to produce large and complex shapes.

These issues drive the current research for alternative production methods.

2.2.2. Liquid state processes

To create composites using anisotropic as well as equiaxed reinforcements, mainly liquid production routes are employed. These can be divided into three dominating processes: infiltration, stir casting and spray casting. It is worth mentioning in-situ processing where the particles are synthesized in the melt from chemical reaction between specific compounds (usually salts). Also liquid metal additive manufacturing is a significant, but very novel topic with many unresolved processing and manufacturing issues. The main advantages of liquid state processes are the fast, low cost manufacturing as well as the ability to directly produce large and complex shapes/products.

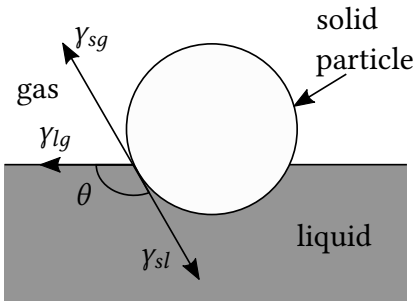

Figure 2.2.: Schematic of contact angle θ between a solid particle and liquid and gas phases [34].

Nevertheless, some difficulties arise with liquid metal processing. The high surface tension of liquid metals does not favour the process – metals usually do not bond with non-metal systems, i.e. "molten metal beads up instead of coating or wetting the surface of most reinforcements" [3]. However, a good wettability is a prerequisite attribute for composite production that also ensures the required strong interfacial bond between the melt and the reinforcement phase. A good wetting between solid and liquid can be observed when the adhesive forces exceed the cohesive forces between the liquid molecules. The measure of wettability is given by a contact angle θ between the solid and liquid, as shown in Figure 2.2, governed by Young's equation,

$$\gamma_{sg} - \gamma_{sl} = \gamma_{lg} \cos(\theta) \ , \tag{2.1}$$

where γ_{sg}, γ_{sl} and γ_{lg} are the surface tensions between solid-gas, solid-liquid and liquid-gas interfaces, respectively [34]. A good wettability is obtained if $\theta < 90°$, while a contact angle larger than 90° implies a non-wetting system.

The wetting can be either non-reactive or reactive. Most often metals have a weak wettability with ceramics (contact angle around 90°) or they do not wet at all due to the high surface tension of metals as well as the presence of thin oxide layers on the surfaces. Such property considerably complicates production of MMCs. To improve the process, the reinforcement phase can be coated with a metal beforehand, thus replacing the interface from metal-ceramic to metal-metal. The matrix can also be alloyed with additional elements that can promote reactions between the phases, reduce the surface tension of the melt and/or disrupt the oxide layer [35].

If wettability is of reactive nature then it will also be time and temperature dependent, with wetting improving over time due to chemical reaction taking place until a thermodynamic balance is achieved. The high temperatures usually encountered in liquid metals also facilitate the reaction rate. On the other hand, higher temperature can reduce the amount of adsorbed gases from the ceramic surfaces. Strong reactions between the phases, however, are undesirable as that degrades the strength of the reinforcement. To overcome the non-wetting behaviour without changing the chemical composition of the material, simple mechanical forces can be used, e.g. stirring of the melt. Furthermore, it is favourable to simply use compatible metal matrix-ceramic pairs and limit the contact time between the melt and the reinforcement.

2.2.2.1.Infiltration

Using infiltration complex shapes can be created as the metal flows trough a mould. The liquid metal, using inert gas or a piston, is forced trough a porous preform of desired shape which is made from the ceramic reinforcements (continuous or discontinuous fibres, particles). The main advantage is the possibility to produce high volume fraction ($40-70\%$) composites. Additionally, the high pressure infiltration using vacuum ensures that the porosity is small. However, the non-wetting of the ceramic stays as the main issue. It can be improved by coating the reinforcement, using higher temperatures or extending the processing time. These solutions might solve the problem, but they also can create unwanted interfacial reactions. Other disadvantages include the difficult preprocessing step of creating the preform and ensuring the microstructural uniformity. Furthermore, possible contact between the reinforcement phase must be avoided as it can degrade the properties of the composite [3].

2.2.2.2.Spray deposition

Spray deposition is seen as a very promising method, e.g. oxide nanoparticles have been successfully dispersed in steel [36]. It is based on atomizing a stream of liquid metal and injecting the reinforcement phase in such a way that it is captured by the liquid metal stream and both phases deposit together on a cooled substrate. One of the main advantages of the spray casting is the short contact time between the liquid metal and the reinforcement which permits the use of reactive metals. Additionally, the rapid

solidification of the composite allows to achieve very fine microstructure. While it sounds promising, the free forming nature of the process makes it difficult to simultaneously control all of the variables [33]. Furthermore, a large amount of material (can be as high as 30%) can be lost due to overspray.

2.2.2.3.Casting

One of the reasons why MMCs have not taken a larger market share is the difficulty to use a simple casting route, i.e. straightforwardly sprinkling the ceramic powder on a liquid metal surface will not create a composite.

All of the previously mentioned problems apply directly to a casting process. Pushing of the reinforcement by the solidification front is an additional issue that may arise. This is not a problem in infiltration processes as the reinforcement cannot move freely which limits the grain size of the matrix. However, in casting processes, where the particulates can float around, the growing dendrites will push the reinforcement until some saturation is reached. This can create segregated reinforcement regions which lower the mechanical properties of a composite.

The addition of a reinforcement also significantly raises the viscosity of the melt which adds an additional problem for casting. Because of the higher viscosity the gas will rise slower, thus, making the degassing more difficult and higher energy has to be provided for mixing the melt [3].

Nevertheless, the disadvantages of a casting route can be solved. The undesirable reactions between the molten metal and reinforcement can be avoided if a stable metal-ceramic pair is found. The high surface tension of liquid metal which prevents the insertion of ceramic can be counteracted by an intense stirring using an impeller or electromagnetic forces. Furthermore, the stirring aids with the dispersion. Particles can also be introduced in the form of a master alloy. The last obstacles – weak wettability and particle agglomeration – can be solved with ultrasonic processing.

2.2.3. Ultrasonic processing of liquid metals

Metallurgical application of ultrasonic treatment of metals has been researched since the 1930s and by the middle of the 1960s it was proven that the microstructure of a material can be improved with sonication. The processing and benefits of ultrasonic treatment are well known, and, especially for light metals, one can refer to the fundamental work of Eskins [7]. Only a short overview will be given here. Additionally, a theoretical description of the cavitation phenomenon with regard to the current work can be found in section 3.3.

Ultrasound processing helps with degassing, filtration and grain refinement [7], [37]. Still, the most relevant feature for the current work is the possibility to break up the reinforcement agglomerates and improve the wetting by the matrix [38], [39], [40]. The governing phenomenon of ultrasonic treatment is acoustic cavitation – “a creation of new surfaces or expansion/contraction/distortion of pre-existing ones in a liquid” [41] in response to an imposed time varying pressure field.

Every unfiltered liquid will contain entrapped gas or vapour in some form. Depending on the ambient pressure, applied pressure and other conditions, as well as the cavities size

(larger or smaller than the resonance size), the gas pocket (a bubble) will undergo expansion and compression phases. This response may be gentle or violent. These processes are termed steady or stable and transient cavitation, respectively. In steady cavitation bubbles oscillate non-linearly around some equilibrium size. In transient cavitation the bubbles may exist even for a shorter time than a full acoustic cycle. During the expansion cycle the bubble will grow swiftly many times its original size while during the compression cycle the bubble will implode, usually creating more bubbles that allows the process to repeat [42]. It must be noted that, unlike in water, liquid metals have no free floating bubbles as any gas will be usually completely dissolved. In this case, the solid inclusions inside the liquid, e.g. micro sized, badly wetted oxides, act as potential cavitation nuclei sites as the cracks and crevices of the body will be filled with gas [7].

An important role is played by different cavitation thresholds: when a cavity or bubble oscillates around equilibrium size (stable cavitation threshold) and when a cavity exists only for a single pressure cycle, during which it grows many-fold and collapses violently during compression phase (transient cavitation threshold). These thresholds, however, depend on many variables, e.g. ambient pressure, applied pressure, bubble radius, oscillating frequency, etc. In other words, a threshold can be defined in terms of one of the parameters by keeping others constant, e.g. cavitation can switch from stable to transient to stable by increasing the excitation pressure, thus, an upper and a lower bound exist where the transient effects can take place depending on the applied pressure, but independent of the bubble size [43]. This brings uncertainty about when the cavitation can be reached in specific liquids. Cavitation also is a measure of purity of the liquid, i.e. how much impurities and gas is there – in very pure liquids the cavitation threshold may approach or even equal the tensile strength of the liquid [44]. In reality it is not possible to predict the amount of inclusions in liquids, especially in liquid metals. Thus, taking into account the previously mentioned uncertainties, predicting the inception and strength of the cavitation is almost impossible.

The growth of bubbles can also happen in undersaturated liquids by rectified diffusion. Usually, in an undersaturated liquid, the gas bubbles will slowly dissolve. However, because of the oscillating pressure, the bubbles are forced to vibrate around an equilibrium radius, and two effects – area effect and shell effect – prevent the dissolution and can cause growth. When a bubble contracts, the gas concentration increases and it diffuses from the bubble, while during the expansion the opposite process takes place. Additionally, during the bubble expansion, the liquid shells around it are compressed. The gas concentration gradient across such a shell towards the bubble is higher than in equilibrium size, i.e. more gas diffuses inside the bubble. As the diffusion rate is proportional to the area, more gas will enter than leave, and over one cycle there will be a net increase of gas concentration in the bubble. This permits the growth of small bubbles, which can possibly reach the resonant or threshold sizes [45].

The formation, expansion, pulsation and rapid collapse of the bubbles within the liquid can create very extreme local conditions – "hot spots" [46] where temperatures in some cases have been measured up to 5000 K [47], pressure reaching 1000 atm and cooling rates above 10^{10} K s^{-1} [48]. Besides the hot spots, the collapse produces high-speed jets in the range of 200-1000 m s^{-1} with a local impact pressure in the GPa range [49] – this is most likely responsible for the erosion of surfaces, fragmentation of dendrites and agglomerates

and other effects. It has also been shown [50] that the dendrites can be fractured even by steady cavitating bubbles. Thus, it is clear that the cavitation phenomenon has the ability to create drastic changes in a metal microstructure.

The most straightforward way to introduce the cavitation into a liquid metal is by directly inserting a sonotrode into the melt. The main difficulty is to find a stable material sustaining the elevated temperatures. For instance, Nb and its alloys are suggested for use with Al [7], also steel and Ti have been tried, but they tend to react with Al more easily. It is possible to use ceramic sonotrodes, but that increases the production costs substantially. Some recent investigation has also been done with coating a metallic sonotrode with a ceramic layer, and while it allowed to protect the sonotrode against the corrosion by liquid metal, the layer erodes by the cavitation damage [51].

A more complex route is to introduce the cavitation indirectly. There are reports of using consumable sonotrodes, vibration of the mould and other methods [52], but the focus on this route is currently minimal. However, that is the only way to process high temperature materials, thus, for this reason, the application of cavitation is primarily limited to the conventional direct route in aluminium and its alloys followed by magnesium and its alloys.

Still, by using direct ultrasonic processing, i.e. sonotrode in the melt, different reinforcements have been successfully dispersed, and good improvements of the mechanical properties of aluminium and magnesium have been reported.

It has been shown in [53] that the addition of 0.8 wt% carbon nanotubes to Al-7Si-Mg (A356) alloy has increased the microhardness, UTS and Young's modulus by 27.8%, 17% and 29.2%, respectively, compared to the pure alloy. The composite has been created by applying 20 kHz ultrasonic vibration to the melt, and the best results have been achieved with a power output of 2.1 kW as increased power leads to coarsening of the microstructure. Yet, fibres make only a small fraction of all reinforcement types. In fact, particulates, both micro- and nano-sized, are the main type as demonstrated by the following research.

Powder metallurgy can be combined with ultrasonic treatment as shown in [54] and [55] where high-energy ball milling is combined with ultrasonic vibration. In [54] magnesium alloy (Mg–2.8Al–0.8Zn–0.3Mn – AZ31B alloy) has been reinforced with 3, 5 and 10 vol% 0.5 µm SiC particles using semi-solid stirring assisted by ultrasonic vibration. As the particle amount increases the mechanical properties follow the trend – UTS and YS increase by 30% and 60% with the highest particle amount, but Young's modulus increases by 33%. Similar routine is used in [55] to create A356 alloy composite strengthened with 40 nm SiC particles. Firstly, granules from mixture of SiC and Al are created and then remelted with the alloying metals. At the last step the melt is treated with ultrasound for 2 minutes. It is shown that even 1 wt% of SiC can increase the UTS by 19%. It is assumed that the uniform distribution is due to the ultrasonic treatment.

Ultrasonic processing of the material can also bring improvement to material properties when applied to in-situ created composites as shown in [56], [57], [58] and [59]. In [56] Al-Mg-Cu composite is reinforced by in-situ created nano-sized Al_2O_3. All the components are melted together in a crucible and after intensive stirring, ultrasonic vibration is applied for 5 minutes. By comparing the resulting composite with one without ultrasonic processing, it has been concluded that the grain size of the alloy matrix reduces from 120 µm to 50 µm. Additionally, the grains consist of less branches and have shorter arms. Lastly, it has been

shown that Al_2O_3 can be produced in-situ by displacement reaction of Al and CuO, and, due to ultrasonic processing, the particles are evenly dispersed inside the grains which significantly increases the YS by 43%, UTS by 32%, hardness by 13%, and, surprisingly, even improves the ductility compared to composites without ultrasonic processing.

Similar results are reported in other works. Either Al [57], [58] or Mg [59] alloy is used as matrix material which is melted together with specific salts to create either TiB_2 or MgO and Al_2O_3 particles, respectively. The mixtures are stirred to facilitate the mixing and reaction with the final step being the application of around 20 kHz ultrasound which lasts from 1 to 5 minutes. The end result is the same – ultrasonic processing results in de-agglomeration and dispersion of particles which leads to drastic increase of the mechanical properties (UTS and YS increases in ranges from 30 to 100%). It is worth underlining that increased wt% increases the strength [57], [59]. Lastly, it is also shown that extended processing times eliminate more and smaller particle agglomerates [59].

Ultrasonic processing truly shines when applied to simple casting route (with mechanical or electromagnetic stirring as well as without) with micro sized particles [60], [61], [62], with micro and nano sized particles [63] and with nano sized particles [6], [64], [65]. The production is relatively straight forward – Al or Mg alloy is melted in a crucible in a resistance furnace. If the melt is stirred, the particles are added during this phase, otherwise particles are fed during the sonication and the stirring is provided by acoustic streaming. Ultrasonic treatment with frequency around 20 kHz is applied for 15 to 90 minutes. After the processing, the melt is solidified in the crucible or poured into a mould and solidified. The effect on the mechanical properties and microstructure is investigated for SiC [60], [61], [62], [64], Al_2O_3 [65] and B_4C [63]. While each experiment has its uniqueness, the conclusions are similar – the particulate agglomeration is much smaller with ultrasonic treatment [60], [64] (in fact, according to [62] the SiC crystal refinement scales with increased amplitude of the ultrasonic tool). Essentially, the reinforcements are nearly uniformly distributed by high intensity ultrasonic treatment [65], [64] allowing creation of composites using the liquid metal route. Besides that, it has been shown that the acoustic streaming from the sonotrode efficiently traps the nanoparticles into the melt from the surface [6]. Overall, all produced materials show greatly improved mechanical properties over unreinforced ones, with highest improvement coming from nanocomposites [63].

2.2.4. Path to contactless cavitation

The main matrix material currently, both in research and production, is aluminium followed by magnesium, i.e. light metals, for which ultrasonic treatment can be easily implemented. In contrast, the production of steel composites with current production methods is complicated. As mentioned, powder metallurgy is the preferred way of producing ODS steels, but it has the disadvantages of being expensive and having size and shape limitations. HMS can be produced in-situ, however, they are limited by the usable compounds. Steel casting is the preferable manufacturing route, but the production of composites in this way is hindered by the particle agglomeration and segregation. The solution that works for the light metals cannot be applied to steel or any other high

melting point or highly reactive metals – there is no sonotrode that can withstand the harsh environment.

Instead the solution can be sought in the form of an important metallurgical principle – controlling of liquid metal in a contactless way using electromagnetic forces. It is well known that liquid metals are both melted and stirred in an induction furnace [66]. The flow can also be controlled by using permanent magnets [67]. The Lorentz force that arises sets the liquid in motion which can help homogenizing the temperature, and, if the flow is strong enough, can bring the floating particles into the melt and help with the particle dispersion [68]. Still, for production of composites a major challenge remains – particle agglomeration has to be prevented.

In 1996 Vivés [69] provided an initial solution for the problem. In his work, he has studied the effects of forced vibrations produced by electromagnetic forces that can initiate the cavitation phenomenon in a contactless way. The working principle is simple – a stationary magnetic field is applied to an aluminium alloy in a rectangular parallelepiped vessel. In addition, a sinusoidal current flows trough the alloy perpendicularly to the steady magnetic field. The interaction between both fields gives rise to a periodic electromagnetic force which sets the melt into vibration and, in turn, generates pressure. This oscillating pressure has been shown to produce cavitation. As the process is based on electrodes having direct contact with the liquid metal, it is still difficult to directly apply this principle to high temperature metals. Additionally, it has been shown that the crucible and the electrodes are rapidly eroded by the exploding cavitation bubbles which can lead to unnecessary contamination of the alloy.

In 2009 [70], with an improvement in 2016 [71], a method for high magnetic field non-contact treatment of conductive materials was patented by scientists from Oak Ridge National Laboratory. Electromagnetic Acoustic Transduction (EMAT) uses the same principle as Vivés system, but the main difference lies in the way the induced current is created – an induction coil is used in EMAT which makes the process truly contactless. However, the system requires a conductive, e.g. steel, crucible to facilitate the cavitation, as the container's vibration is the main source of the phenomenon at higher frequencies due to the thin skin depth. Thus, this method is difficult to employ for high temperature, reactive melts or if the melt is the same material as the crucible.

A different approach that employs electromagnetic forces is suggested by Bojarevics et al. [72]. They use a system of primary and secondary coils. The movable primary coil is responsible for inducing strong vibrations in the melt at double the frequency than that of the coil current, which then creates cavitation. Meanwhile the secondary low frequency coil generates the heating as well as the stirring of the volume. As the primary coil is lowered, it repels the free surface and rises the metal around the coil which increases the region of the vibrations. Yet a simple disadvantage exists – the effective cavitation region is limited to the vicinity of the coil.

All methods of contactless magnetic sonication have shown to create cavitation in light metals – the effects on the material microstructure are comparable to that created with mechanically excited ultrasound. To facilitate the same phenomenon in high melting point metals, in 2015 Grants et al. [18] proposed a system similar to EMAT with an important difference – by employing concept similar to floating zone condition, a crucible is not necessary. In such case the molten part is in contact only with holders from the same

material, thus, no contamination is possible, making it a truly contactless system suitable for high melting point metals. The working principle is as follows – a steady 0.5 T strong axial magnetic field is applied to a liquid metal part heated by induction currents. The superposition of both fields creates an alternating Lorentz force that produces pressure oscillations. If they are sufficiently strong, the cavitation can be created. The proposed system has been tested and the cavitation phenomenon has been successfully observed with different light metals, i.e. Sn, Zn and Al. The follow-up question of sonication of high melting point metals and subsequent dispersion of particles with such a set-up has been addressed and explored in the present work.

3. Theoretical assessment of the feasibility of contactless cavitation caused by magnetic fields

In the following chapter a simplified description of the relevant electromagnetic forces (section 3.1) as well as magnetohydrodynamic (MHD) phenomena (section 3.2) for the contactless cavitation set-up is given. In the last part (section 3.3), some basic considerations about a single oscillating bubble and the potential of initiating cavitation in liquid metals are presented. It is important to note that the considered problems contain various simplifications in order to extract main tendencies on the relevant phenomena and not to solve full-scale problems. As such, direct comparison between the given theoretical aspects and experimental results presented later are not possible, but also not intended.

3.1. Electromagnetic forces in the system

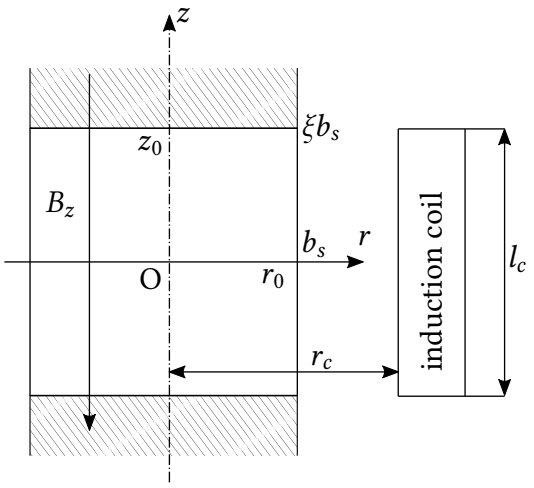

Figure 3.1.: Schematic of the variation of the induced magnetic field b_z, where B_z is steady axial magnetic field, b_s is induced magnetic field on the surface of the cylinder, ξ is a parameter describing deviation of magnetic field from the maximum, r_c and l_c are the radius and length of the coil, respectively.

A cylindrical, infinite workpiece with a radius r_0 is immersed in an infinite length induction coil, which induces an alternating magnetic field $\mathbf{b}_i$ in the workpiece. At the same time, a steady magnetic field B_z is applied axially. The sketch of a more realistic

representation of a practical problem is given in Figure 3.1 and will be further explained in detail later. Assuming the induced field $\mathbf{b}_i$ is sinusoidally alternating and only in the axial direction, $\mathbf{b}_i = b_z(r)\mathbf{e}_z e^{i\omega t}$, where $b_z(r)$ is the amplitude of the oscillating field, then the induced currents are purely azimuthal, $\mathbf{j}_i = j_\phi(r)\mathbf{e}_\phi e^{i\omega t}$. Using Faraday's and Ampere's laws, the magnetic field distribution is given as [73],

$$\frac{d^2 b_z(r)}{dr^2} + \frac{1}{r}\frac{db_z(r)}{dr} = -i\omega\sigma\mu b_z(r)\,, \tag{3.1}$$

where μ, σ and ω are magnetic permeability, specific electric conductivity and angular frequency. Taking $S^2 = \frac{\omega\sigma\mu r_0^2}{2}$, equation (3.1) can be rewritten as

$$\frac{d^2 b_z(r)}{dr^2} + \frac{1}{r}\frac{db_z(r)}{dr} + i b_z(r)\frac{2}{r_0^2}S^2 = 0\,, \tag{3.2}$$

where the dimensionless parameter S can be expressed as the ratio of the skin depth δ and the radius as $S = \frac{r_0}{\delta}$.

Two boundary conditions are applied - the magnetic field value on the surface of the cylindrical workpiece b_s and the Neumann boundary condition on the symmetry axis, i.e.

$$b_z(r)|_{r=r_0} = b_s, \left.\frac{db_z(r)}{dr}\right|_{r=0} = 0\,. \tag{3.3}$$

The solution of (3.2) with (3.3) is given by Bessel functions as:

$$b_z(r) = b_s\frac{J_0((1+i)rS/r_0)}{J_0((1+i)S)}\,, \tag{3.4}$$

where J_0 is the Bessel function of the first kind. Induced currents can be found by Ampere's law

$$j_\phi(r) = \frac{(1+i)b_s S}{r_0\mu}\frac{J_1((1+i)rS/r_0)}{\mu J_0((1+i)S)}\,. \tag{3.5}$$

The interaction between the induced current $j_\phi(r)e^{i\omega t}$ and the steady magnetic field B_z creates a radially oscillating Lorentz force F_r which in the skin depth can be found as

$$F_r(r,t) = B_z j_\phi(r) e^{i\omega t}\,, \tag{3.6}$$

and which sets the workpiece in vibration – periodic radial expansion and compression. The irrotational force is balanced by a radial pressure gradient. Integration trough the skin depth allows to find the pressure, which leads to

$$p(r,t) = -B_z e^{i\omega t}\int_0^{r_0} j_\phi dr = \frac{b_s B_z}{\mu}P(S)\, e^{i\omega t}\,, \tag{3.7}$$

where

$$P(S) = \left(1 - \frac{1}{J_0((1+i)S)}\right)\,. \tag{3.8}$$

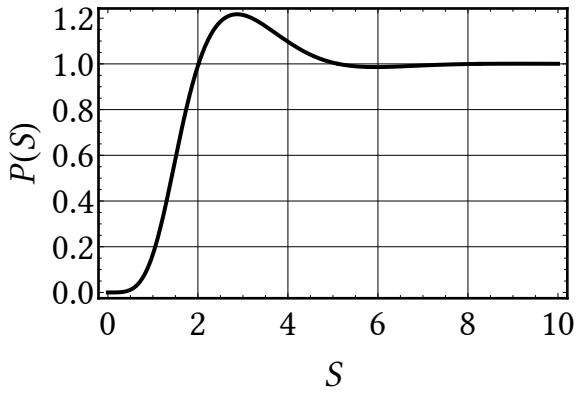

Figure 3.2.: Function's P dependence from the dimensionless parameter S.

In case of large frequencies ($S > 5$), the function $P(S) \approx 1$ as can be seen from Figure 3.2, thus the oscillating pressure amplitude P_A is given by

$$P_A = \frac{b_s B_z}{\mu} . \tag{3.9}$$

This forms the fundamental backbone of the proposed set-up [18] – an oscillating Lorentz force leading to a varying acoustic pressure can be created in the melt by superposition of a steady magnetic field B_z and the induced alternating magnetic field b_s. The electromagnetic wave also carries energy which heats and subsequently melts the workpiece. The active power can be found using the Poynting vector $\mathcal{P}$, and at high frequency, it can be approximated as

$$\mathcal{P} = \frac{0.5 b_s^2 S}{r_0 \mu^2 \sigma} . \tag{3.10}$$

Additionally, interaction between $j_\phi(r)$ and $b_z(r)$ creates a Lorentz force f_r which is responsible for stirring the melt.

However, in the previously defined system, the forces are irrotational, thus, they are only supplementing the fluid pressure. For improved analysis of the problem, the whole system must be reduced to a finite size, i.e. the induction coil is finite and consequently the induced field $b_z(r, z)$ varies along the surface of the workpiece. As there is no analytical solution for this problem, a simplified approach is sought.

For a short coil (diameter of the coil is larger than the length $2r_c > l_c$), the variation of magnetic field $b_z(r, z)$ along the central axis, i.e. depending of z, of an empty (*air*) coil can be found using the Biot-Savart law [74]:

$$b_z(r, z) = \frac{I_c \mu_c n}{2 l_c} \left(\frac{l_c (1 - z)}{\sqrt{(l_c (1 - z))^2 + r_c^2}} + \frac{l_c z}{\sqrt{(l_c z)^2 + r_c^2}} \right) , \tag{3.11}$$

where I_c is the applied coil current, n - number of turns, l_c and r_c - length and radius of the coil, respectively. If the induction coil is finite, then only a part of the infinite

workpiece melts, i.e. a molten segment with a length $2z_0$ is bound between solid semi-infinite cylinders of the same material, as shown in Figure 3.1. To further simplify the problem, it is assumed that the workpiece is non-magnetic ($\mu_r = 1$) and the specific electric conductivity difference between the solid and the liquid is negligible.

A coefficient ξ can be introduced as

$$\xi = \frac{b_z(0, z_0)}{b_z(0, 0)}, \tag{3.12}$$

where $b_z(0, z_0)$ is the magnetic field value at some endpoint, e.g. the liquid-solid boundary on the rotational axis. Then ξ describes how smaller this value is in comparison with the value at the center, i.e. the magnetic field deviation from the uniform field distribution along the cylinder. From (3.11) it then follows:

$$\xi = \frac{\sqrt{0.25 l_c^2 + r_c^2}}{\sqrt{l_c^2 + r_c^2}}. \tag{3.13}$$

As this approach is based on serious simplifications, in order to estimate the correctness of it, a numerical simulation is employed. Using FEMM 4.2 (Finite Element Method Magnetics) an axisymmetric finite case is studied.

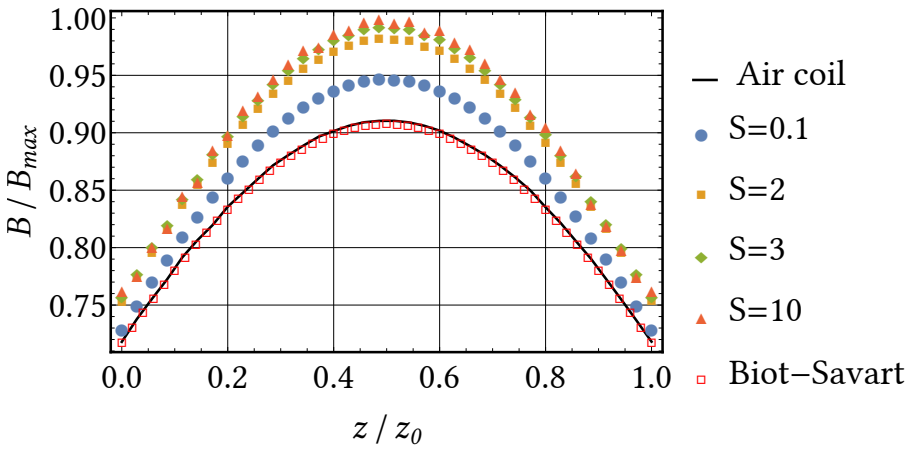

Figure 3.3.: Dimensionless magnetic field values along the workpiece boundary r_0 depending on parameter S (coloured symbols) together with an empty or *air coil* (black line) and Biot-Savart solution (red squares) on the coil axis.

Taking a coil with an aspect ratio $2r_c/l_c = 2$, magnetic field variations along the boundary of the workpiece depending on the parameter S are plotted in Figure 3.3. In the same figure also the analytical solution from (3.11) (red empty squares) together with the modelled result along the symmetry axis for an empty coil (black line) can be seen.

It can be observed that with increasing S the magnetic field maximum value on the surface increases till reaching saturation limit. The magnetic field is forced into a subsequently thinner skin-depth, and at very high frequencies the skin-depth is infinitesimal, i.e. the workpiece is effectively shielded. Most importantly, independently of any parameters,

in case with a finite coil and semi-infinite workpiece the field distribution does not change and simply follows a parabolic curve.

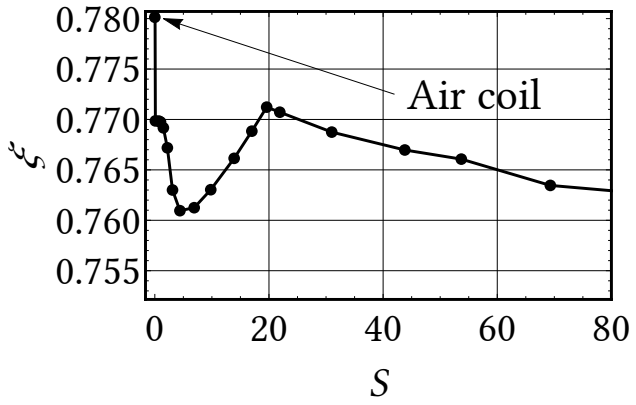

Figure 3.4.: Coefficient ξ depending on S when the molten region is equal to the length of the coil $2z_0 = l_c$. Air coil value calculated by equation (3.13). The change of ξ diminishes for further increasing S (e.g. $S = 100 : \xi = 0.758$; $S = 220 : \xi = 0.752$).

Of course, stirring by the Lorentz force f_r is only possible in the part where the metal is molten. In general, if the workpiece is somehow cooled, this molten part will be limited in size. Figure 3.4 reveals ξ from equation (3.12) as a function of the parameter S by assuming the molten region is of the same size as the coil, i.e. $2z_0 = l_c$.

With the coil aspect ratio of 2, equation (3.13) gives $\xi = 0.78$ (the *air coil* approach). As it can be seen, the variation of S changes ξ, however, the relative change is small, i.e. in the order of 4%. In other words, the magnetic field variation on the surface of a workpiece can be approximated to that of an empty coil on the symmetry axis, and the difference between the ξ value obtained by the air coil approach (3.13) and the actual values for the workpiece for any practically attainable S values is small. Essentially this gives basis to use ξ to describe the deviation from the uniform field distribution when the region of interest is of the same size or smaller than the length of the coil and if $2r_c > l_c$.

As the function to describe the variation of the magnetic field follows a parabolic equation with unity at the peak and ξ at the ends, a full equation for the magnetic field can be written as

$$b_z(r,z) = b_s \frac{J_0((1+i)\frac{r}{r_0}S)}{J_0((1+i)S)} \left(1 + (\xi - 1)\left(\frac{z}{z_0}\right)^2\right), \tag{3.14}$$

and the current distribution as

$$j_\phi(r,z) = (1+i)\frac{b_s S}{r_0 \mu} \frac{J_1((1+i)\frac{r}{r_0}S)}{J_0((1+i)S)} \left(1 + (\xi - 1)\left(\frac{z}{z_0}\right)^2\right). \tag{3.15}$$

This allows to rewrite the two electromagnetic forces, which act on the molten part of the workpiece, as

$$F_r(r,z,t) = j_\phi(r,z)B_z e^{i\omega t}\,, \tag{3.16}$$

and

$$f_r(r,z,t) = j_\phi(r,z,t)b_z(r,z,t)\,. \tag{3.17}$$

The force, which entails both the mean part $\langle f\rangle$ and the oscillating part $\tilde{f}$, can be expanded as

$$\begin{aligned} f_r(r,z,t) &= \mathrm{Re}[j_\phi(r,z)e^{i\omega t}]\mathrm{Re}[b_z(r,z)e^{i\omega t}] = \\ &= \frac{1}{2}\mathrm{Re}[j_\phi(r,z)b_z^*(r,z)] + \frac{1}{2}\mathrm{Re}[j_\phi(r,z)b_z(r,z)e^{2i\omega t}]\,, \end{aligned} \tag{3.18}$$

where * denotes the complex conjugate.

Only the time independent part plays any role regarding the workpiece and/or melt zone, while the component, which oscillates with double the frequency, induces a comparably negligible motion because of the finite inertia of the fluid. However, the oscillating component can set the solid metallic parts in vibration and create noise.

Averaging (3.18) over time gives:

$$f_r(r,z) = \langle f\rangle = \frac{1}{2}\mathrm{Re}[j_\phi(r,z)b_z^*(r,z)]\,. \tag{3.19}$$

Using (3.14) and(3.15), the following expressions result from (3.16) and (3.19):

$$\begin{aligned} F_r(r,z,t) &= \frac{b_s B_z S}{\mu r_0}\left(1+(\xi-1)\left(\frac{z}{z_0}\right)^2\right)\mathrm{Re}\left[\frac{(1+i)J_1((1+i)\frac{r}{r_0}S)}{J_0((1+i)S)}\right]e^{i\omega t} = \\ &= \frac{b_s B_z S}{\mu r_0}\left(1+(\xi-1)\left(\frac{z}{z_0}\right)^2\right)F(r;S)e^{i\omega t}\,; \end{aligned} \tag{3.20}$$

$$\begin{aligned} f_r(r,z) &= \frac{b_s^2 S}{\mu r_0}\left(1+(\xi-1)\left(\frac{z}{z_0}\right)^2\right)^2\mathrm{Re}\left[\frac{J_1((1+i)\frac{r}{r_0}S)J_0^*((1+i)\frac{r}{r_0}S)}{|J_0((1+i)S)|^2}\right] = \\ &= \frac{b_s^2 S}{\mu r_0}\left(1+(\xi-1)\left(\frac{z}{z_0}\right)^2\right)^2 f(r;S)\,. \end{aligned} \tag{3.21}$$

At the point $r = r_0$, the Bessel function parts ($F(r;S)$ and $f(r;S)$) of both (3.20) and (3.21), which at this point have the same value, are plotted in Figure 3.5. For $S \gg 1$, the functions $f(r;S)$ and $F(r;S)$ can be approximated to 1, while for $S < 1$ the dependence scales as $0.25S^3$, giving the amplitude of the electromagnetic forces.

The radial dependence of $F(r;S)$ can be estimated from Figure 3.6. For large S, the radial force variation is well described by an exponential decrease typical for the skin effect, i.e.

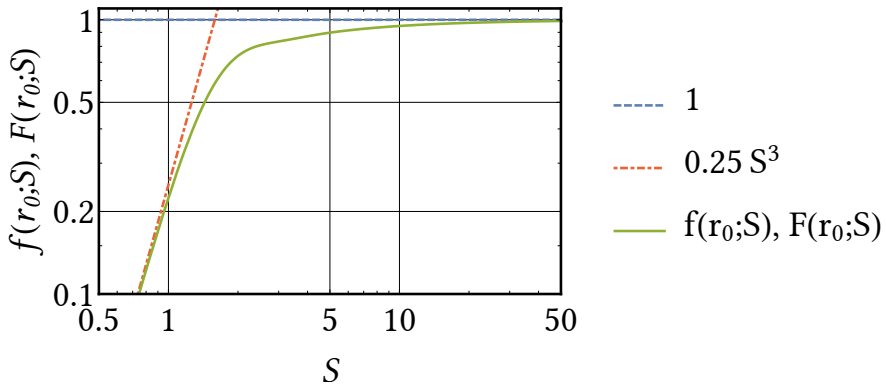

Figure 3.5.: Functions $f(r;S)$ and $F(r;S)$ approximation at the point $r = r_0$ as a function of the dimensionless parameter S.

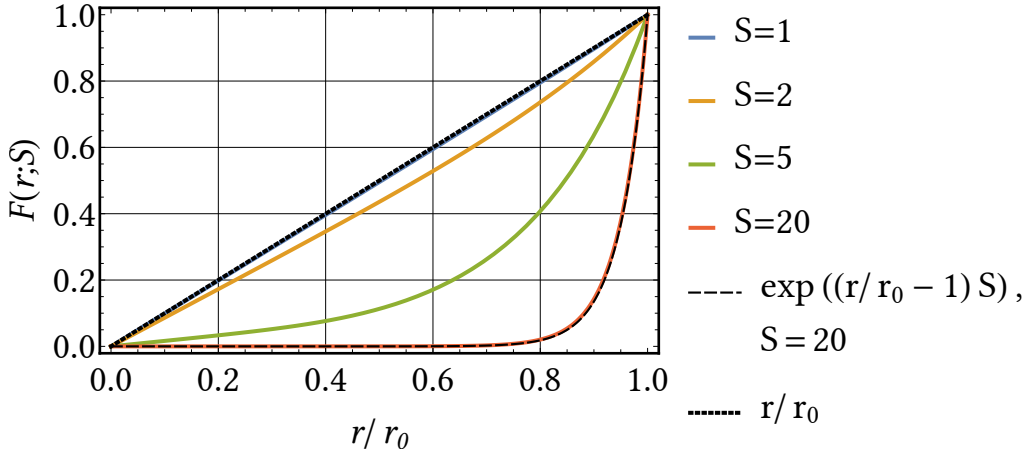

Figure 3.6.: Calculated functions $F(r;S)$ dependence on the dimensionless radius for different values of the parameter S.

$e^{-r/\delta} = e^{(-1+r/r_0)S}$, while for small S the dependence is linear with r/r_0. Thus, for small S equation (3.20) can be approximated to:

$$F_r(r,z,t) \approx -\frac{S^4 b_s B_z r}{4\mu r_0^2}\left(1+(\xi-1)\left(\frac{z}{z_0}\right)^2\right)e^{i\omega t}, \tag{3.22}$$

and for large S it reads as,

$$F_r(r,z,t) \approx -\frac{b_s B_z S e^{(-1+r/r_0)S}}{\mu r_0}\left(1+(\xi-1)\left(\frac{z}{z_0}\right)^2\right)e^{i\omega t}. \tag{3.23}$$

In a similar manner $f(r;S)$ can be estimated from Figure 3.7. For large S, the radial force variation follows an exponential decrease $e^{2(-1+r/r_0)S}$ while for small S it scales as $(r/r_0)^3$. Thus, for small S equation (3.21) can be approximated to:

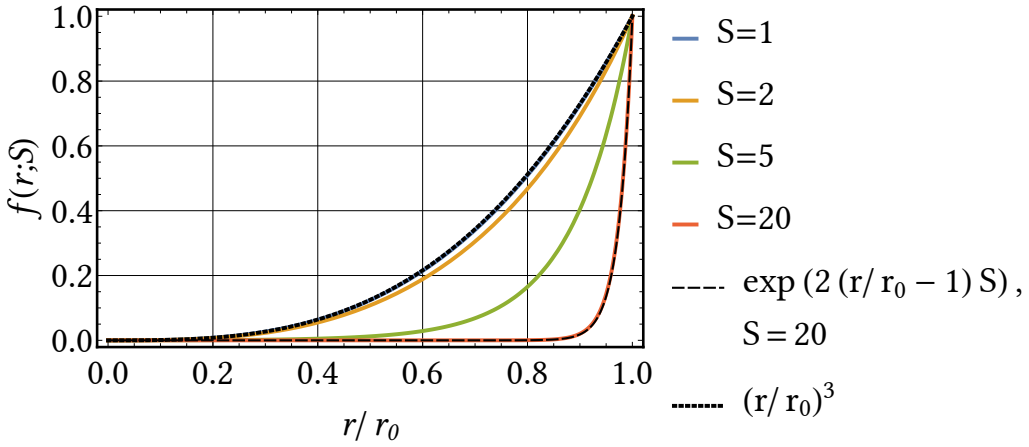

Figure 3.7.: Calculated functions $f(r;S)$ dependence on the dimensionless radius for different values of the parameter S.

$$f_r(r,z) \approx -\frac{b_s^2 r^3 S^4}{8\mu r_0^4}\left(1+(\xi-1)\left(\frac{z}{z_0}\right)^2\right)^2, \tag{3.24}$$

and for large as,

$$f_r(r,z) \approx -\frac{b_s^2 S e^{2(-1+r/r_0)S}}{2\mu r_0}\left(1+(\xi-1)\left(\frac{z}{z_0}\right)^2\right)^2. \tag{3.25}$$

3.2. Magnetohydrodynamic considerations of the system

3.2.1. Flow driven by the induction coil

The simplified force formulas obtained in the previous section can be used to determine the flow inside the melt. For an incompressible fluid the Navier-Stokes equation holds, which is given by:

$$\frac{\partial \mathbf{u}}{\partial t} + (\mathbf{u} \cdot \nabla)\,\mathbf{u} = -\frac{1}{\rho}\nabla p + \nu \nabla^2 \mathbf{u} + \mathbf{F}/\rho\,, \tag{3.26}$$

where ν is kinematic viscosity, p is pressure, ρ is density, $\mathbf{F}$ is a body force, t denotes time and $\mathbf{u}$ is the velocity field, and together with the continuity equation,

$$\nabla \cdot \mathbf{u} = 0\,, \tag{3.27}$$

fully describes the flow field for any given boundary and initial conditions. The flow driving force $\mathbf{F}$ is a sum of the Lorentz force $\mathbf{f}_{r,z} = f_r(r,z)\mathbf{e}_r$ from equation (3.19) and the braking force $\mathbf{F}_B$ which arises from Ohm's law for a moving electrical conductor in a static magnetic field, and is described by:

$$\mathbf{F}_B = -\sigma u_r B_z^2 \mathbf{e}_r\,. \tag{3.28}$$

With no electrostatic field imposed externally, the electric potential is zero in this case due to the symmetry of the problem and the assumed axisymmetry of the meridional flow. Keeping the ratio $z_0/r_0 = 1$, and using the following substitutions:

$$t^* = \frac{t}{r_0^2/\nu}\,, \quad r^* = \frac{r}{r_0}\,, \quad z^* = \frac{z}{r_0}\,, \quad \mathbf{u}^* = \frac{\mathbf{u}}{\nu/r_0}\,, \quad p^* = \frac{p}{\rho(\nu/r_0)^2}\,, \tag{3.29}$$

equation (3.26) can be rewritten as,

$$\frac{\partial \mathbf{u}}{\partial t} + (\mathbf{u} \cdot \nabla)\,\mathbf{u} = -\nabla p + \nabla^2 \mathbf{u} + \frac{f_r(r,z) r_0^3}{\rho \nu^2}\mathbf{e}_r - \frac{\sigma B_z^2 r_0^2}{\rho \nu} u_r \mathbf{e}_r\,, \tag{3.30}$$

with asterisks removed for convenience and continuity equation remaining the same. Two dimensionless numbers appear, namely

$$\mathrm{Ha}^2 = \frac{\sigma B_z^2 r_0^2}{\rho \nu}\,; \quad \mathrm{F} = \frac{f_r(r,z) r_0^3}{\rho \nu^2}\,, \tag{3.31}$$

where Ha is the Hartmann number and F is the dimensionless driving force.

Equation (3.30) together with the continuity equation is solved using the finite element method (FEM) in Mathematica 11.3. The solution is obtained in a rectangular domain in the meridional plane. Symmetry condition is applied on $r = 0$, thus, momentum there is directed along the axis. Furthermore, no-slip condition for the velocity is applied at top and bottom $z = \pm 1$, and at the side wall $r = 1$.

The flow structure without and with applied magnetic field can be seen in Figure 3.8 (a) and (b), respectively. The basic flow without applied field consists of two recirculating vortices, with the maximum radial velocity in the midplane which is defined by the Lorentz

force distribution in the melt. Applying steady axial magnetic field lowers the velocity and influences the flow pattern. The horizontal walls $z = \pm 1$, where B_z has the normal component, are called Hartmann walls while the wall tangential to B_z at $r = 1$ is called side wall. Assuming that the side wall is electrically isolating, e.g. a ceramic crucible, the flow becomes restricted to this outer layer at the surface. In such instance a radial segregation of the particles could be expected.

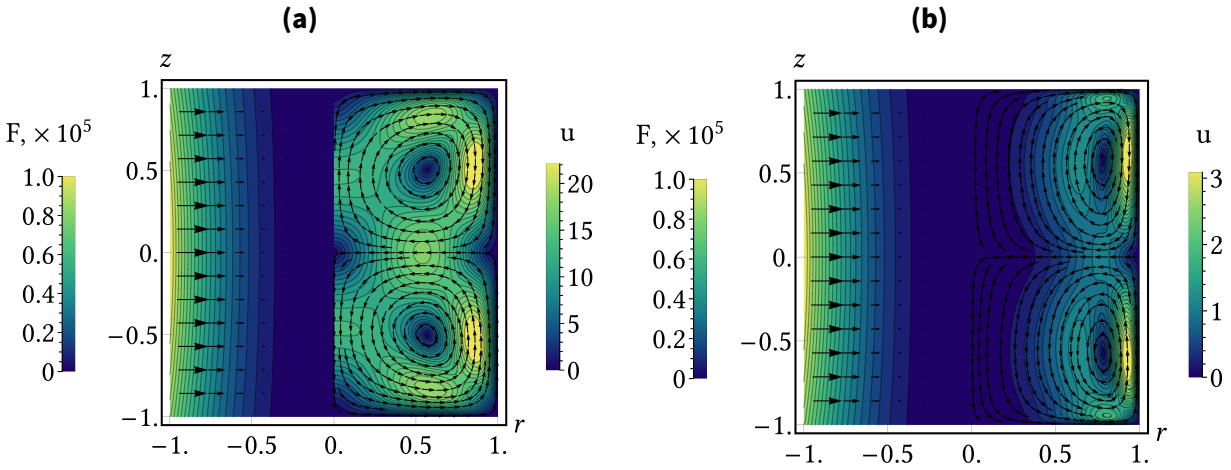

Figure 3.8.: Isolines of the dimensionless velocity amplitude at dimensionless driving force $F = 10^5$ without applied static magnetic field (a) and with applied axial magnetic field (Ha = 50) (b). Left side shows the force distribution in the volume.

The maximum radial and axial velocity dependence from the applied F at different magnetic fields is plotted in Figure 3.9 (a) and (b), respectively. A linear scaling of the maximal velocity values can be seen. The scaling laws for the radial ($0.28\,\mathrm{F\,Ha^{-2}}$) and axial components ($0.054\,\mathrm{F\,Ha^{-3/2}}$) are in a close agreement with values published in [75]. Scaling r by a factor of $\mathrm{Ha}^{1/2}$ (characteristic thickness of side layers) reveals the formation of the side layers for different Ha numbers in Figure 3.10 for radial (a) and axial (b) velocity profiles.

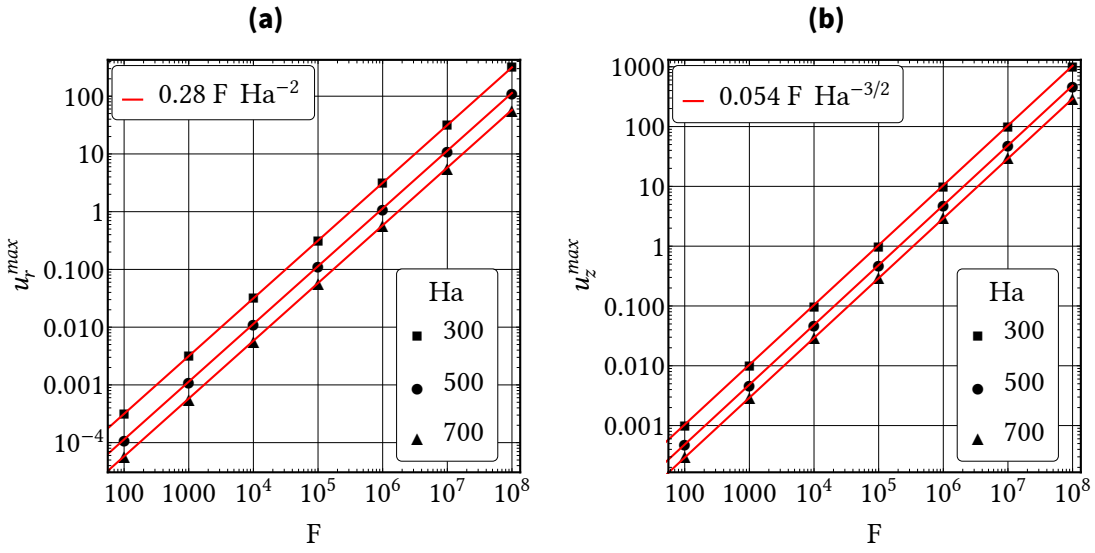

Figure 3.9.: Calculated dimensionless maximum radial u_r^{max} (a) and axial u_z^{max} (b) velocities as a function of the force magnitude for different Hartmann numbers.

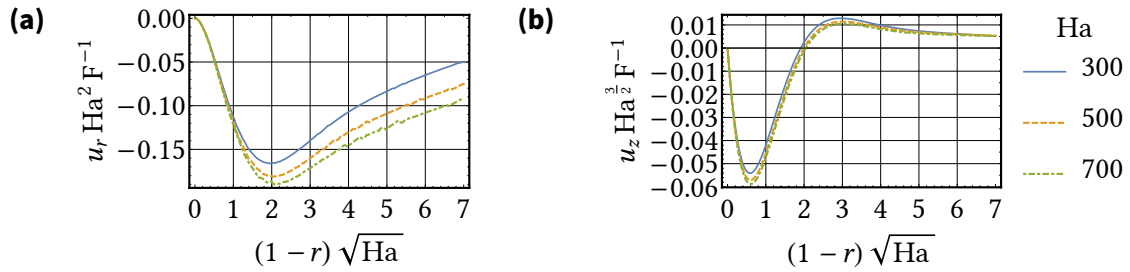

Figure 3.10.: Scaled radial profiles of the radial velocity at $(r, 0)$ (a) and axial velocity at $(r, 0.5)$ (b) depending on the Hartmann number for $\mathrm{F} = 10^6$.

3.2.2. Steady streaming

In the basic flow calculations the influence of the oscillating force $F_r(r, z, t)$ from equations (3.22) or (3.23) is neglected. Such force will create an oscillating flow $\mathbf{u}'$. While the mean $\overline{\mathbf{u}'}$ over the oscillating period is zero, the mean value of quadratic combinations of the velocities may not be. Similar to turbulence modelling, these terms are called the Reynolds stress $\tau_{i,j} = \rho\overline{u_i' u_j'}$, where $\rho\overline{u_i'}^2$ is the Reynolds normal stress and $\rho\overline{u_i' u_j'}$ is the Reynolds shear stress. Reynolds stress creates a mean force that acts on the fluid, which leads to:

$$F_{stream,j} = -\frac{\partial(\rho\overline{u_i' u_j'})}{\partial x_i}\,. \tag{3.32}$$

A flow created by such force is called steady streaming. The streaming force can be neglected as long as it remains much lower than the steady flow driving forces. However,

as in the present case the oscillating force scales with B_z, and the magnetic field can be varied in a large range, an estimate of such streaming flow is necessary. The Navier-Stokes equation with the oscillating term takes the following form:

$$\frac{\partial \mathbf{u}'}{\partial t} + (\mathbf{u}' \cdot \nabla)\,\mathbf{u}' = -\frac{1}{\rho}\nabla p + \nu \nabla^2 \mathbf{u}' + \frac{\mathbf{F}_{osc}}{\rho}\,, \tag{3.33}$$

where $\mathbf{F}_{osc} = F_r(r, z, t)\mathbf{e}_r$ from either equation (3.22) or (3.23).

Using substitutions from equations (3.29) and

$$\omega^* = \frac{\omega}{\nu / r_0^2}\,, \quad \mathrm{F}^*_{osc} = \frac{r_0^3}{\rho \nu^2} F_r(r, z, t)\,, \tag{3.34}$$

the Navier-Stokes equation can be rewritten in the dimensionless form (3.35) with asterisks removed for convenience and where F_{osc} is the dimensionless oscillating force parameter:

$$\frac{\partial \mathbf{u}'}{\partial t} + (\mathbf{u}' \cdot \nabla)\,\mathbf{u}' = -\nabla p + \nabla^2 \mathbf{u}' + \mathrm{F}_{osc}\,\mathbf{e}_r\,. \tag{3.35}$$

It can be assumed that the AC frequency is much higher than the *hydrodynamic* one, i.e. $\omega \gg u/r_0$, thus, the convective term can be neglected in the Navier-Stokes equation, yielding

$$\frac{\partial \mathbf{u}'}{\partial t} = -\nabla p + \nabla^2 \mathbf{u}' + \mathrm{F}_{osc}\,\mathbf{e}_r\,. \tag{3.36}$$

Outside a thin boundary layer, which has the characteristic thickness $\delta \sim \sqrt{\nu/\omega}$, also the diffusion term can be removed, and taking curl discards the pressure term, leaving

$$\nabla \times \frac{\partial \mathbf{u}'}{\partial t} = \nabla \times \mathrm{F}_{osc}\,\mathbf{e}_r\,. \tag{3.37}$$

As $\mathrm{F}_{osc} \sim \mathrm{e}^{i\omega t}$, then a direct relation $\mathbf{u}' = \mathbf{u}'_0 \mathrm{e}^{i\omega t}$ is assumed and the equation (3.37) can be rewritten as

$$i\omega \nabla \times \mathbf{u}'_0 = \nabla \times \mathrm{F}_{osc}\,\mathbf{e}_r\,, \tag{3.38}$$

where F_{osc} is no longer time dependent. Then,

$$\mathbf{u}'_0 = \frac{\mathrm{F}_{osc}\,\mathbf{e}_r}{i\omega} + \nabla\psi\,, \tag{3.39}$$

where ψ is an unknown potential. Using mass conservation (3.27) and taking divergence gives Poisson's equation (3.40) for the potential

$$\nabla^2 \psi = -\nabla \cdot \frac{\mathrm{F}_{osc}\,\mathbf{e}_r}{i\omega}\,. \tag{3.40}$$

Boundary conditions for ψ are found by setting $u'_n = 0$ on all boundaries, i.e.

$$\nabla\psi \cdot \mathbf{n} = -\frac{\mathrm{F}_{osc}\mathbf{e}_r \cdot \mathbf{n}}{i\omega}\,, \tag{3.41}$$

where **n** is the outward directed normal.

To validate the made assumptions, the simplified solution (3.39) is compared with solving the fluid flow equation (3.35) numerically using a transient solver. Figure 3.11 (a) presents a comparison of both methods by showing the maximum radial velocity u_r' depending of the dimensionless frequency ω (from equation (3.34)) for different oscillating force parameter F_{osc} values. The symbols mark the numerical solution while solid lines represent the corresponding values obtained with the simplified solution. The dependence on the parameters is straightforward: the flow velocity is linearly dependent on F_{osc} (velocity increases with an increased oscillating force) while inversely proportional to ω as inertia damps the flow driving action with increasing frequency. It can be observed that the results of both methods do not fit ideally. The disparity between the two methods is better revealed in Figure 3.11 (b), where relative difference ($\delta u_r' = (u_{r,sim}' - u_{r,num}')/u_{r,num}'$, where *sim* denotes simplified solution while *num* denotes numerical solution) of the maximum oscillating radial velocity component $u_r'^{max}$ is plotted. The velocity graph reveals a relative error of around 15%, while the variation due to oscillating force at constant frequency is in the order of 1%.

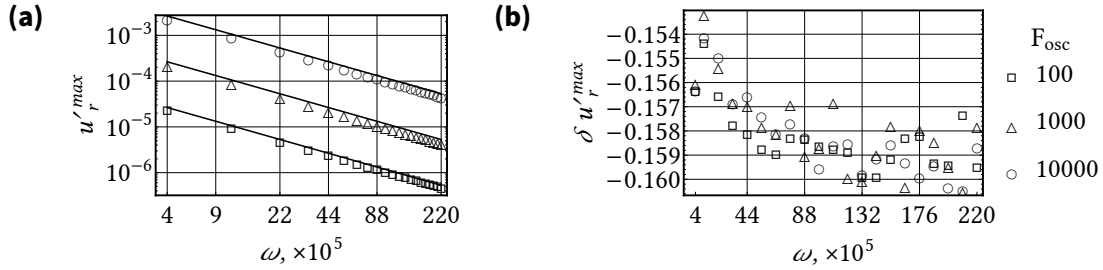

Figure 3.11.: Comparison of the maximum radial oscillating velocity dependence of the dimensionless frequency ω at different oscillating force parameter F_{osc} values solved by two methods (a). The symbols mark numerical solution while solid lines mark the corresponding values obtained with the simplified approach (3.39). The relative difference of results by both methods is revealed in (b).

In Figure 3.12 the oscillating velocity $\mathbf{u}_0'$ components obtained with the numerical approach for $F_{osc} = 1 \cdot 10^4$ and $\omega = 10 \cdot 10^5$ are compared to the simplified solution along $(0.85, z)$ in (a) and along $(r, 0.5)$ in (c). Subsequently, the streaming force $\mathbf{F}_{stream}$ from equation (3.32) can be obtained. The radial component of this force is compared in the same manner as the oscillating velocity in (b) and (d). The error of the simplified approach becomes visible – as no-slip boundary conditions are not applied, velocity components normal to the respective boundaries do not reach zero. This also affects the profile of the streaming force, showing an overestimation at the edges. The streaming force depends on the spatial variation of the oscillating flow and is stronger where the difference is larger. While the maximum relative difference can reach 20%, the obtained profiles are similar outside the thin boundary layers. The error there possibly arises due to the elimination of the convective term that affects the attainable velocity in the bulk.

It is important to note that the numerical solution depends on the time step as well as mesh refinement, even more at higher frequencies where the boundary layer becomes

increasingly smaller. Mathematica is not a computational fluid dynamics software *per se* and solving time dependent fluid dynamics problems is, most likely, at the edge of its capabilities. Therefore, the obtained relative differences should not be taken at face value, and emphasis is put on the similarity of the profiles. The comparison between both approaches has shown that the simplified approach can be used to estimate the Reynolds stresses and the streaming force at least within the bulk of the sample. As later analysis will show, steady streaming is more relevant at low ω and/or very high Ha numbers, while in more realistic conditions the phenomenon is of lower importance.

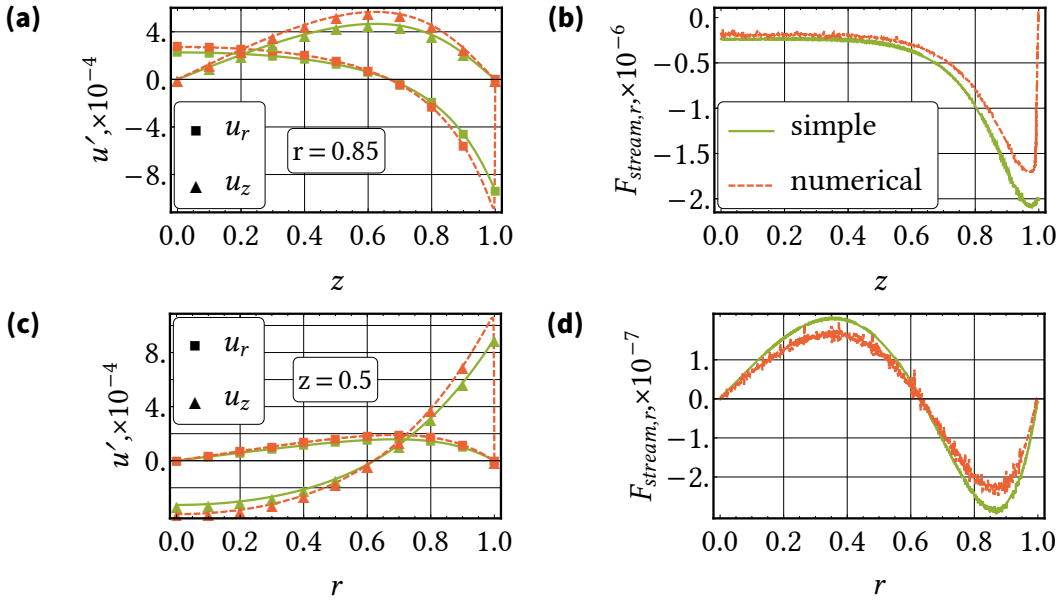

Figure 3.12.: Numerical solution (red dashed line) for the dimensionless oscillating velocity components u_r' (squares) and u_z' (triangles) compared with the simplified approach (green line) along $(0.85, z)$ in (a) and along $(r, 0.5)$ in (c). The radial component of the dimensionless streaming force $\mathbf{F}_{stream}$ is compared in the same manner in (b) and (d). Oscillating force parameter and dimensionless frequency are $\mathrm{F}_{osc} = 1 \cdot 10^4$ and $\omega = 10 \cdot 10^5$.

The steady streaming force obtained by the simplified formulae can be directly incorporated into the Navier-Stokes solver by adding the force term and the effect on the basic flow can be investigated. Figure 3.13 shows the flow structure without (a) and with (b) the steady streaming term. The basic flow is driven by $\mathrm{F} = 1.7 \cdot 10^6$ with $\mathrm{Ha} = 200$. Adding the oscillating force $\mathrm{F}_{osc} = 2.6 \cdot 10^8$ with a dimensionless frequency of $\omega = 5.4 \cdot 10^4$ homogenizes the bulk flow by reducing the effect of the side layers and gives rise to a counter-rotating vortex at the outer part of the sample. Note, the solution shown in Figure 3.13 (b) is already time-dependent whereas the flow in (a) is in a steady state. It indicates that the steady streaming not only changes the flow structure, but also causes instability of the basically laminar flow.

However, the effect of the streaming term is highly dependent on ω and B_z. Figure 3.14 reveals the comparison between the maximum radial and axial velocities with and without the steady streaming term depending on the Ha number for $\mathrm{F} = 1.7 \cdot 10^6$. Results for different ω values are shown. A clear dependence on the applied frequency can be

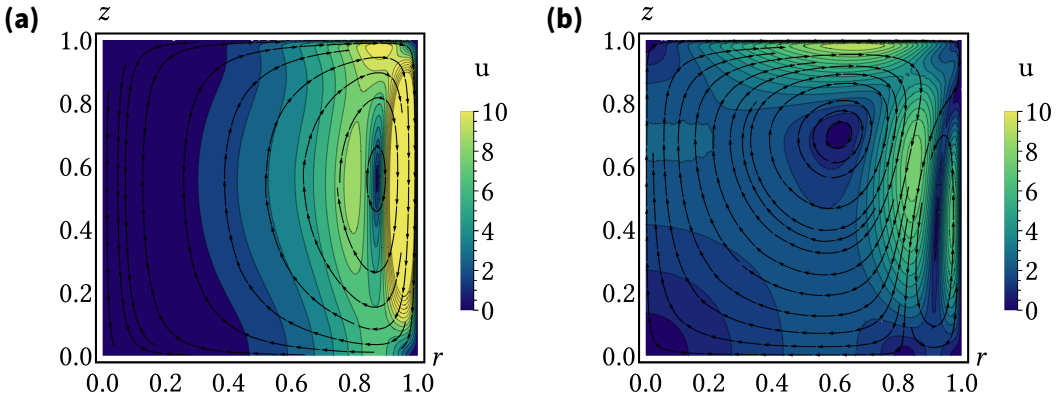

Figure 3.13.: Isolines of the velocity amplitude comparing flow without (a) and with steady streaming (b) at Ha = 200, F = $1.7 \cdot 10^6$. Steady streaming created by oscillating force $F_{osc} = 2.6 \cdot 10^8$ with dimensionless frequency $\omega = 5 \cdot 10^4$.

observed as the stress induced flow plays a diminishing role for increasing ω. The scaling with B_z is obvious – the steady streaming force scales with u'^2, and, since $u' \sim F_{osc} \sim B_z$, then steady streaming scales with B_z^2. Similarly, the damping from equation (3.28) has a braking action scaling with B_z^2. This means there is always a value of B_z at which the flow due to the steady streaming has a maximum. The scaling with frequency ω can be resolved from equations (3.22) and (3.23). For small ω the oscillating force F_{osc} scales with ω^2, whereas for $S \gg 1$ it becomes a surface force increasing with $\sqrt{\omega}$. Furthermore, the resulting velocity adds an additional scaling with ω^{-1} (3.39) due to the fact that the flow inertia damps the flow driving action for increased driving frequency. Comparing radial and axial velocities, it can be observed that the steady streaming term accelerates the flow in the axial direction, which also follows from the direction of the damping force. Furthermore, an interesting tendency can be observed at lower ω – with an increasing Ha the braking force does not efficiently damp the flow as the larger F_{osc} and, thus, the steady streaming plays a more prominent role in impacting the motion.

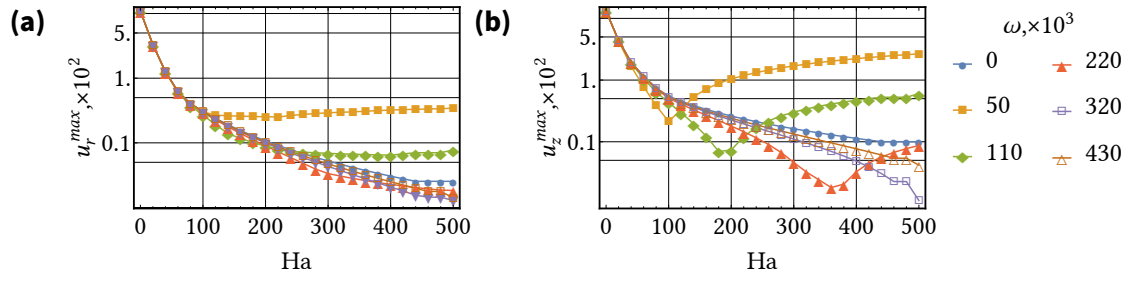

Figure 3.14.: Comparison of maximal radial (a) and axial (b) velocity values against Ha without ($\omega = 0$) and with steady streaming at different ω values. Basic flow driving force parameter F = $1.7 \cdot 10^6$.

Figure 3.15 reveals a comparison of radial and axial velocity profiles with and without steady streaming depending on the dimensionless frequency ω along $(r, 0)$ in (a) and $(r, 0.5)$ in (b) with Ha = 200 and $F = 1.7 \cdot 10^6$. It can be seen that at low ω values, u_r also changes qualitatively with a different sign near the side layer due to the larger influence of the steady streaming, which creates a second vortex. Similarly, u_z is dominated by steady streaming with lower ω.

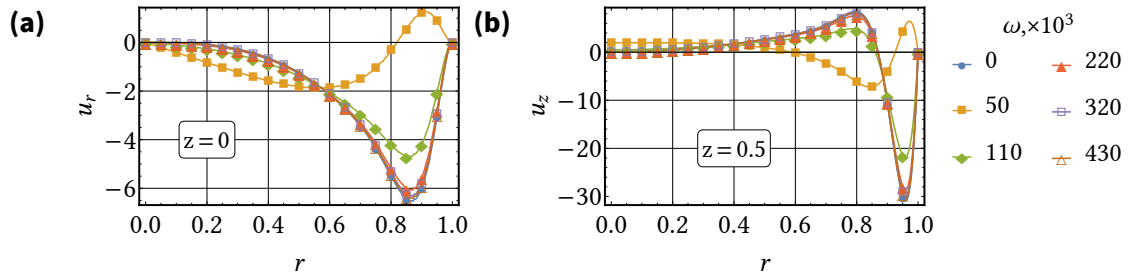

Figure 3.15.: Comparison of radial (a) and axial (b) velocity profiles without ($\omega = 0$) and with steady streaming at different ω values with Ha = 200 and $F = 1.7 \cdot 10^6$. Profiles taken along $(r, 0)$ and $(r, 0.5)$.

To evaluate the importance of steady streaming an example based on experimental conditions described in chapter 5.1 is presented. Taking $r_0 = 0.01\,\mathrm{m}$, $\xi = 0.6$, $\omega = 6.3 \times 10^4\,\mathrm{s}^{-1}$, $b_s = 0.1\,\mathrm{T}$ and $B_z = 1\,\mathrm{T}$ for a molten austenitic steel 1.4401 sample ($\eta = 8\,\mathrm{mPa\,s}$, $\rho = 6.881\,\mathrm{g\,cm}^{-3}$ [76], $\sigma = 1.35 \times 10^6\,\mathrm{S\,m}^{-1}$ [77]) $S = 2$, Ha = 130 and $F = 1.7 \times 10^8$ from equation (3.31), $F_{osc} = 3.4 \times 10^9$ and the dimensionless frequency $\omega = 5.4 \times 10^6$ from equation (3.34). The calculations reveal that with such high frequency the maximum velocity with and without streaming is the same and can reach $0.49\,\mathrm{m\,s}^{-1}$. Changing to $B_z = 18\,\mathrm{T}$ (Ha = 2300) gives a maximum velocity of $0.0077\,\mathrm{m\,s}^{-1}$ without steady streaming in contrast to a maximum velocity of $0.0071\,\mathrm{m\,s}^{-1}$ with the steady streaming – a decrease by 7.7 %. While the influence in absolute values is rather small, the ability of the steady streaming to amplify the flow braking at high Ha and ω must be taken into account. However, also the change of the flow structure and the possible instability onset due to the steady streaming as seen in Figure 3.13 (b), as well as the instabilities associated with high Ha numbers [75], may cause a stronger impact on the homogenization and dispersion of the particles in the melt. More detailed studies about this effect have to be undertaken.

3.2.3. Acoustic pressure distribution in the melt

Using the previously described simplifications the oscillating pressure field can also be found. Removing the diffusion term in equation (3.36) and taking divergence gives an equation for the pressure,

$$\nabla^2 p = \nabla \cdot F_{osc}\,\mathbf{e}_r\,. \tag{3.42}$$

This equation is solved numerically with $p = 0$ on the surface $r = 1$ and $dp/dn = 0$ on the symmetry planes and at the top $z = 1$. Figure 3.16 shows the solved oscillating pressure p amplitude normalized with $P_A = b_s B_z/\mu$ from equation (3.9) depending on moderate and large S values ($S = 10$ in (a) and $S = 100$ in (b)). Note, the oscillating pressure p is directly caused by the oscillating force F_{osc}, and the distribution of the oscillating pressure amplitude does not correlate with the mean flow in the sample as described in section 3.2.1.

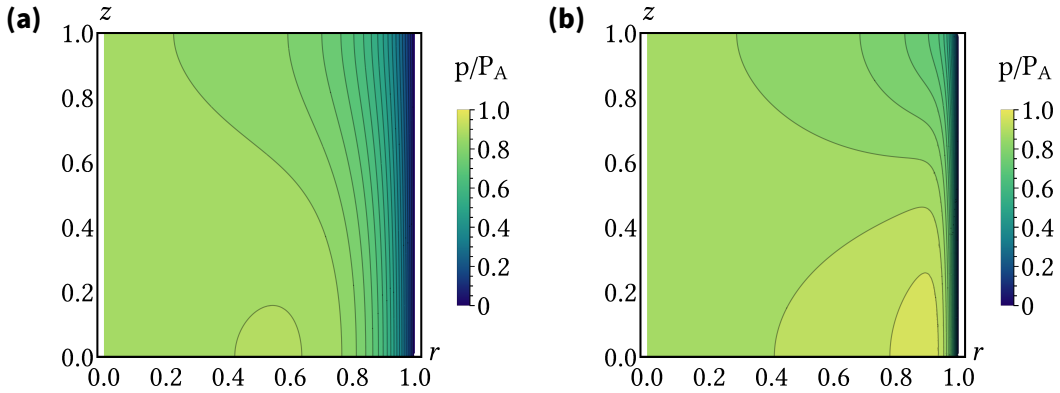

Figure 3.16.: Contour plots of dimensionless pressure p amplitude normalized against P_A from equation (3.9) at (a) $S = 10$ and (b) $S = 100$.

It can be seen that for increased S the distribution of the pressure oscillations (except at the outer rim at $r \leq 1$) becomes increasingly homogeneous over the sample volume, which is an important benefit of the contactless magnetic initiation of cavitation. In comparison to the pressure distribution obtained with ultrasonic mixers, where the pressure oscillations are relevant only in the vicinity of the ultrasonic tip ([78], [79]), the contactless approach can provide significant values throughout the volume.

3.3. Description of the bubble dynamics in the system

By the most basic definition of cavitation the liquid must be torn apart, and by doing so cavities or voids are created which then fill with vapour and/or gas inside the liquid. In an ideal case the tension required is equal to the tensile strength of the liquid; in reality impurities act as weakness (and cavitation nuclei) which lowers the strength. In first approximation, to put the liquid into tension, for some part of the oscillation cycle the oscillating pressure amplitude P_A must become larger than the static (ambient) one to create a negative pressure inside the liquid [41], [80].

While it is not possible to predict if cavitation will be obtainable as it heavily depends on the purity of the melt which is typically unknown, the dynamics of a cavitating bubble forced by a cyclic pressure field in an incompressible liquid (speed of sound $\rightarrow \infty$) can be examined using the Rayleigh-Plesset equation, which reads as

$$R\ddot{R} + \frac{3\dot{R}^2}{2} = \frac{1}{\rho}\left(\left(p_0 + \frac{2\gamma}{R_0} - p_v\right)\left(\frac{R_0}{R}\right)^{3\kappa} + p_v - \frac{2\gamma}{R} - \frac{4\eta\dot{R}}{R} - p_0 - P_A\sin(\omega t)\right), \tag{3.43}$$

where R is the time dependent radius of the bubble, R_0 the initial bubble radius, ρ the density of the liquid, p_0 the ambient pressure in the liquid, γ - surface tension, p_v - vapour pressure, η - dynamic viscosity of the liquid, κ - polytropic constant, P_A - pressure amplitude and ω - angular frequency, and dots represent the time derivatives.

Initially, the bubble with radius R_0 is at rest. It is also assumed that the bubble is already present in the liquid, it is filled with an ideal gas and obeys a polytropic law. Furthermore, the vapour pressure and the gas content in the bubble is considered constant during the oscillation. Also the temperature inside and outside the bubble is uniform and constant. In reality, there is a multitude of bubbles inside the liquid and there is a strong interaction between them, but for simplicity multi-bubble effects are ignored. While other models exist, at low Mach numbers they give essentially the same information, and can predict the oscillations and implosion of a single bubble reasonably well.

By linearising the equation (3.43) it is possible to find the resonance frequency (3.44) for a bubble with a radius R_0, or, alternately, to find the resonant radius if the frequency is known,

$$\omega_0 = \frac{1}{\sqrt{\rho}R_0}\sqrt{3\kappa\left(p_0 + \frac{2\gamma}{R_0} - p_v\right) - \frac{2\gamma}{R_0} + p_v - \frac{4\eta^2}{\rho R_0^2}}\,. \tag{3.44}$$

As mentioned earlier, bubbles can also oscillate in an unstable manner, which defines the transient cavitation. The short-lived high energy collapses are more relevant than the stable oscillations as these provide the means for particle wetting and dispersion. Still, even stable oscillating bubbles can influence the metallic microstructure as shown in [81].

However, the question about transient cavitation inception is not easy to answer. The threshold is defined by the driving frequency as well as the negative pressure which puts the liquid into tension. From (3.44) it is clear that a smaller bubble will have a higher resonance frequency. As explained by Leighton [41], it means that the bubble has more time to expand before the liquid is compressed by the sound field. By then there is larger

Table 3.1.: The physical properties of different metals with calculated resonance sizes for $f = 14\,\mathrm{kHz}$ and Blake's radius for $P_A = 80\,\mathrm{kPa}$. Physical properties given at the melting tempearture [84].

Liquid	Sn	Al	Fe	Ni	H_2O
Density, ρ g cm^{-3}	7.000	2.385	7.015	7.905	1
Dynamic viscosity, η mPa s	1.85	1.30	5.50	4.90	1
Surface tension, γ mN m^{-1}	544	914	1872	1778	60
Resonance size, R_0 10^{-5} m	4.4	7.3	6.6	6.2	4.4
Blake's radius, R_B 10^{-5} m	0.5	0.8	1.8	1.7	0.065

Table 3.2.: Parameters for calculating bubble sizes in Table 3.1.

pressure amplitude, P_A	80 kPa
frequency, f	14 kHz
vapour pressure, p_v	0 kPa
ambient pressure, p_0	0.5 kPa
polytropic index, κ	5/3 (for Ar)

amount of elastic energy stored which is released during the collapse. Larger bubbles, however, have a slower response time, i.e. there is not enough time for a significant growth during a single tension phase. On the other extreme, growth for very small bubbles is hindered by the surface tension. Thus, there is a range of bubbles which will grow rapidly and end with a violent collapse. The minimum value for the acoustic pressure (also called Blake's pressure) that is needed for an explosive growth of a bubble with the initial radius R_B (Blake's radius), i.e. the lower threshold for a transient cavitation, is given by

$$P_A = p_0 + \frac{8\gamma}{9}\sqrt{\frac{3\gamma}{2R_B^3(p_0 + (2\gamma/R_B))}}\,. \tag{3.45}$$

In the case considered in this work, the cavitation limits are imposed by the experimental configuration, namely the used frequency f and the applied B_z, which in turn limits the pressure amplitude P_A, as shown by equation (3.9). The physical properties of selected liquid metals are given in Table 3.1. Solving equation (3.44) with the parameters from Table 3.2, the resonance radius of a bubble for the different metals can be found (water values for reference). Additionally, using the maximum obtainable pressure amplitude, Blake's radius can be determined by equation (3.45). Such collapsing bubbles in the range $[R_B{:}R_0]$ can create jets with a diameter of 1/10 of the maximum bubble radius. These jets can attain a velocity of 1000 m s^{-1} with a pressure of up to 4 GPa [82], which provides enough force to separate even nanoparticles [83].

Preconditions for bubbles in a range [R_B:R_0] to exist in a liquid metal are not given or known beforehand, and cavitation can be only assumed to happen. Real melts always contain impurities as well as dissolved gas (either as combined substances, such as oxides, nitrides etc., or uncombined, such as oxygen, nitrogen, hydrogen etc.) [85]. The poorly wetted inclusions will act as weak spots of the melt and, subsequently, cavitation nuclei. Furthermore, the amount of the inclusions is increased during composite production since weakly wetted particulates are added as a reinforcement, thus, increasing the readily available amount of the cavitation nuclei. As a simple estimation, assuming mass of a melt $m_l = 0.1\,\mathrm{kg}$, adding 0.01 wt% ceramic, e.g. Al_2O_3 (density $\rho = 3.0\,\mathrm{g\,cm^{-1}}$), particles with size $d = 1\,\mu\mathrm{m}$ will give [7]:

- mass of a single particle $m_p = 4/3\pi r^3 \rho = 1.57 \times 10^{-12}\,\mathrm{g}$,
- total alumina mass in the melt $m_{Al_2O_3} = 0.01\%\, m_l = 0.001\,\mathrm{g}$,
- number of alumina particles $m_{Al_2O_3}/m_p = 6.4 \times 10^9$.

To have a higher probability of attaining the cavitation regime, these impurities and/or their crevices should be in the same range or larger than the needed cavities. Yet, even much smaller cavities can be excited as it is know that increasing the pressure amplitude facilitates the growth of a bubble [43]. Since all such gas pockets are subjected to pressure oscillations and a net increase over a period through the rectified diffusion, if sufficiently large pressure amplitude is applied, for a moment these cavities can surpass the critical radius after which the bubble growth would become explosive [80].

Table 3.1 also shows the disparity of the critical bubble radius for metals compared to water – the surface tension plays the dominant role determining the lower end for a cavitating bubble radius. As such, the critical pressure needed for smaller bubbles is much larger in metals than in water. Bubble growth with $R = R_B$ in iron depending on variation of P_A during 1.5 period is shown in Figure 3.17. Pressure values are depicted on the right side. The inset shows the initial oscillations for the first half-period. With lower $P_A = 100$ kPa the bubble radius never reaches a critical value and the oscillations stabilise. With increased amplitudes, the bubble undergoes larger expansion phases followed by steep collapses and successive after bounces. With the largest expansion amplitudes, bubbles, most likely, exist only for few cycles.

Oscillations of a smaller bubble $R = R_B/5$ are shown in Figure 3.18. It is clear that to cavitate a smaller bubble, much larger pressures are needed. At the same time, when the critical value is reached, the response in growth is also more dramatic. For comparison, while for $R = R_B/5$ roughly four times larger P_A is needed than for $R = R_B$, when the critical value is reached at 600 kPa, the growth of the bubble R/R_0 increases twice. Thus, it is essential to reach the highest P_A possible to be able to obtain these extreme collapses within a larger bubble size range.

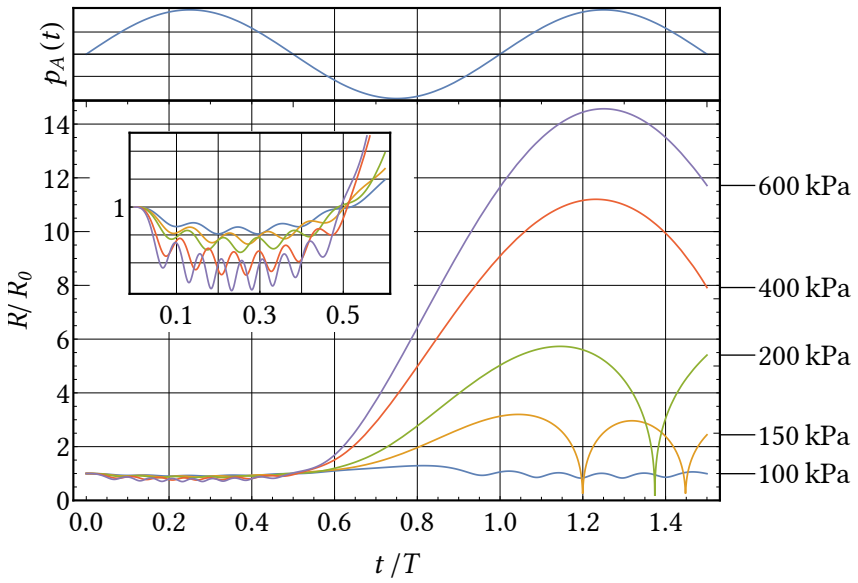

Figure 3.17.: The radius/time plot showing the response of a bubble with initial radius $R_0 = R_B = 18\,\mu m$ for different applied pressure amplitudes P_A inside liquid iron during 1.5 periods. The top plot shows the sinusoidal sound pressure oscillation. The bubble is subjected to a 14 kHz sound field. The bubble radius is calculated with the Rayleigh-Plesset equation. The numbers on the right side denote P_A in kPa and the inset shows the oscillations for the first half-period.

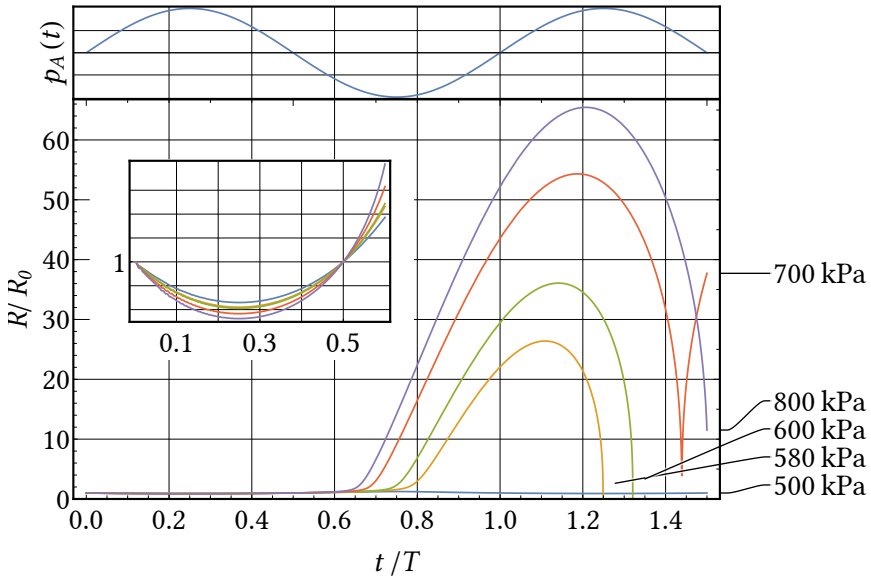

Figure 3.18.: The radius/time plot showing the response of a bubble with a radius $R_0 = R_B/5$. All other parameters remain the same as in Figure 3.17.

4. Particle dynamics in electrodynamically forced flow

It is a key requirement to understand the complex, multiphase liquid metal flow for the development and optimization of MMCs production by the liquid metal route. Thus, as a first step, it is attempted to visualize the melt flow similar to induction melting, as shown in Figure 3.8 (a), with addition of ceramic reinforcements.

4.1. How to visualize multi-phase flows in opaque liquids?

Particle image velocimetry (PIV) is a powerful, nonintrusive tool for flow mapping. The method uses tracer particles which are added to the flow and illuminated to obtain images. The displacement of particles is determined in two consecutive recordings and by knowing the time interval between them the flow can be reconstructed. More importantly, an additional benefit is the necessity to include the particles which makes this method suitable for the particle-laden flows. However, opaqueness of metals limits the conventional light source of PIV – the laser, and for the purpose of investigating particle flow in a liquid metal, a different method must be employed.

To obtain information about flow structure inside non-transparent liquids using particle tracking methods, x-ray imaging has been used with good success [86], [87]. Additionally, because of different lightning mechanisms, particles can have a large size distribution which makes it more suitable for real life applications where particles are not strictly equisized while traditional PIV needs monodispersed particles. However, since x-rays are attenuated relative to the materials density, heavier elements provide a challenge for multiphase flow inspection. Additionally it is almost impossible to trace particles of similar density as the liquid metal.

Contrary to x-rays, neutrons interact on the level of the nuclei, therefore, they are sensitive to light atoms, but at the same time show lower interaction probability with heavy metals, thus, allowing higher penetration depths than x-rays. This physical difference leads to different attenuation coefficients for neutrons μ_n and x-rays μ_x (for a good comparison one is referred to Figure 1 in [68]). The beam attenuation in a medium is governed by Beer-Lambert law,

$$I = I_0 \mathrm{e}^{(-\mu_{n,x} d)}, \tag{4.1}$$

where d is the thickness of a sample in the beam direction, I_0 and I are the intensities of the beam before and after passing through the sample, respectively. For example, according to equation (4.1) a 30 mm thick layer of gallium will leave 25% of the initial intensity of a neutron beam ($\mu_n = 0.49$) whereas using x-rays ($\mu_x = 1.42$) leaves only 1% of the intensity.

Thus, as long as an access to a neutron source is available, the use of a neutron beam appears as an attractive alternative for researching particle-laden liquid metal flows.

4.2. Experimental set-up and procedure

The experiments have been performed at the Swiss Neutron Spallation Source (SINQ) NEUTRA beamline in the Paul Scherrer Institute (PSI) using thermal neutrons (25 meV thermal Maxwellian spectrum), with maximum proton current of 1.8 mA and neutron flux in the order of $10^7 \mathrm{cm}^{-2}\mathrm{s}^{-1}$. 200 µm thick 6 Li doped ZnS scintillator screen is used to produce light when excited by ionizing radiation. Images are recorded with a sCMOS camera detector (Andor Neo, pixel size 6.5 µm) together with a Nikon AF-S NIKKOR 50 mm 1:1.4 G lens. The effective number of pixels is 2048 × 2048 with a pixel (px) size of 0.13 mm with binning 2. A more detailed description of the facility can be found in [88].

For successful velocity measurements in the melt the tracing particles should have a similar density to the fluid, but at the same time the highest attenuation difference between both materials should be achieved. However, in MMC applications the density ratios vary for different reinforcements, thus, it is not possible to model all possible combinations and some compromise must be found. Gadolinium (Gd) has been chosen as the main tracing element. It has one of the highest attenuation coefficients ($1479\,\mathrm{cm}^{-1}$), which means that the highest contrast between the particle and any liquid metal can be achieved, but at the same time a comparable density ($7.9\,\mathrm{g\,cm}^{-3}$) with liquid metals that can be used in experiments.

Conventional melting equipment can not be employed because of the size, cooling and 2D imaging limitations. Hence, the solenoidal inductor which is used in the induction crucible furnaces is replaced by two pairs of counter-rotating permanent magnets at the sides of the vessel, which leaves the beam line free of any set-up periphery. A 2D axially symmetric flow – four counter-rotating vortices which correspond to the toroidal vortices observed in a cross-section of an induction crucible furnace – are simulated in the plane perpendicular to the neutron beam. A schematic drawing of the set-up can be seen in Figure 4.1. The experimental set-up has been designed and built by Dr. Mihails Ščepanskis (Institute of Physics University of Latvia (IPUL), now CENOS LLC). Magnets (2) with a diameter of 30 mm and 1.3 T large remanence are magnetized radially. A rotation speed of 420 – 1900 rotations-per-minute can be provided. To avoid additional beam attenuation, the vessel (1), depending on the experiment, is produced from a window glass or stainless steel as it is important that the material does not chemically react with the used liquid metal. The inner dimensions of the vessel are the following – length is 100 mm, height is 100 mm, width is 30 mm. Detailed description of the system can be found in a dedicated report [89]. Two experiment campaigns have been conducted by a team of scientists from IPUL together with the author.

The first experimental campaign is limited to finding the necessary flow velocity and structure for the most optimal particle admixing, as well as the limits imposed by NEUTRA. Pure gallium (density $6.095\,\mathrm{g\,cm}^{-3}$ when molten) has been used as a model liquid because of its low attenuation coefficient as well as its low melting temperature. Tracing particles have been created by mixing Gd_2O_3 and Pb powders with adhesive (wt% of 6%Gd_2O_3-10%

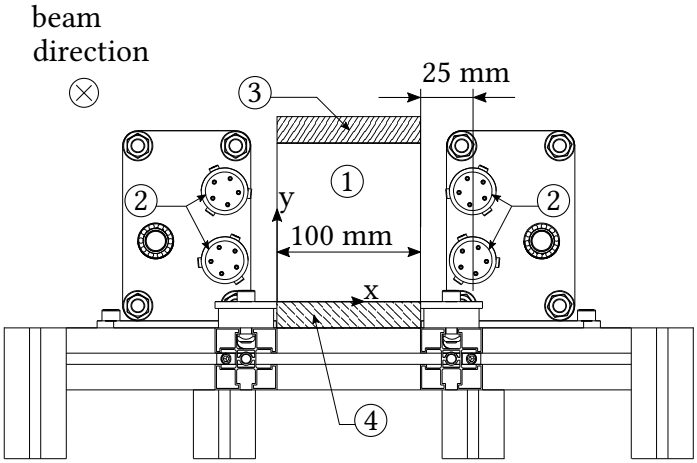

Figure 4.1.: The scheme of the experimental set-up with four counter-rotating magnets (2) and with added heater (3) and cooler (4) to the liquid metal vessel (1). Neutron beam is directed into the plane.

adhesive-84%Pb) to obtain an average density of 6 g/cm^3 and afterwards ground and separated according to sizes < 160 µm, 160–400 µm and > 400 µm. A glass vessel is used in this experiment.

The task in the subsequent campaign is to understand how the reinforcement particles are entrained in the metal matrix. The metal is exchanged from Ga to Sn for better control of solidification, and a resistance heater and cooler have been added to the set-up ((3) and (4) in Figure 4.1, respectively). For safety reasons the vessel is changed from glass to a stainless steel one. Pure Gd spheres with a diameter of 355–500 µm are used as the tracer/reinforcement particles since the adhesive is not stable at elevated temperature. The choice of size is based on the previous experiment, where this was found to be the optimal range for particle tracking limited by the spatial and temporal resolution of the instruments in NEUTRA.

4.3. Image processing

Typical raw images from the experiments can be seen in Figure 4.2 – the first (a) and the second (b) measurement campaign, respectively. Image preprocessing is done with Fiji. Firstly, 1 px sized black and white outliers have been removed to reduce the salt-and-pepper noise. Nevertheless, a lot of random noise is left, therefore, each background pixel that deviates from the median by more than a certain value has been replaced by the median intensity value of the surrounding pixels. Finally, a slight smoothing using a mean filter has been applied. Figure 4.3 (a) shows a processed image before applying PIV. It is clearly visible that light intensity for a single particle is comparable with that of the noise which makes it nearly impossible to apply single-particle tracking tools in this case.

For PIV x- and y- velocity components are obtained using cross correlation of images in PIVview2C 3.3.2 from PivTec. A 16x16 px window size with 8 px step size is chosen. The region of interest is limited to 100×100 mm (the size of vessel) that corresponds to

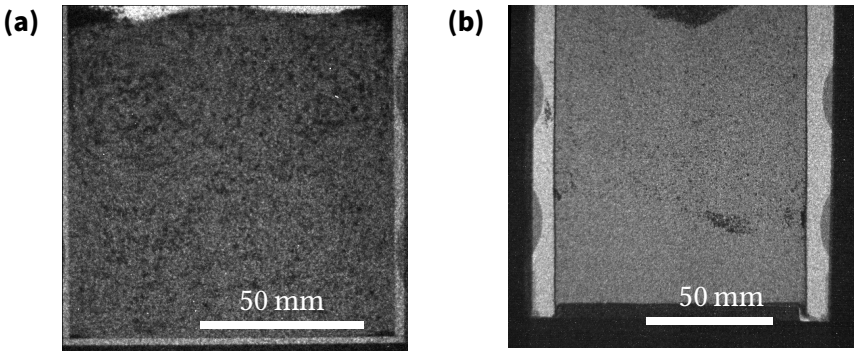

Figure 4.2.: Recorded raw neutron radiography images: (a) the first measurement campaign to test the set-up and the concept, and (b) solidification and particle entrapment experiment. Image exposure time 10 ms.

480×460 px. Multi-grid interrogation method is used with initial sampling window of 96×96 px. Images are interpolated with B-Spline interpolation scheme with order of 3 and the peak search is done by a least squares Gauss fit. Outliers are detected and then re-evaluated with larger sample window size and replaced if evaluation is successful. Approximately 25% of all vectors are left as outliers in the end. The obtained velocity field is then visualized using Mathematica 11.3. An example of a mean velocity field u averaged over a 30 second experiment obtained with PIV can be seen in Figure 4.3 (b). Such flow structure is obtained with magnet rotation frequency of 35 Hz with 10 ms exposure time.

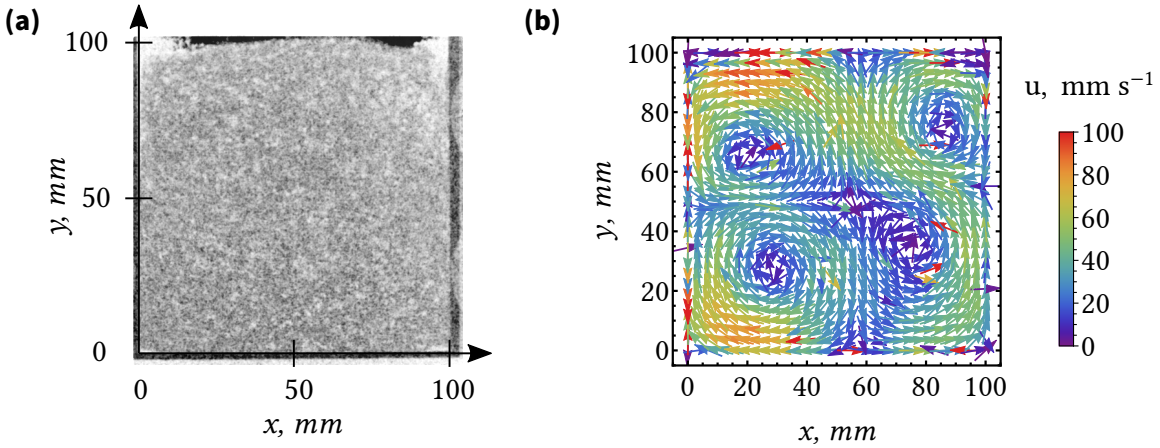

Figure 4.3.: Processed neutron radiography image (a) with the resulting mean velocity field (flow averaged over 30 seconds) by applying PIV (b); u denotes the velocity magnitude. The flow obtained with a 35 Hz stirring rate. Image exposure time 10 ms.

Note that the neutron radiography PIV results presented in this work are based on the same post-processing and analysis as the well known optical method using the conventional light sources, however, neutron radiography images processed with the PIV algorithm lack the precision of the latter. With conventional laser PIV systems optical resolution of 0.03 mm/px with frame rates up to 1000 Hz can easily be reached [90], while neutron PIV has 0.1 mm/px and up to 100 Hz, respectively. The low spatial resolution due to the

sensitivity of the scintillator prevents using small particles. Furthermore, the low neutron flux creates high noise which substantially reduces the contrast-to-noise ratio (CNR) for the obtained images. The CNR is a ratio of a signal intensity difference between a particle and the local background and the noise level for the whole image

$$CNR = \frac{|I_p - I_S|}{I_\sigma} \tag{4.2}$$

where I_p is the particle intensity at its center, I_S is the mean background intensity in the vicinity of the particle and I_σ is the standard deviation of the intensity of the whole image. In the results presented in this work, CNR, on average, is 1.5. In order to enhance the particles for PIV processing, some of the noise, e.g. few darker neighbouring pixels, is enhanced as well. This high noise, which can be reduced, but not eliminated, creates flickering artificial particles which then are included in calculating the displacement vector leading to false velocity estimates. Furthermore, the usage of large particles creates an additional inaccuracy since the particles do not faithfully follow the turbulent flow as will be demonstrated later. A rather large velocity difference has been shown to exist between the used particles and the fluid – the terminal velocity of freely raising particles is in the range of 0.8–1.5 cm s^{-1} with larger agglomerates reaching even 3 cm s^{-1} [91].

4.4. The visualization of the flow and particle entrapment

4.4.1. Particle behaviour in an intensively stirred melt

The experimental set-up with the four counter-rotating magnets (Figure 4.1) is used to create a flow in a rectangular vessel similar to the one observed in the induction melting furnaces. In Figure 4.4 snapshots of different stirring rates, i.e. with different magnet rotation frequencies, can be seen. 400 µm large 6%Gd_2O_3-10% adhesive-84%Pb particles are inserted in liquid gallium. The complete experimental run is graphically shown in Figure 4.5, where dots represent the corresponding snapshots in Figure 4.4. The first admixing of particles is done with 35 Hz (Figure 4.4 (a)). At the start, even with the highest mixing rate it is impossible to achieve a homogeneous dispersion of the particles. By the effects of buoyancy, non-wetting behaviour and the high surface tension of Ga, the inclusions simply float. Although the flow velocity is high enough to pull in some particles as agglomerates, the shear forces are not strong enough to break apart the 10 mm large clusters.

During the 730 seconds long experiment, the mixing rate is varied as shown in Figure 4.5 – the melt stirring is gradually increased and decreased to investigate how particle admixing changes. It can be observed that the wetting has been greatly improved between (a) and (b) when the same intensive stirring rate is applied after long time of mixing. Most likely, the crevices of the particles are slowly filled with the metal due to the prolonged exposure to the shear stresses inside the liquid. While not perfectly dispersed, compared to the first snapshot (a) more and smaller agglomerates are inside the volume. Furthermore, the particle amount introduced in the melt with the lowest stirring rate (e) is larger than at the start of the experiment with 35 Hz (a). It clearly proves the importance of a strong wetting behaviour needed to pull in and admix the particles. Uncoated particles are

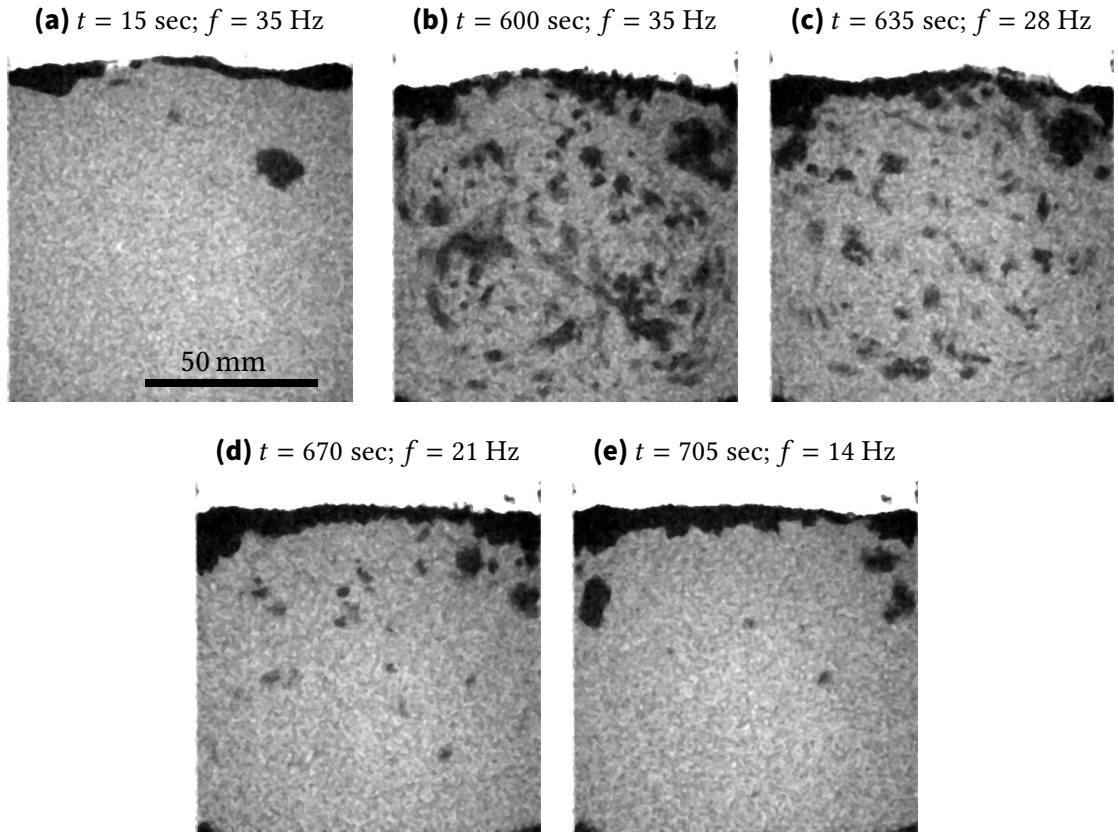

Figure 4.4.: Image sequence of mixing of non-wetted 6%Gd_2O_3-10% adhesive-84%Pb particles in liquid gallium. Flow depending on different stirring rates, i.e. permanent magnet rotation frequency, is shown: (a) 35 Hz, (b) 35 Hz, (c) 28 Hz, (d) 21 Hz, (e) 14 Hz. The experiment timeline is given in Figure 4.5. Total processing time is 730 seconds. Image exposure time is 25 ms.

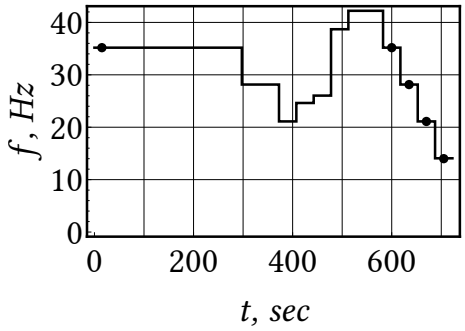

Figure 4.5.: The timeline of non-wetted particle admixing experiment in liquid Ga using different magnet rotation frequencies. Dots represent the corresponding snapshot in Figure 4.4.

impossible to disperse uniformly without additional pre-processing, and they admix as large clusters. This statement is true for the used particles in liquid Ga, but the research done with high temperature melts reported later in the work suggests that it also stands for other materials.

To improve the particle admixing, a layer of liquid Ga is mechanically applied to the particles. The mixing of such particles with different sizes with low and high mixing frequencies can be seen in the snapshots in Figure 4.6. Clearly, the particles are now dispersed evenly and without clustering. Comparing figures with different mixing frequencies, it can be seen that the faster flow created by more intensive stirring brings more particles inside the volume – the flow driving force must overcome the buoyancy force and flow velocity has to be larger than the terminal velocity of the particles for a successful admixing. Thus, to disperse particles in liquid metals, importance lies not only in the wetting and physical and chemical compatibility between the particles and the liquid, but also on the flow characteristics and topology (the discussion about topology is outside the scope of this work and interested readers are referred to [68]).

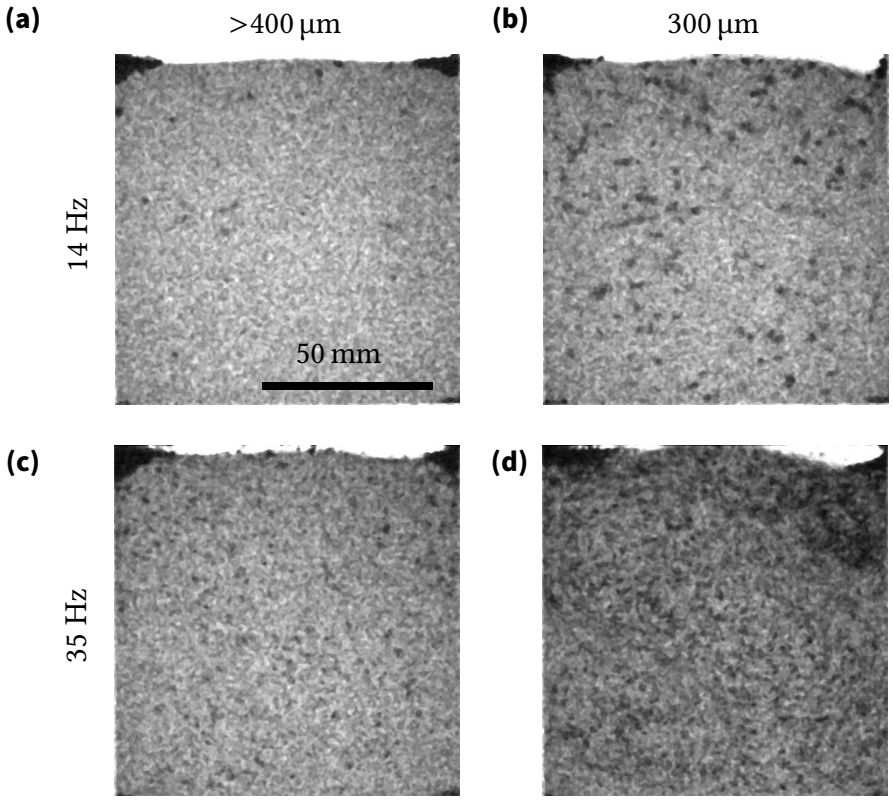

Figure 4.6.: Admixing of gallium coated 6%Gd_2O_3-10% adhesive-84%Pb particles of different sizes in liquid gallium. Flow obtained with different stirring rates: (a) particle size > 400 μm, 14 Hz, (b) ~ 300 μm, 14 Hz, (c) > 400 μm, 35 Hz, (d) ~ 300 μm, 35 Hz. Image exposure time is 25 ms.

The flow structure and velocities in the neutron radiography experiment have been obtained using PIV as described in section 4.3. These results are compared with ultrasonic Doppler velocimetry (UDV) measurements performed by Reinis Baranovskis from IPUL.

GaInSn ($\rho = 6.58\,\mathrm{g/cm^3}$, $\eta = 2.2\,\mathrm{mPa\,s}$ at 300 K [92]) has been used as liquid metal in UDV experiments. The comparison of the maximal vertical velocity component v_{max} at the coordinate (50, 25) mm (for the coordinate system refer to Figure 4.3 (a)) can be seen in Figure 4.7, and a large disparity between the results is observed. To describe the flow in dimensionless quantities, the Reynolds number is introduced as $\mathrm{Re} = v_{max}L/\nu$, where L is the half-length of the vessel and ν is the kinematic viscosity of the fluid. In the current case the characteristic Reynolds number is as high as 20000, therefore, the flow is considered turbulent in the vessel which, additionally, improves the homogenization of the volume. Both methods have their limitations, yet, for this comparison, the UDV measurements are considered to represent the real flow velocities better because of the already well established usage [93], [94]. It can be verified by simply tracing a random larger particle *by hand* (Figure 4.8) that the velocity, on average, is in the order of $100\,\mathrm{mm\,s^{-1}}$ with magnet rotation at 21 Hz. Therefore, PIV of neutron imaging underestimates the velocities by a factor of three at higher Re numbers, which can partly be attributed to the low CNR and partly to the not neutrally buoyant particles. Furthermore, there is a substantial interaction between the particles, and these impact events significantly slow down the averaged flow. As the particles in traditional PIV are equisized, usually few µm large and have the same density as the liquid they trace, the flow can be described more precisely. In the neutron imaging, it is more likely that the velocity field of the relatively large particles is obtained which is not necessarily the same for the liquid flow.

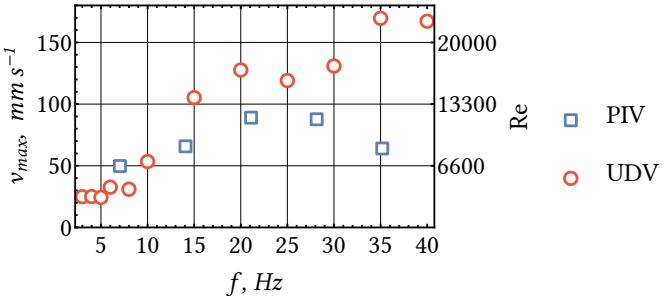

Figure 4.7.: The maximal vertical velocity component v_{max} depending on different magnet rotation frequencies. Comparison between neutron PIV and UDV measurements. Velocity values taken at the coordinate (50, 25) mm. Corresponding Reynolds number given on the right axis.

Qualitatively the visualized flow structure inside the vessel corresponds to the expected one as it is possible to distinguish a four eddy structure (Figure 4.9 (a)) as in the industrial induction furnaces over long time average [95]. Similar flow is also expected in the contactless cavitation set-up (Figure 3.9 (a)). The particle trajectories, however, reveal the complexity and time dependence of the flow. The four vortices pattern frequently (every few seconds) transforms into three eddies - a diagonal vortex can be observed in both directions in Figure 4.9 (b) and (c). This flow transformation into a three eddy structure plays a significant role for homogenization of the inclusions between the upper and lower parts of the melt. While neutron radiography reveals the existence of the turbulent regime and its importance for particle homogenization, quantification of it is still difficult due to the limited precision of the measurement technique.

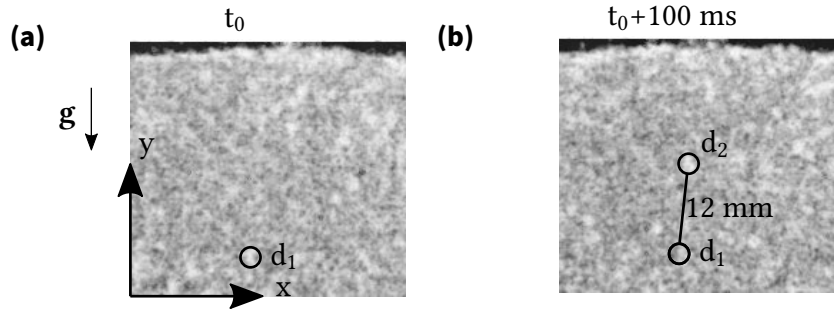

Figure 4.8.: Particle tracking *by hand* with magnet rotation at 21 Hz. Particle moves 12 mm during 10 frames. With exposure time of 10 ms, it gives a particle velocity of 120 mm s^{-1}.

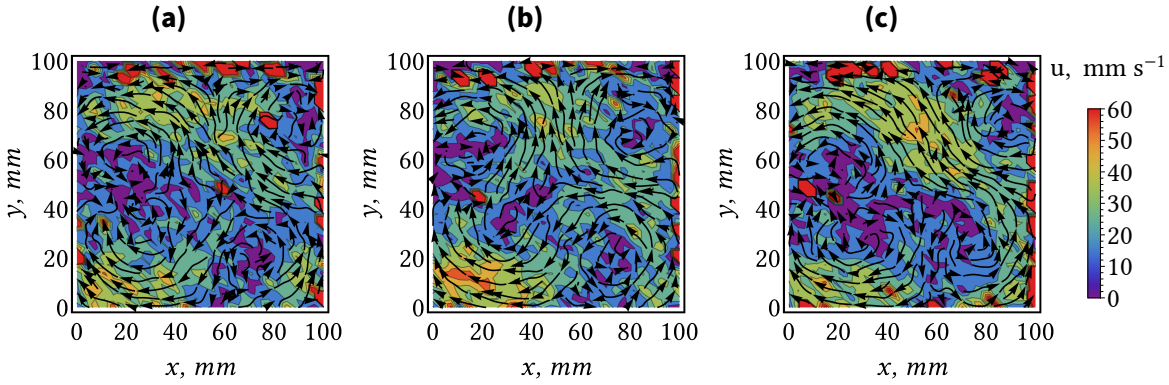

Figure 4.9.: Velocity field averaged over 3 seconds (120 frames with exposure time of 25 ms) showing highly varying 4 vortex structure: 4 separate vortices recognizable in (a), while transformation to 3 vortex structure in opposing directions observable in (b) and (c). Magnet rotation set to 35 Hz.

The large discrepancy between the UDV and neutron PIV means that to obtain quantitative results using PIV, the experimental procedure has to be significantly improved regarding particle seeding as well as post-processing. Yet, for the first-of-their-kind experiments the results are still beneficial and, for example, allow to explore particle behaviour in a turbulent liquid metal flows. A further improvement can be done with optimizing neutron instruments, e.g. a higher neutron flux significantly improves the PIV results by increasing the CNR, as presented in [91].

4.4.2. Particle entrapment by the solidification front

The first neutron flow tracing experiment showed the high velocities needed for bringing the particles inside the melt. Additionally, the importance of wetting by the liquid has been observed. The objective of the second experiment is to observe a directional solidification of a composite. A solidification experiment of liquid metal, influenced by high rate stirring, has been already reported using Ga [96]. While Ga has also been tried in this experiment, the solidification is too time consuming (in order of hours). Henceforth, tin has been used as an alternative liquid for more efficient experiments. However, the problem of particle insertion remains, as in the first experiments. Coating particles with Sn is not trivial, therefore, to improve the wetting, they are again mechanically covered with a layer of Ga. The drawback of such approach is the addition of Ga inside Sn creating an Sn-Ga alloy. Yet, as it will be shown, the alloying emerges to be preferable for particle entrapment.

The vessel is cooled from the bottom with a water cooled heat sink, Sn is melted with a resistive heating element from the top, which is turned off during the solidification. The image sequence of tin solidification using mixing with 50 Hz is presented in Figure 4.10. In this case 355 µm large Gd spheres are used as tracers/reinforcement phase. For the first two minutes there is no capturing of the particles by the solidification front, which is approximately marked with the black line. It can be observed that the particles are not even affected by the front, and it acts as a solid wall as shown in the image sequence in Figure 4.11. The particle (white spot marked with black circle in each frame) approaches the solidification front (approximately marked with the black solid line) with velocity of around $90\,\mathrm{mm\,s^{-1}}$, slides along it and then returns into the volume. The velocity before, during and after the sliding remains the same.

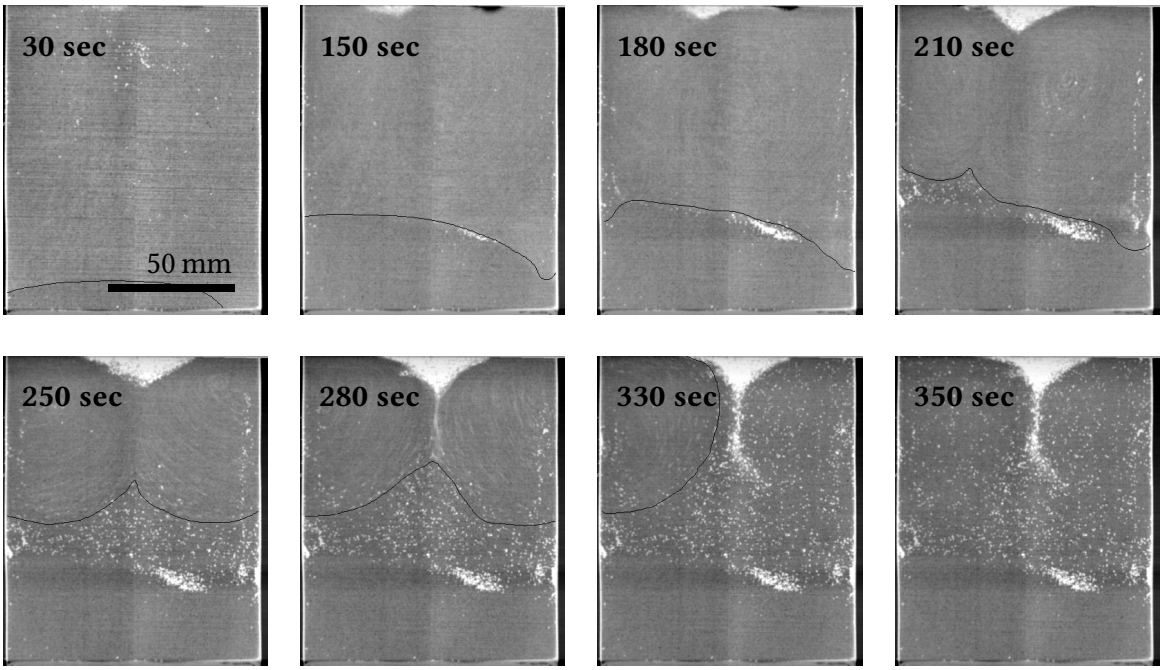

Figure 4.10.: Snapshots of tin solidification with 50 Hz mixing frequency. The solidification front is approximately marked with a solid line. Images are obtained by 100 frame averaging, which allows to clearly see the solid phase and the entrapped particles (white dots). The skewed solidification front is a result of a possible slight asymmetrical positioning between the magnets and the uneven cooling.

As the solidification front keeps growing, some particles are entrapped. First agglomeration develops on the right side while afterwards a relatively equidistant distribution can be observed. Since the vorticies are pulling the particles inside the melt from the free surface, a stream of agglomerates develops and solidifies in the middle. The flow itself becomes symmetric as expected from the previous experiment, yet, the right side solidifies faster. This might be caused by antisymmetric centering of the vessel (the flow is sensitive to the positioning distance from the magnets) and an uneven cooling by the cooler.

Tracing of a particle that gets entrapped is shown in Figure 4.12. While in Figure 4.11 the particle just slides over the solidification front, in 4.12 it gradually is slowed down from 60 mm s^{-1} to a complete stop. In this case, there is no clear solidification front, but instead a higher viscosity zone with a considerable thickness has developed. Naturally, such transition zone does not occur in pure metals. In this experiment, Sn cannot be considered pure since a substantial amount of Ga is added together with the particles, and the overall composition of the melt has been changed. However, why the zone appears only after two minutes of cooling? The occurrence of the higher viscosity layer can have multiple explanations. Firstly, the continuous high rate mixing brings metallic oxides from the surface in the volume. The melt becomes a foamy, slurry-like structure with an increased viscosity. Secondly, during solidification of alloys, dendritic growth occurs when the system in front of the solidification front becomes undercooled because of segregation of alloying elements that locally reduce the melting point. This semi-liquid part, or mushy zone, can significantly damp the flow in the vicinity while also slowing

down the particles. Lastly, the high stirring rate provokes a grain refinement [97] – as the solidification progresses the dendrites grow longer until a breakdown of the arm occurs due to the forced convective flow. The broken tips are brought into the melt and serve as new nuclei for solidification. A high density of such broken dendrites can create a slurry effectively increasing the viscosity of the melt. However, most likely the formation of this higher viscosity zone is a combination of all mentioned explanations.

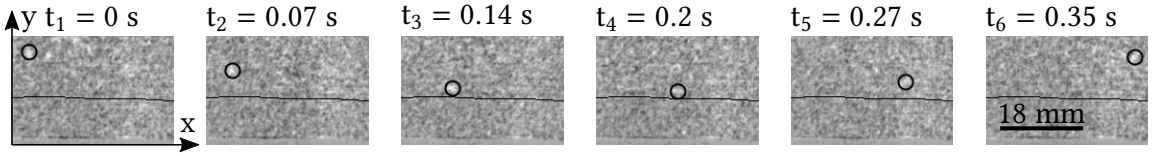

Figure 4.11.: Particle behaviour near solidification front at the start of the experiment. Magnet rotation 35 Hz. With exposure time of 10 ms, a particle travels 37 mm in 36 frames (circled in the snapshots), which gives a particle velocity of 90 mm s^{-1}. The solidification front is approximately marked with the black solid line.

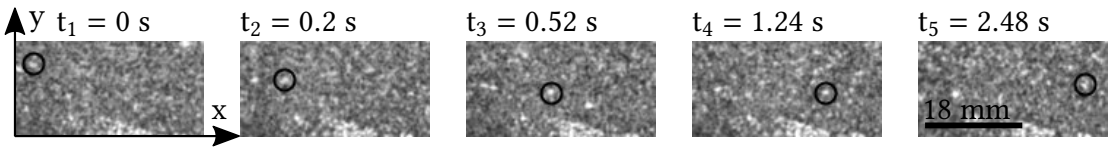

Figure 4.12.: Capturing of a particle by the higher viscosity zone. The time difference between frames: 1-2 0.2 sec, 2-3 0.32 sec, 3-4 0.72 sec, 4-5 1.24 sec. The particle is slowed down from approximately 60 mm s^{-1} to rest when entering the solidification zone. Experimental parameters are the same as in Figure 4.11.

Quantitatively, again the PIV shows its limitations as the high velocities can not be resolved properly. However, the flow structure is well described, as seen in Figure 4.13. For example, at the start of the experiment (Figure 4.13 (a)), when almost all of the volume is liquid, 4 vortices have developed. The bottom ones are influenced by the developing solidification zone (region with 0 mm s^{-1}). At the same time, the right vortex at the top has expanded over the symmetry line and overtakes the left one. The reason for such asymmetry, as mentioned earlier, are slight imperfect experimental conditions. The flow velocity, similarly to the previous experiment, is also greatly underestimated. Comparing maximum value from Figure 4.13 (40 mm s^{-1}) to estimation from Figure 4.11 (90 mm s^{-1}), the velocity differs by a factor of 2. However, when more than half of the volume is solid and the top vortices are slowing down due to the increasing viscosity, the velocities can be resolved better. In such case PIV can also be used to estimate the height of the more viscous zone which has developed. From Figure 4.13 (b) it can be found that the velocities drop from their maximum value to zero in approximately 20 mm which then is the height of the zone.

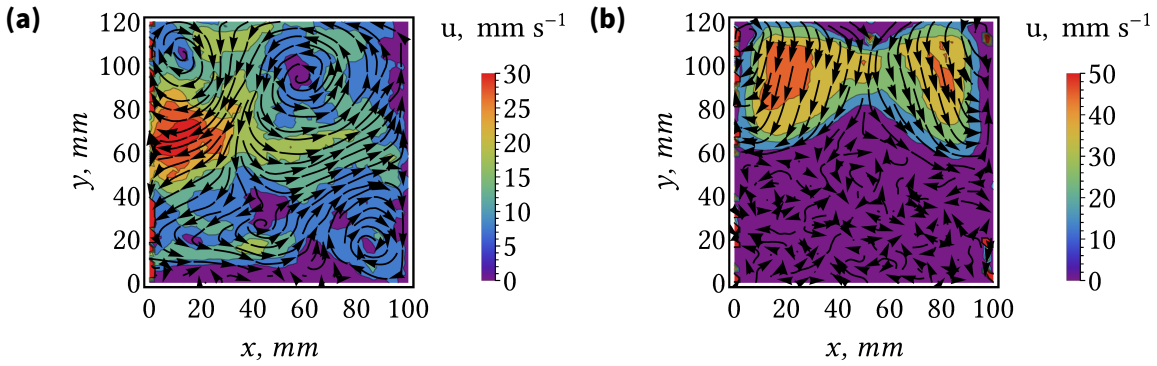

Figure 4.13.: PIV applied at the start of the solidification experiment (a) and at 280 seconds (b). A clear difference between solid, where velocity is correctly given as 0 mm s^{-1}, and liquid parts can be seen.

Such PIV images can be used to obtain the height of the liquid-solid interface. While at fast flow rates the velocity measurements are not reliable, in the solid region the average velocites will be zero. An image sequence of liquid-solid (red-blue) phases and the growing of the interface is given in Figure 4.14. The solidification front is clearly visible and distinguishable. The advancement of the front as a function of time has been measured and can be seen in Figure 4.15. This allows for a more precise investigation of the solidification process. The solidification rate up to 300 seconds is fairly linear on both sides with average solidification rate of 0.2 mm s^{-1}. After 200 seconds the middle part starts to solidify with an increased rate of 0.7 mm s^{-1}. At this moment also the particles are getting entrapped in the metal matrix – a more viscous zone has developed. The zone grows larger as more volume solidifies, essentially slowing the flow and the particles. After 240 seconds, the melt starts to solidify in the center antiparallel to the flow – by now the whole liquid zone is most likely undercooled. The last two vortices solidify rapidly with around 6 mm s^{-1} high rate. It can be noted that before complete solidification, the particles are significantly slowed down – from 100 mm s^{-1} (order of magnitude) at the start of the experiment to less then 10 mm s^{-1}.

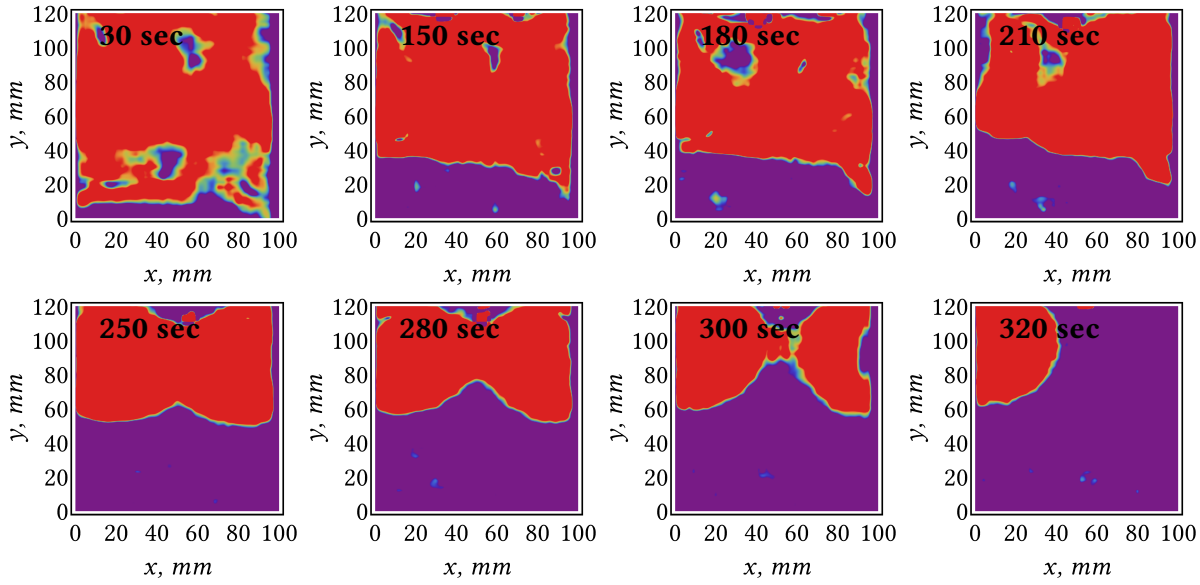

Figure 4.14.: Advancement of the solidification front obtained using the PIV approach. The solid-liquid (blue-red) phase difference can be clearly observed which permits to track the front. The measured advancement of the front is shown in Figure 4.15.

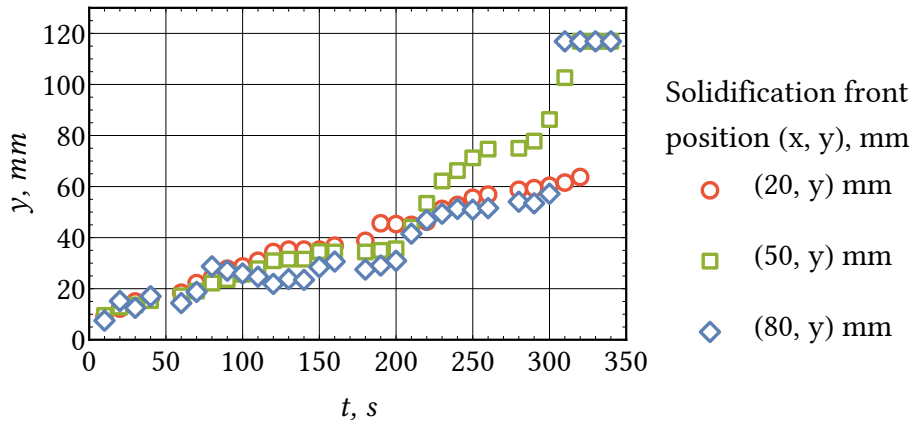

Figure 4.15.: Measured temporal advancement of the solidification front obtained from series of PIV images, as in Figure 4.14. The front is compared along three lines – through the left eddy with coordinates (20, y), middle with (50, y) and through the right eddy with coordinates (80, y).

4.5. Synopsis of the effect of the flow on particle entrapment

The first visualization experiments of a turbulent flow by neutron radiography have proven the strength and usefulness of this approach. Yet, the spatial and temporal resolution of the measurement technique has to be improved to provide more accurate velocity values as well as to quantify the turbulence degree. This mainly depends on the used neutron instrumentation, and, for example, it has been already shown that a higher neutron flux significantly improves the resolution [91], considerably enhancing the precision of neutron

PIV. Furthermore, the measurement technique can be made better by suitably adjusting the particle properties and the seeding.

The conducted experiments have clearly shown the importance of particle wetting. Because of the buoyancy, the high surface tension and a complete rejection by the melt, particles agglomerate and float. A high stirring rate has to be applied to admix them into the melt, however, having a bad wetting behaviour means the particles are pulled in as clusters. Furthermore, as clusters have higher terminal velocity, they are more likely to leave the volume if moved to a lower velocity zone, e.g. near the sides of the vessel or in between the vortices. The situation completely changes if particles are pre-processed by coating with a layer of liquid metal. In this case they can be stirred in with ease, agglomeration can be prevented and a good dispersion can be achieved.

While the neutron PIV underestimates the flow velocity, it can quite well be used for other purposes, e.g. determining the flow structure or tracking of the solidification front. A routine to follow the front has been proposed and successfully applied to obtain its development in time.

For particle admixing and homogenization in the volume, a high flow velocity is necessary. Furthermore, the turbulent nature of the flow improves the dispersion because of the mass transfer between the vortices. While high velocities are needed to draw the particles into the melt, they also need to be slowed down for an efficient entrapment. The experiments have shown that with a pure melt, particles are not entrapped in a solidifying material, and they simply bounce off the solidification front. A zone with increased viscosity with a significant thickness is needed to capture the particles. Of course, beforehand, a good wetting of the particles by the liquid metal has to be achieved.

5. Contactless magnetic initiation of cavitation in high melting point metals

The proof of principle of creating an oscillating force field by superimposing a steady magnetic field on the induced magnetic field has been shown in section 3.1. However, a potential weakness has been identified by the MHD analysis in section 3.2 showing a possibly weak homogenization of the melt and particle segregation due to the high flow damping resulting from the static magnetic field. In contrast, the visualization of particle behaviour using the neutron radiography has shown the necessity for a turbulent flow and mixing of the whole volume, while also highlighting the importance of particle-matrix compatibility, i.e. a good wetting has to be ensured. Furthermore, the high pressure amplitudes needed to facilitate bubble growth have been recognized in section 3.3. In the following chapters the question whether cavitation can be realistically created in a contactless way in high melting point metals and its ability to support particle dispersion will be investigated. The discussion is started with presenting the experimental set-up and studying the cavitation initiation by recording the emitted acoustic signal.

5.1. Contactless cavitation set-up

5.1.1. Low magnetic field

A sketch of the experimental set-up designed by Dr. Ilmārs Grants (Helmholtz-Zentrum Dresden - Rossendorf (HZDR), now IPUL) for low magnetic field (LMF) experiments is depicted in Figure 5.1. A compressed tablet (1) consisting of the matrix material and reinforcement powder (a concept similar to insertion of a solid master alloy for grain refinement) is placed in between two supports (2) which are made of the required matrix material and are partly melted together with the tablet creating a composite. The process conditions are similar to floating zone melting. The melting is done in an evacuated cell, which is enclosed by a quartz tube (3) from the sides and water cooled copper plates (4) from top and bottom. This gives the ability to partly control the solidification rate as well as how much of the sample will be melted. Additionally, the copper plates act as a shielding of the alternating currents from the induction coil (5) for the electromagnet poles (6), which direct the steady magnetic field. The piezo elements (7) used to record the cavitation are placed in grooves in the shielding plates. While the liquid metal zone would be kept in place by the magnetic pressure, in practice this may not be the case and for safety reasons a refractory material is placed between the melt and the quartz tube.

Two different low field electromagnets have been used – first test experiments have been carried out with a magnet with a maximum magnetic flux density up to $B_z = 0.5\,\mathrm{T}$

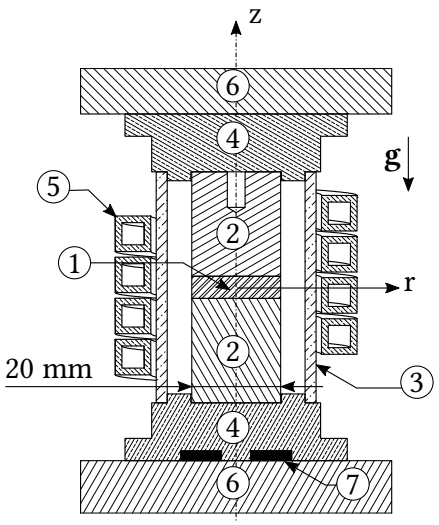

Figure 5.1.: The sketch of the experimental set-up used: (1) tablet containing the powder and matrix mixture, (2) supports from the matrix material, (3) quartz tube, (4) water cooled copper shielding plates, (5) induction coil, (6) electromagnet poles, (7) position of the piezo elements.

with a 8.5 cm pole distance. A major limiting factor is the run-time as the used magnet heats up and has to be turned off after 20 minutes of operation. With improved knowledge about the processing, the experiment has been moved to a larger electromagnet which can provide a magnetic flux density up to $B_z = 0.8\,\mathrm{T}$ in a 10.8 cm gap between pole shoes, and has no limit for the duration of the experiment.

5.1.2. High magnetic field

As shown in Figure 3.17 in section 3.3, a pressure amplitude P_A of 80 kPa is barely sufficient for cavitation onset in liquid iron. Furthermore, Table 3.1 shows that the effective range of cavitating bubble sizes decreases with increasing surface tension and density, and it is clear that the cavitation is much more difficult to obtain for heavy metals. To be certain about the onset and to be able to reach the transient threshold, additional experiments are conducted in a high magnetic field (HMF). The possibility of a manyfold increase of the steady magnetic field allows to investigate the characteristic features of cavitation in heavy metals by increasing the radial force and, thus, the pressure amplitude P_A.

These additional experiments are conducted in the Dresden High Magnetic Field Laboratory (HLD) in Magnet E (Oxford Instruments superconducting magnet system). The magnet is 2290 mm long with a 150 mm large bore diameter. The magnetic flux can be increased step-wise up to $B_z = 19\,\mathrm{T}$. The superconducting coils are immersed in liquid helium and the temperature is kept around 4 K. A direct insertion of the previously used experimental set-up is not possible, thus a modified melting cell has been constructed. The scheme of the set-up, constructed by Stefan Findeisen (HZDR) in close cooperation with the author, is shown in Figure 5.2.

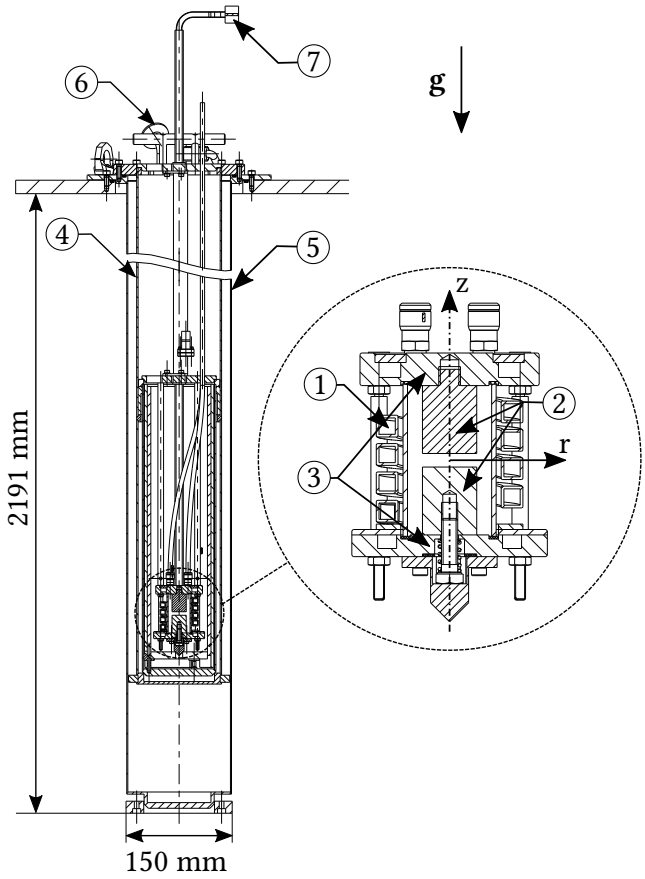

Figure 5.2.: The scheme of the set-up used in the superconducting magnet with the melting chamber zoomed in the circle on the right side: (1) AC induction coil, (2) supports from the matrix material where tablet is placed in-between, (3) water cooled copper shielding plates, (4) inner shielding tube from copper, (5) outer stainless steel tube, (6) vacuum connection, (7) connector to the power supply for the induction coil.

Since the melting temperature can reach up to 1600 °C, additional safety measures have to be undertaken to prevent the evaporation of helium. A multi-walled chamber, consisting of an inner copper tube (4) for shielding the superconducting magnet coils from induction currents and an outer stainless steel tube (5) which act as a separator between the coolant and the copper tube, is constructed. A vacuum (6) is used as a thermal isolation between the inner and outer layers of the chamber. Additionally, two layers of heat reflective, multi-layered aluminum foil are wrapped around the inner copper tube. Since the maximum field strength is located inside the lower part of the bore, 2200 mm long AC feeding bars (7) for the induction coil (1) have been constructed. All other parts of the HMF melting cell, e.g. copper cooling plates (3) and positioning of the sample holders (2), remains similar to the one used in LMF experiments.

5.2. Raw materials for composite production

To investigate the feasibility of particle dispersion and subsequent production of composites by contactless sonication, different high melting point matrix-particulate systems have been examined. List of the raw powders can be seen in Table 5.1 while the matrix materials in Table 5.2. The choice of specific particles is based on information about the wetting behaviour as well as the stability of the reinforcement phase in the relevant temperatures [36], [98], [99], [100], [101], [102], [103], [104], while the matrix materials are compromised of the most commonly used high melting point metals. Some preliminary experiments to investigate the working principle of the contactless cavitation have been conducted with light metals as well.

Table 5.1.: The list of the used particles.

Compound	Particle size, µm	Melting point, °C	Density, g cm^{-3}
TiC	0.8	3200	4.93
TiN	0.8	2950	5.22
TiB_2	$2-6$	2900	4.52
TiO_2	$0.01-0.03$	1843	3.78
Al_2O_3	0.02	2072	3.99
Al_2O_3 spheres	0.8	2072	3.99
Y_2O_3	$0.03-0.05$	2425	5.01
CeO_2	< 5	2400	7.22
ZrO_2	0.8	2715	5.89
ZrB_2	5	3040	6.09
ZrC	$0.4-1.2$	2700	6.70

While the used reinforcement particles have a good stability at high temperatures and are often used as refractory ceramics, the high melting point metals, e.g. iron and steel, are an extremely reactive environment when in a liquid state. It is known that some of the ultra-high-temperature ceramics, e.g. TiC ([105], [106]) and TiB_2 ([107]) tend to dissolve in the liquid iron under specific conditions. The dissolution highly depends on the carbon

Table 5.2.: The list of used matrix metals. Properties given at the melting temperature [84].

Metal/Alloy	Purity, %	Melting point, °C	Density, g cm^{-3}	Surface tension, mN m^{-1}
Steel 1.4404	-	1375-1400	7.900	-
Fe	99.8	1536	7.015	1872
Ni	≥ 99	1455	7.905	1778
Sn	99.75	231	7.000	544
Al	99.9	660	2.385	914

content in the melt – a higher amount limits the reaction and even favours the wettability. Other ceramics, e.g. Al_2O_3 [102], show limited reactivity in iron. This knowledge is even more scarce when discussing particle behaviour in steel since the concentration of different alloying elements considerably influences the outcome [100]. However, even when the dissolution does take place, it is possible only until the solubility equilibrium is reached after which the rest of the particles are thermodynamically stable [103]. Nevertheless, the composites can also be produced in-situ from the particle precipitation during the solidification [108]. Even in this case preventing particle agglomeration, obtaining a fine dispersion and achieving homogenized structure is crucial for composite production – tasks where cavitation treatment can bring significant improvements.

As it is almost impossible to clearly predict the reaction of a specific particle in a specific liquid melt and there are no obvious ceramics that would be guaranteed to survive during processing, it has been decided to investigate a wide range of particles even if a possible dissolution at some conditions could be expected. Note that the main goal of the thesis consists of contactless creation of the cavitation in high melting point metals and identifying tendencies of its influence on distributing small particles in those melts, rather than a detailed material science analysis of such compounds.

The most important matrix material is steel and it is the most widely produced alloy in the world. Since the main aim of the work is to produce heavy metal composites, steel is the primary target for such investigation. From the wide selection only one of the most common stainless steel grades is chosen – 1.4404 (AISI 316L, Fe-Cr18-Ni10-Mo3). It is clear that one cannot generalize the obtained results with one grade to the whole range, e.g. even a slight change in the composition affects the wettability [100]. Still the obtained results should allow to understand the feasibility of the proposed processing route.

To reduce some uncertainty about the effect of different alloying elements also pure iron has been used as a matrix material. As being base material of steel, a successful admixing of reinforcement in iron would translate to a similar effect in steel. Nevertheless, there is a difference of the wetting properties (just like between different steel grades), e.g. steel shows smaller contact angle compared to iron for specific oxides [102], [103].

Lastly, nickel is one of main alloying elements of steel, with some grades reaching up to 5 wt%. Particle reinforced nickel is not relevant for an industrial application, however, a master alloy could be produced if a good dispersion can be achieved. In such case a solid master sample can be melted together with iron during the alloying phase releasing the already dispersed particles. As good wetting with nickel is achieved beforehand, an increased wettability could be expected and an improved particle distribution in the produced steel might be attained.

While the aim of the work is to create MMCs using the liquid metal route, firstly the problem of inserting the particles must be solved – the strong surface tension of any liquid metal means that the particles will simply float. Powder metallurgy allows a more practical way for insertion – by compacting the particles together with the matrix powder, a small, electrically conducting tablet is created which then can be melted together with the chosen metal.

The first set of tablets with iron and steel matrix have been produced in-house at HZDR. A simple hydraulic press with roughly 95 kN maximum force is used. This allows to create particulate-steel or -iron tablets with densities in the range of 5000–6000 $\mathrm{g\,cm^{-3}}$, which,

however, is lower than that of stainless steel or pure iron, thus a high porosity of the sample is expected. Additionally, a multiple-use dye has been employed. Using this simplified process hinders the reproducibility of the initial tablets, e.g. as throughout cleaning can not be ensured, powder from the previous pressing can remain on the walls of the dye contaminating the subsequent sample.

To improve the properties of the tablets, and, more importantly, the repeatability of the experiments, all of the following tablets have been produced by Fraunhofer-Institut für Fertigungstechnik und Angewandte Materialforschung (IFAM), mostly by spark plasma sintering (SPS). Different particulates have been pressed together with either pure iron or 1.4404 steel using SPS – 12 kN force is applied for 5 hours in 1120 °C in Ar atmosphere. To study the effect of higher porosity in the initial samples on the cavitation strength, additional tablets have been densified with a 12 kN force, but without sintering to possibly entrap more gas inside a tablet. In this way different particulates have been pressed together with pure iron or pure nickel. All the created tablets have a $\varnothing = 20$ mm and thickness of around 5 mm. Ceramic particles amount to roughly 2 wt% per tablet.

The overall list of all the produced tablets can be seen in the Table 5.3.

Table 5.3.: The list of produced tablets

with SPS	
Composition	Produced in
1.4404+Al_2O_3	IFAM
1.4404+ZrO_2	IFAM
1.4404+CeO_2	IFAM
1.4404+TiN	IFAM
1.4404+TiB_2	IFAM
1.4404+TiC	IFAM
Fe+Al_2O_3	IFAM
Fe+ZrO_2	IFAM
Fe+CeO_2	IFAM
Fe+TiN	IFAM
Fe+TiB_2	IFAM
Fe+TiC	IFAM

without SPS	
Composition	Produced in
Fe+Al_2O_3	IFAM
Fe+ZrC	IFAM
Fe+TiC	IFAM
Fe+TiB_2	IFAM
Fe+ZrB_2	IFAM
Ni+Al_2O_3	IFAM
Ni+ZrC	IFAM
Ni+TiC	IFAM
Ni+TiB_2	IFAM
Ni+ZrB_2	IFAM
1.4404+Al_2O_3	HZDR
1.4404+ZrO_2	HZDR
1.4404+CeO_2	HZDR
1.4404+TiO_2	HZDR
1.4404+TiN	HZDR
1.4404+TiC	HZDR
1.4404+TiB_2	HZDR
1.4404+Y_2O_3	HZDR

5.3. Sample processing procedure

The tablet (1) in Figure 5.1 (a) is placed between the metal holders (2) which then are enclosed with a refractory material and a quartz tube. The next steps, however, with improved knowledge about the process, changed and have been fine-tuned during the course of the work to better understand and investigate the underlying phenomena. The work can be split in different Phases:

Phase I – the first trials to create cavitation in various pure metals as well as alloys; observe the effects of the cavitation.

Phase II – first trials with stainless steel and different particles; self-made tablets.

Phase III – experiment moved to a 0.8 T electromagnet; Fe, Ni and steel composite tablets produced by IFAM.

Phase IV – experiments in the superconducting magnet.

After closing the melting cell, it is evacuated and kept at around 0.5-5 mbar in Ar atmosphere to prevent the oxidation of the sample. After placing the melting cell between the magnet poles (or in the bore in HMF), a $I_{AC} = 1300\,\mathrm{A}$ strong current at $f = 14\,\mathrm{kHz}$ frequency is applied to the sample. The frequency slightly varies depending on the used sample and its phase. The maximum r.m.s. current corresponds to roughly $b_z = 0.13\,\mathrm{T}$ induced magnetic field in the center of the coil. For samples in low magnetic fields (0.5 T and 0.8 T), according to equation (3.9), it corresponds to $P_A = 80\,\mathrm{kPa}$ while in the superconducting magnet the oscillating pressure amplitude can reach $P_A = 1.9\,\mathrm{MPa}$. To prevent a complete melting of the samples, they are water cooled from the top and bottom using a Lauda proline RP1845 thermostat. To avoid thermal shock of the parts of the experimental set-up, the current is increased step-wise until the maximal value and then kept constant.

As particle wetting plays a major role in composite production, special care is taken to improve it. The stabilization of the contact angle is not instant (in order of tens of minutes), and in addition it depends on the temperature (lower contact angle in higher temperature) [98], [100]. Furthermore, with increased particle refinement, the forces holding the particles together increase as well [7]. In the end, it is not possible to predict the wetting behaviour for each matrix-reinforcement system as it also heavily depends on the used matrix (pure or alloy) type, the purity of the elements (e.g. O_2 affects the reactivity of the particles), and an addition of different reaction elements (e.g. BN or Al_2O_3 both of which are used as refractory material) that can contaminate the melt. Thus, taking into account that

1. it is not possible to measure the temperature in the used set-up,
2. the purity of the material is usually set by the provider and ranges from $99.0 - 99.9\%$, however, during the handling, production of the parts and the experiment it might be exposed to additional oxidation,
3. additional elements may be included in the melt during the handling and processing,

the pre-sonication melting of the composites is simply done for at least 10 minutes to facilitate the wetting of the particles by the liquid metal and to improve the dispersion.

When the steady magnetic field is turned on and applied to the sample, a high pitch noise arises in the vicinity of the sample due to the interaction between the magnetic field and the induction coil. At the same time the sample starts to vibrate and an additional noise from the cavitation phenomenon may appear. The sample is kept under cavitation treatment for around 30 minutes (processing time has been varied during the course of the work to explore the effect of sonication duration) with all other parameters remaining constant. Lastly, the sample is solidified by slowly lowering the power. A direct control of the solidification rate, however, is not possible.

As every processing parameter, including the melting temperature, solidification rate, composition and surface properties of the reinforcement, the ambient atmosphere and the presence of solutes even in low concentrations [105], affects the dispersion of particles, a certain degree of variance between different samples can be expected. Naturally, this leads to an important question about the reproducibility of the experiments. Many of the parameters potentially influencing the dispersion and/or cavitation onset have been varied and adjusted during the course of the thesis. However, when comparing the effect of different cavitation strengths between a specific particle-matrix pair, the processing parameters are kept the same within the possible limits.

5.4. The search for cavitation

Cavitating bubbles emit acoustic waves, which can be analysed and used to characterize the cavitation [41], [43], [109], [110], [111], [112]. The spectrum of cavitation noise consists of a variety of harmonics (nf_0, $n = 2, 3...$), sub-harmonics (f_0/m, $m = 2, 3...$) and ultra-harmonics (nf_0/m, $n = 2, 3...$ and $m = 2, 3...$) of the fundamental driving frequency f_0. Furthermore, a broadband continuum (background white noise) is present, which becomes more pronounced when approaching the transient threshold. The knowledge about the spectral lines can be summarized as follows. At a low excitation power, a cavitating bubble emits sound at f_0. At higher acoustic pressure, but below the transient threshold, harmonics at $n = 2, 3...$ appear. Care must be taken for interpretation though, as in the used set-up, the double frequency appears from the vibrations arising from the oscillations of the induction coil. Lastly, the onset for the transient cavitation is marked by broadening of the spectral lines, large increase of the broadband noise and appearance of sub- and ultra-harmonics. While many theories try to explain the rise of different spectral lines, the underlying fact is clear – the noise is an indicator for cavitation onset.

As such, the acoustic signal is recorded using Pz27 ceramic piezo sensors with a 4 MHz resonant frequency from Ferroperm which are attached to the copper shielding plates ((7) in Figure 5.1). The electric signal is measured with a Tektronix DPO7104 Digital Phosphor Oscilloscope. Two channels are devoted to cavitation signal measurements while two others are used to measure the supplied voltage with the Tektronix TMDP0200 differential probe and the current with the PEM CWT3LFB Rogowski coil from the induction coil. The signal is acquired in packets of 5000 measurements with sampling rate of 312.5 kHz and transferred to a PC every second.

To find the power spectrum (Figure 5.3 (a)) the measured voltage from the piezo element is transformed to the frequency domain using the discrete Fourier transform, while plotting

all of the obtained spectra versus time allows to create a two dimensional image which shows the dynamics of the recorded sound signal during the whole experiment (Figure 5.3 (b) bottom). The provided example image presents a captured cavitation phenomenon – the recorded acoustic spectrum in (a) at around 2400 s and marked with a dashed line in (b) clearly show a sub- ($f_0/2$) and ultra- harmonics ($3f_0/2$, $5f_0/2$) of the driving frequency $f_0 = 14\,\mathrm{kHz}$ – one of the indicators of a transient cavitation phenomenon.

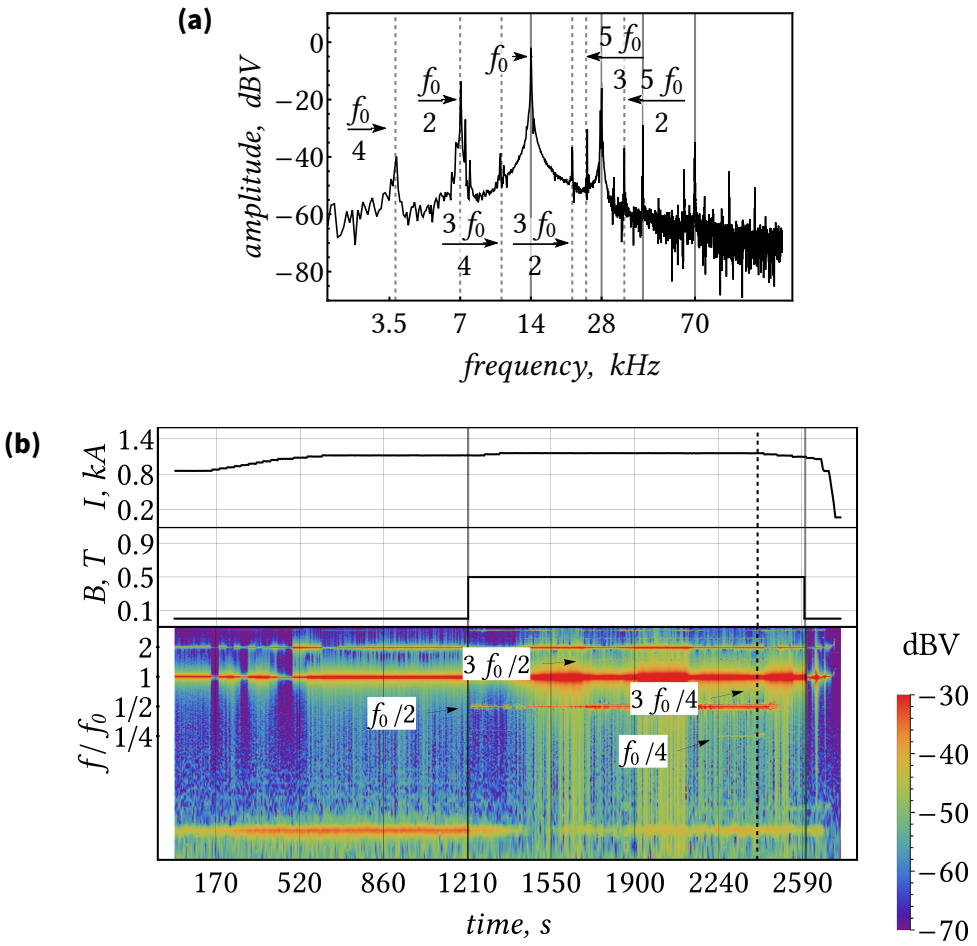

Figure 5.3.: A representative example of a power spectrum at $t = 2400$ seconds (a) and a representative example of cavitation signal (bottom) depending on the applied coil current I (above the spectrum) and the applied magnetic field B during the whole experiment (b). Power spectrum in (a) corresponds to the dashed line in (b).

The combined acoustic spectrum gives a better overview of the whole process in a single image and will be explained in a greater detail here. The steady magnetic field is turned on at 1200 s and turned off at 2600 s – the interval between the solid lines in Figure 5.3 (b). It is also graphically represented above the spectrum. The magnetic field is kept constant at the maximum value during this period, while the coil current is gradually increased to the maximum of 1.3 kA, kept constant and then decreased as shown in the graph at the top. The spectrum is given in voltage from the piezo element relative to 1

volt (dBV). A pronounced $f_0/2$ subharmonic appears immediately after applying the static magnetic field and stays almost until the field is turned off. A $3f_0/2$ ultraharmonic emerges at 1650 s, while a weaker $f_0/4$ subharmonic appears at 2200 s. Lastly, just before the $f_0/2$ subharmonic disappears, a weak $3f_0/4$ appears at around 2300 s.

5.5. Cavitation with a sonotrode and potential problems

The cavitation signal recording method is evaluated using a Hielscher UIP500 ultrasonic mixer with a nominal power of 500 W and 20 kHz processing frequency. The 15 mm large tip has maximum amplitude of 250 µm. It is difficult to estimate the oscillating pressure amplitude P_A since it depends on many factors. However, based on the measured properties of a different, but stronger ultrasound generator described elsewhere [78], the input oscillating pressure amplitude is, most likely, not larger than 50 kPa, i.e. it is comparable with the theoretical P_A obtained with the contactless approach.

Three liquids have been used for testing the recording of cavitation – water, silicon oil AK37 and GaInSn. The physical properties of the materials are given in Table 5.4. A piezo element is attached to a copper cylinder (further in text called *waveguide*) which is directly immersed in the liquid. The cavitation signal from this waveguide has been compared with a signal recorded with the shielding plate from the experimental set-up. A mock sample is attached to the shield and immersed in the liquid next to the waveguide. The testing set-up is shown in Figure 5.4.

Comparison between the cavitation signal obtained using the waveguide in the liquids can be seen in Figure 5.5. It can be observed that the signal strength is strongest for the silicon oil and weakest for GaInSn. The result is as expected, since the main limiting factor for bubble growth is surface tension. The activity of cavitation is marked with many different spectral lines. A high intensity broadband noise in the higher frequencies is visible as well. Additionally, multiple sub- and ultraharmonics, e.g. $f_0/3$, $f_0/2$, $4f_0/3$, together with higher order harmonics, e.g. $2f_0$, $3f_0$, are detectable.

Figure 5.6 shows a comparison of the recorded signals between the waveguide and the experimental set-up with the highest sonotrode amplitude in the silicon oil. The characteristic properties of the signal differ a lot. One important missing detail in the shield signal is the higher frequency broadband noise which originates from collapse induced

Table 5.4.: The physical properties of used liquids for cavitation signal recording.

Liquid[a]	WACKER AK 35 Silicone oil [113]	H_2O	GaInSn [92]
Density, ρ g cm^{-3}	0.96	0.99	6.330
Dynamic viscosity, η mPa s	35	0.89	2.1
Surface tension, γ mN m^{-1}	21	≈ 60	585

[a] At around 25 °C.

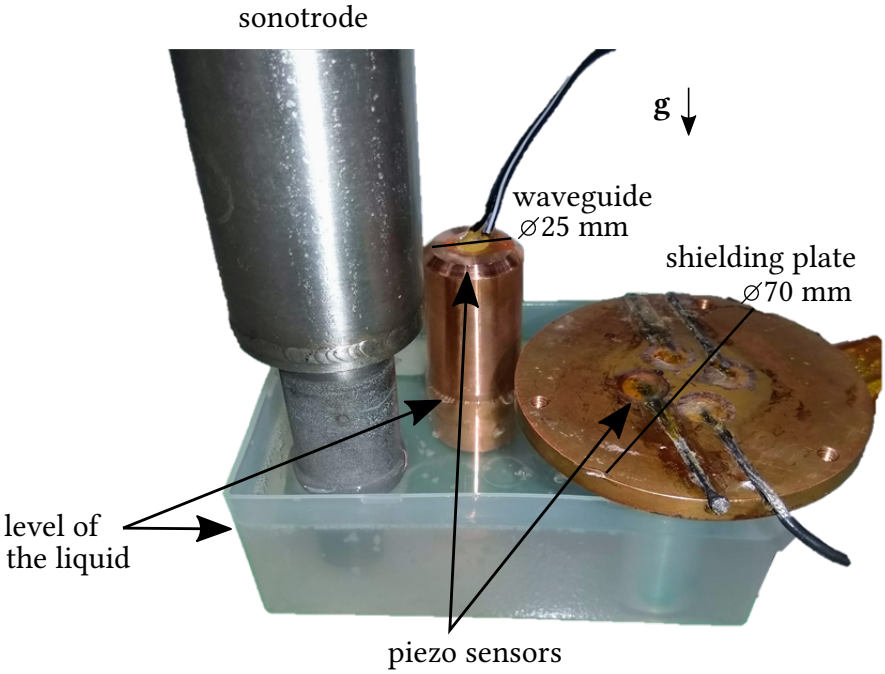

Figure 5.4.: Cavitation signal measurement set-up with the sonotrode on the left, the copper *waveguide* in the middle and the *shielding* plate from the experimental set-up with an aluminium mock sample immersed in the liquid on the right. Piezo elements are fixed at the top.

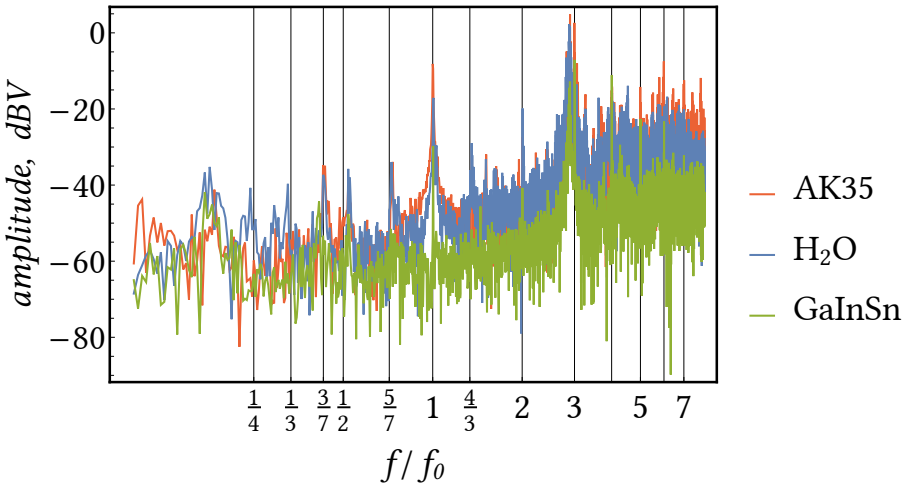

Figure 5.5.: Cavitation signal in three different liquids – silicon oil AK37, water and GaInSn, measured with the waveguide. The strongest cavitation is recorded in oil, the weakest in liquid metal. The surface tension plays the main role, especially for smaller bubbles, which is in accordance with the bubble oscillation theory.

shockwaves, cavitation activity of very small bubbles and instabilities in general. As the recorded spectra with the shield do not provide any useful information about cavitation activity after $3f_0$, it will be discarded in further analysis. Yet, the other important signs – sub- and ultraharmonics, e.g. $f_0/2$ – are clearly visible and broader, and, furthermore, have much larger amplitude compared with the waveguide. Therefore, to determine the cavitation onset and strength, only these harmonics, i.e. nf_0/m, $n = 1, 2, 3$ and $m = 2, 3, 4$, will be used. The presented comparison gives sufficient ground to use the proposed piezo element arrangement for detecting cavitation in the real experiments.

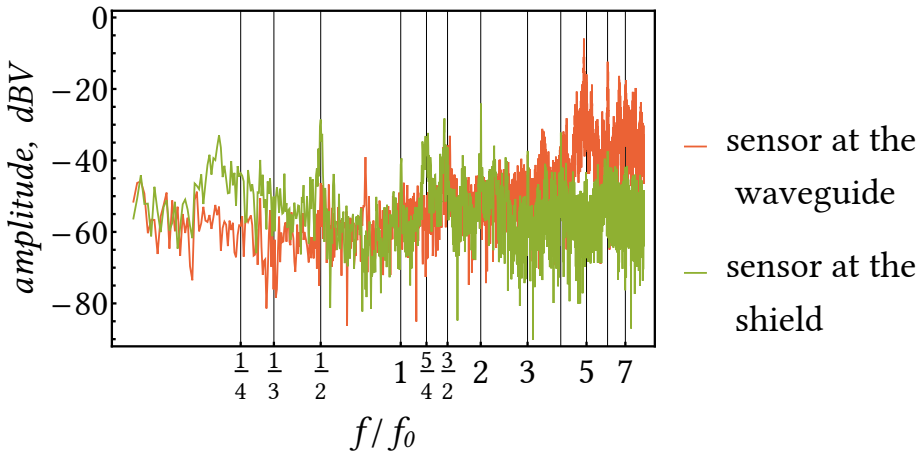

Figure 5.6.: Comparison of cavitation signal measured at the same time with the waveguide and the shield in silicon oil. Vibration amplitude of sonotrode is 250 µm. Spectra recorded with the experimental set-up shown in Figure 5.4.

5.6. Cavitation soldering – signal and effects

Ultrasonic soldering is a known method to connect metal pieces without any fluxing agent. The principle is based on the disruption of the oxide layer that naturally covers any liquid metal surface [114]. As a proof of concept, an experiment employing this principle using the contactless cavitation method, has been performed. A small, pure tin cylinder is placed in-between two copper supports which are well cooled and cannot melt in the applied AC field. When the tin is molten, steady magnetic field of either 0.8 T in the low field set-up or 1 T in the high field set-up is applied to the sample. The difference between simple melting and melting with cavitation can be directly observed and compared after the experiment.

The initial conditions of copper supports and tin can be seen in Figure 5.7 (a) while (b) and (c) shows the samples after melting in low field experiment. Sample produced in high field experiment is shown in (d). Result without applying the steady field, i.e. without cavitation treatment, can be seen in (b). The tin is completely molten and drops downwards along the copper cylinder, however, all metal pieces are completely separable. Applying cavitation drastically changes the outcome - tin and copper parts are soldered together, as illustrated in (c) and (d).

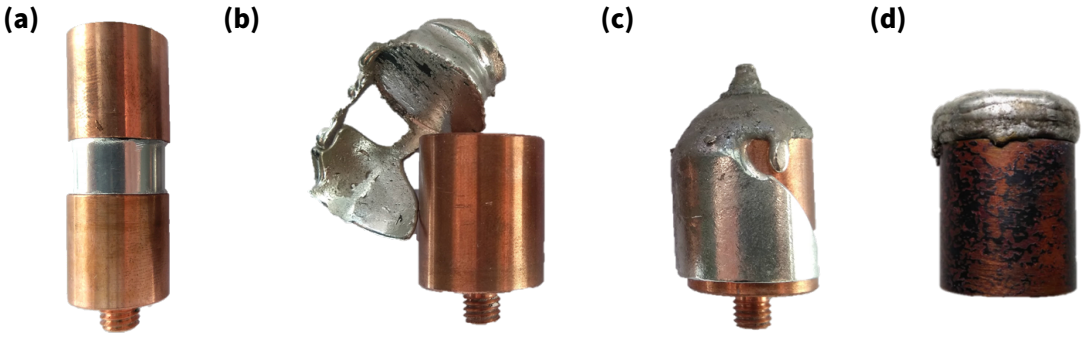

Figure 5.7.: Soldering of copper and tin. Initial sample in (a), processing without applied DC magnetic field (b) and processing with applied 0.8 T steady magnetic field, i.e. with cavitation treatment, in low field set-up in (c). Soldering of copper and tin in the superconducting magnet set-up with a 1 T strong field shown in (d).

The corresponding cavitation spectrum obtained during processing of sample (c) can be seen in Figure 5.8. The AC field is maximum and kept constant from 1000 to 1300 seconds at 1400 A, 0.8 T is applied from 600 to 1350 seconds. It must be noted that the current is gradually increased, but only the maximum is marked in the graph. It is possible to observe strong $f_0/3$ and $2f_0/3$ peaks at the start of the processing, yet, they become weaker after the sudden, unexplainable drop in signal from 790 to 800 seconds. In the higher frequency range the $5f_0/3$ peak stands out. It is also possible to see a broad, but weak $f_0/2$ peak. While also missing during the previously mentioned gap, it grows stronger during the processing as can be seen in the 1180 second inset. This direct correlation between an observable result of cavitation (soldering) and the expected cavitation signal ($f_0/2$, $f_0/3$) gives proof that the cavitation can be generated in a contactless way and recorded.

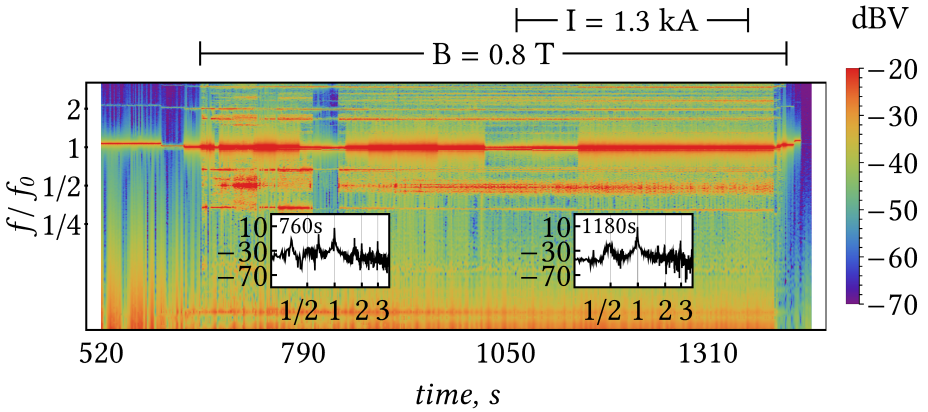

Figure 5.8.: Cavitation spectrum of copper-tin soldering experiment, obtained during the processing of sample (c) in Figure 5.7. Insets show the signal at 760 and 1180 seconds. At the start strong $f_0/3$ and $2f_0/3$ peaks together with a slightly weaker bump at $f_0/2$ can be seen. During processing, at 1180 seconds, both peaks have become weaker, yet, the broad $f_0/2$ has become more pronounced. Steady magnetic field is applied from 650 to 1410 seconds, maximum current is applied from 1060 to 1360 seconds.

5.7. Cavitation with pure metals in lowest magnetic field (0.5 T)

Some representative spectra from both, pure metal processing and processing of composites, are presented in the following sections. Here the notion of *composite* metals stands for admixture of particles in contrast to the *pure* metal case where the sample is processed without addition of the reinforcement phase. The selection of detailed results is based on displaying the successful experiments which show cavitation in different materials. It must be noted that not every melting with superimposed steady magnetic field yielded recordable cavitation.

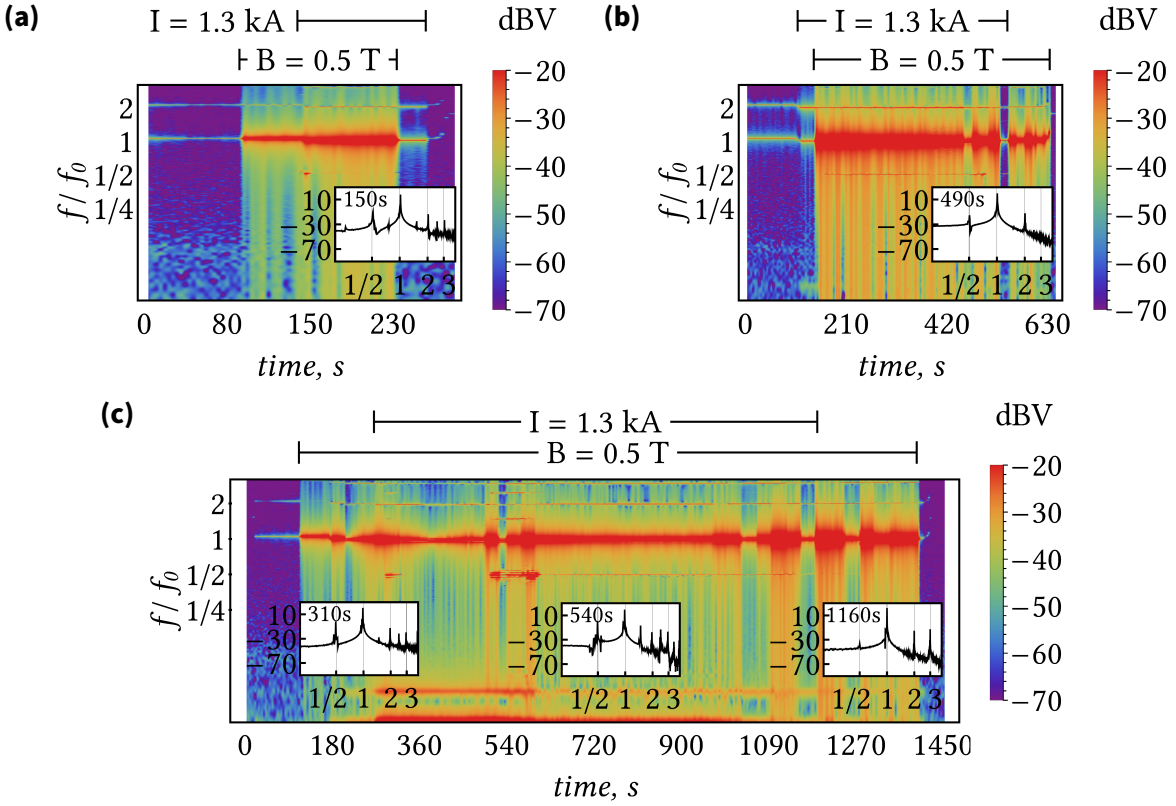

Figure 5.9.: Recorded cavitation phenomenon with pure metals: (a) tin, (b) aluminum, (c) stainless steel. Experiments performed in the 0.5 T magnet. The spectra show the characteristic $f_0/2$ peak in all cases, however, with varying strengths.

The spectra in Figure 5.9 show recorded cavitation signal in tin (a), aluminum (b) and steel (c), all produced in 0.5 T. Using this low field it is possible, according to equation (3.9), to introduce 52 kPa large pressure oscillations in the liquid metal. From the obtained spectra it can be concluded that such P_A is sufficient to initiate cavitation. However, it can also be seen that the recorded signal is weak and unstable.

In the case of tin, the $f_0/2$ peak is strongest at the start as shown in the inset at 150 seconds and then diminishes. On the other hand, in aluminum, the half frequency is visible for the whole experiment, but is less pronounced than in the case of tin. Lastly, in the steel

sample the $f_0/2$ peak is stable, but for most of the experiment rather weak (1160 second inset) and close to the background noise level. A much stronger response is observable at the start of the processing (at 310 and 540 seconds).

These results with the pure metals do not fully agree with the phenomenological description of cavitation presented before. Based on the material properties, tin and aluminum should have stronger bubble response (lower viscosity, lowest density in case of Al) and therefore stronger cavitation. Yet, all the presented examples are similar, with steel having the strongest signal ($f_0/2$ around -1 dBV compared to Sn maxima at -9 dBV and Al maxima at -15 dBV) for short periods. This shows the large uncertainty regarding cavitation onset as many factors play a role. In the case of steel it can be assumed that there is a higher amount of nuclei inside which permits easier initiation of cavitation.

5.8. Cavitation with self-made tablets in lowest magnetic field (0.5 T)

The examples presented in further sections are from experiments where melting is done together with particles. As explained in the raw materials section, the particles are admixed with the matrix material and then compressed. Pressing has been done either with a simple press in HZDR or in IFAM with and without SPS.

The first set of initial tablets are self-made, and have been melted in the 0.5 T magnet. During these experiments, it has been observed that the cavitation can become more pronounced with an increased ambient pressure, which, however, is counter-intuitive compared to formulas presented in section 3.3. From the Rayleigh-Plesset equation (3.43) it follows that the pressure amplitude must be larger than the ambient pressure for a part of the cycle to create a tension in the liquid. In other words, the cavitation onset is delayed by the ambient pressure and increasing the pressure in the melting cell should damp the cavitation phenomenon. Yet, in some instances an increase/change of the signal strength has been recorded.

Such response to increasing pressure, however, cannot be predicted and is not consistent in every experiment where the pressure change has been applied. The explanation for this response can only be speculated. One possibility can be related to degassing – as the cavitation is used to remove dissolved gas, the amount of cavities is reduced over time if the processing is done in vacuum. On the other hand, processing in an increased Ar atmosphere would allow some gas to diffuse inside the melt which might facilitate the bubble growth.

An example is shown in Figure 5.10 where stainless steel is processed together with 5 µm large CeO_2 particles. After turning on the steady magnetic field at 1200 seconds, the spectrum slightly broadens and a weak $f_0/2$ appears. An increase of Ar pressure, at the start, does not change the signal, however, at 400 mbar the $f_0/2$ peak disappears. Further increase of the pressure to 600 mbar brings a sudden broadening at the low frequencies as well as widening of $f_0/2$, as visible in the 1790 seconds inset. The low frequency signal may correspond to pulsations and cavitation of relatively large bubbles. Lowering and subsequent increase of the pressure level again changes the spectrum, yet, the previous

signal is not obtained. The second increase dampens the $f_0/2$ that appears at 2100 seconds, and cavitation signal is not obtained any more.

While this response to increased pressure is difficult to explain, it does give a reason to assume that the recorded cavitation signal truly arises from the effect taking place in the melt and not from other sources.

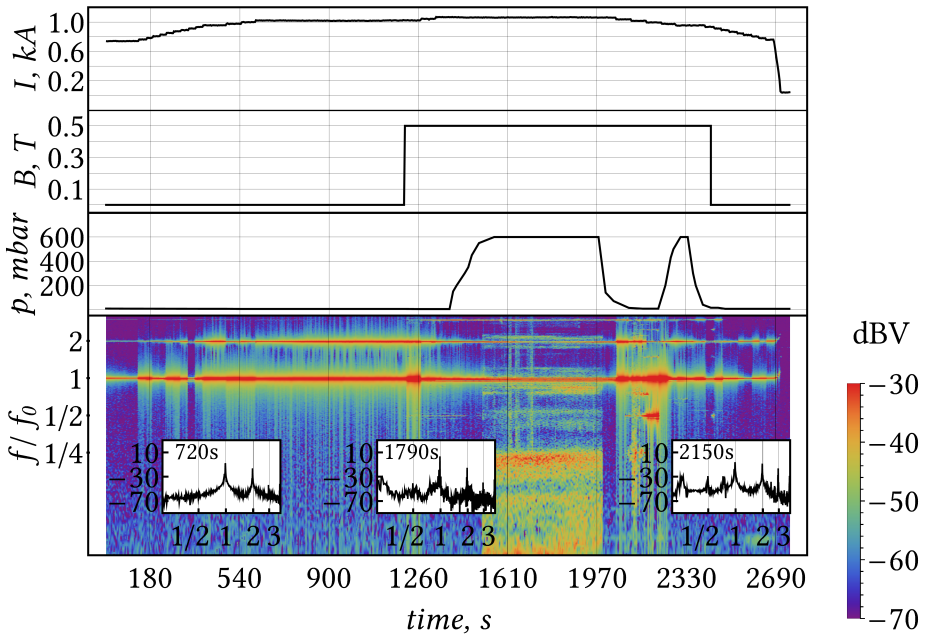

Figure 5.10.: An example of a power spectrum with a changing cavitation signal response to varied pressure in the melting chamber. Insets at 720, 1790 and 2150 seconds show the signal without steady magnetic field, with 0.5 T and 600 mbar in the melting chamber, and with 0.5 T and vacuum in the melting chamber, respectively. Steel processed with 5 µm large CeO_2 particles.

5.9. Cavitation with sintered and non-sintered tablets in low magnetic field (0.8 T)

Cavitation phenomenon with sintered and non-sintered initial tablets in iron and nickel are presented next. These samples do not represent the strongest recorded cavitation in iron, however, these are exemplary cases where cavitation is observed and can be compared with the same reinforcement (TiC) in iron and nickel, with and without SPS. The presented experiments have been conducted in the 0.8 T magnet.

Spectrum from processing of iron with 0.8 µm large TiC particles (initial sample created by SPS) can be seen in Figure 5.11. Steady magnetic field of 0.8 T is applied from 920 to 2910 seconds. Current has reached maximum 1300 A from 1640 to 2760 seconds. The first inset shows the recorded signal without cavitation treatment when the sample is already liquid. When the magnet is turned on, nothing changes in the low frequency range while

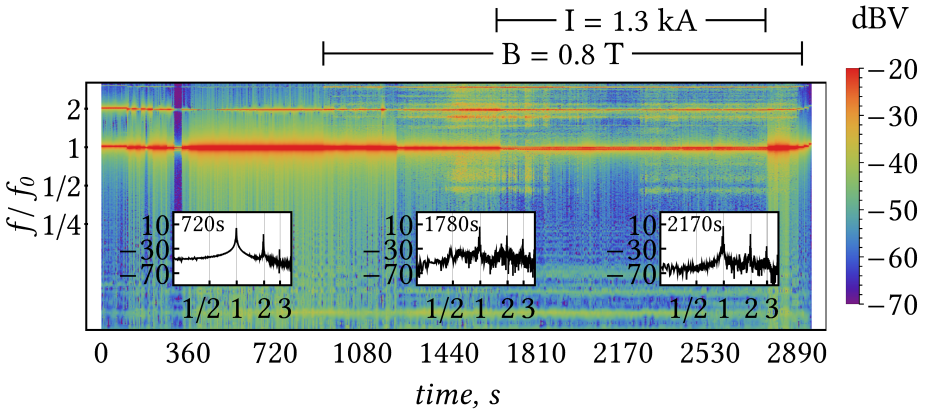

Figure 5.11.: Cavitation spectrum from processing of pure iron with 0.8 µm TiC. Initial sample is produced with SPS. The inset at 720 seconds shows the spectrum without the steady magnetic field. 0.8 T magnetic field is applied from 920 to 2910 seconds, maximum current is applied from 1640 to 2760 seconds. A slight broadening of spectrum from 1440 to 1810 seconds is observable in the inset at 1780 seconds and then again from 2200 seconds. During the gap there are no signs of cavitation as shown in the inset at 2170 seconds. The broad low frequency part includes a wide $f_0/2$ peak.

some weak peaks appear at higher harmonics. Around 1440 seconds there is a change in the signal as a sudden broadening of spectrum in the low frequency range can be observed. The inset at 1780 seconds, during maximum processing conditions, possibly reveals frail, but wide $f_0/2$. This broadening of the signal is not continuous, as quiet gaps can be seen, e.g. in the 2170 seconds inset.

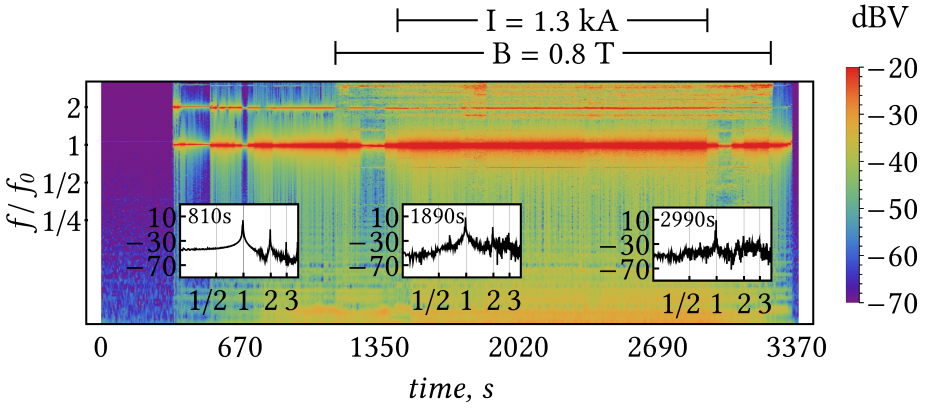

Figure 5.12.: Cavitation spectrum from processing of pure iron with 0.8 µm TiC. Initial sample is produced without SPS. The inset at 810 seconds shows the spectrum without the steady magnetic field. 0.8 T magnetic field is applied from 1140 to 3240 seconds, maximum current is applied from 1440 to 2940 seconds. Inset at 1890 seconds shows a strong $2f_0/3$ peak, while near the end of the processing it has become weaker. Possibly, a dim $f_0/2$ could be existing within the background noise, as can be seen in the inset at 2990 seconds.

Spectrum from processing of iron with an initial sample produced without SPS can be seen in Figure 5.12. Steady magnetic field of 0.8 T is applied from 1140 to 3240 seconds. Current is set to maximum 1300 A from 1440 to 2940 seconds. Compared with the previous experiment only a stable $2f_0/3$ peak can be observed throughout the experiment. At around 2990 seconds the low frequency noise has increased, and, possibly, a dim $f_0/2$ arises which may indicate cavitation activity.

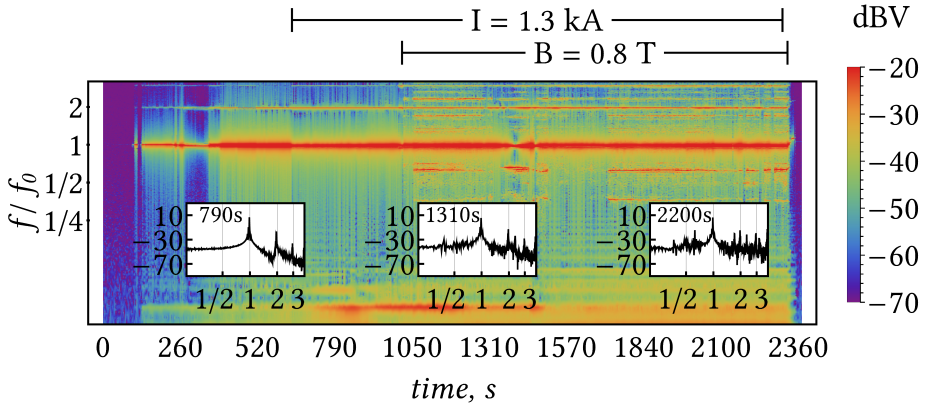

Figure 5.13.: Cavitation spectrum from processing of pure nickel with 0.8 µm TiC. Initial sample is produced without SPS. The inset at 790 seconds shows the spectrum without the steady magnetic field. 0.8 T magnetic field is applied from 1010 to 2320 seconds, maximum current is applied from 640 to 2300 seconds. Different strong, but inconsistent peaks are observable. During the weakening phase at 1310 seconds only $f_0/3$ remains strong. At 2200 seconds also $2f_0/3$ appears, and in-between a slightly weaker $f_0/2$ emerges.

Spectrum from processing of nickel with a TiC tablet produced without sintering can be seen in Figure 5.13. Steady magnetic field of 0.8 T is applied from 1010 to 2320 seconds. Current is maximum at 1300 A from 640 to 2300 seconds. The spectrum has a couple of distinct peaks, namely, $f_0/3$ and $2f_0/3$ in the low frequency range. Similar to the previous experiments, the signal also is inconsistent. The $f_0/2$ is visible, but for most part it has an amplitude close to the level of noise as can be seen in the 1310 second inset. It only appears more prominently towards the end of the experiment, at around 2200 seconds. Nevertheless, it shows that cavitation is also achievable in nickel.

As the only available data is the recorded sound emitted by many cavitating bubbles, it does not bear a direct translation to cavitation impact or strength. As such, any description is limited to comparison of the emitted power level between sets of experiments. In the presented cases above, the noise level without the steady magnetic field is around −45 dB V. Processing of iron with the initial sample made with SPS (Figure 5.11) has the shortest lived cavitation activity with a $f_0/2$ peak having maximum at −30 dB V, while exhibiting a sporadic response. Melting when the initial sample is produced without SPS (Figure 5.12) creates a relatively stable $2f_0/3$ peak for the whole duration of the experiment. Yet, a decrease from −20 dB V at the beginning to −25 dB V at the end can be observed. Lastly, the nickel sample, which is created without SPS (Figure 5.13), has the highest emitted power which corresponds to comparably highest cavitation intensity in the melt. At least

three distinct peaks can be recognized: $f_0/3$ at −30 dB V, $f_0/2$ at −21 dB V and $2f_0/3$ at −13 dB V. While being inconsistent, the overall response is the strongest compared to the others.

When comparing different materials with the same reinforcement phase (TiC), it is possible to conclude that production without sintering is more beneficial to initiate the cavitation. The manufacturing without sintering leads to a higher amount of impurities as the processing temperatures are lower and production byproducts do not react as the sample is not liquified. Additionally, there is large amount of cavities with entrapped gas inside the tablet which is released inside the melt during melting. In other words, without SPS, the samples have a larger amount of cavitation nuclei besides the added ceramic reinforcement phase. However, this is also one of the few observed cavitation instances in nickel, while in iron it is reachable in most cases. It again shows the high level of uncertainty and randomness for the initiation of cavitation.

5.10. Cavitation in the superconducting magnet

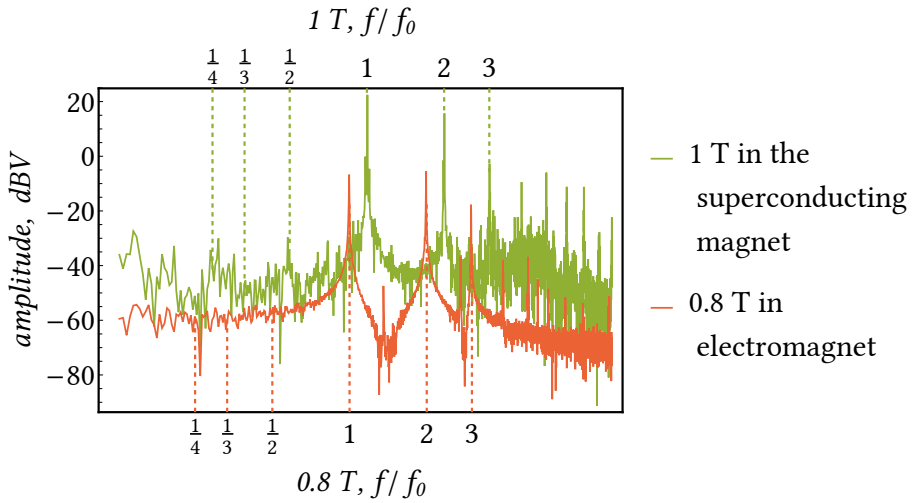

Figure 5.14.: Comparison of signals created by superimposing alternating and steady magnetic field on low (trial done in 0.8 T, red line) and high (trial done in 1 T, green line) field set-ups. Top of the graph marks frequencies for superconducing magnet, while bottom for the electromagnet. A clear difference can be observed – the low field set-up signal does not have any significant peaks while the superconducting magnet signal already shows all relevant sub-harmonics, i.e. $f_0/2$, $f_0/3$, $f_0/4$, even when the set-up is empty.

As the theoretical calculations showed that the available field strengths are on the borderline to achieve a strong cavitation regime, complementing experiments have been conducted in a superconducing magnet in HLD. This magnet allows field strengths of up to 19 T in a 150 mm bore. Working with such device demands higher precautions, therefore, the project and construction of the set-up is much more complex compared

with that used in low fields. Since the magnet is 2 meters deep and is accessible only from the top, the melting chamber is not reachable during the experiments. Furthermore, it is not possible to assemble or adjust the set-up inside the bore. Therefore, the experiment is designed in a way, that the melting chamber is built around the coil, and then the coil can be immersed in the magnet together with it. The scheme of the whole assembled set-up has been presented in Figure 5.2. Such design, however, also brought unforeseen problems.

From the experiments in the low magnetic fields it is known that the coil vibrates and emits high frequency signals which interferes with the cavitation recordings, i.e. the coil vibrations are a source for higher order harmonics (nf_0, $n = 2, 3...$). Furthermore, the coil cannot touch the quartz glass which encloses the experiment, as that generates additional sub- and ultra-harmonics. While in the high field experiment the coil is centered with respect to the system so it does not touch the set-up, some mechanical coupling is unavoidable for the assembling and inserting into the magnet. Yet, for meaningful cavitation measurements, a complete decoupling of both pieces is necessary.

Figure 5.14 shows the difference of noise levels when the maximum current is applied and superimposed with the steady magnetic field in low magnetic field set-up (red, 0.8 T) and high magnetic field set-up (green, 1 T). The recorded signals are with empty set-ups, i.e. there is no workpiece inside. The low magnetic field set-up, which is completely decoupled from the induction coil, has some background noise, yet, no distinctive subharmonics are visible. On the other hand, the superconducting magnet experiment shows much higher noise. More importantly, strong peaks appear at the locations where the cavitation signal is to be expected, i.e. subharmonics of the driving frequency. This highly complicates the analysis of the recorded signal, and, for now, no real cavitation recordings for the high field case can be presented simply because of the large uncertainty of what exactly has been recorded in these experiments. Since the cavitation signal from the piezo elements is not reliable, to determine if cavitation occurs in the superconducting magnet set-up, a test of tin-copper soldering has been performed. Successful soldering can be observed and was demonstrated in Figure 5.7 (d).

5.11. Synopsis about recording of the cavitation

The concept of contactless production of cavitation has been proven to work in various metals. It has been successfully applied to tin, aluminium, steel, iron and nickel. For high melting point metals, which are the main focus of the work, cavitation is the strongest in steel, followed by iron and nickel. Yet, the response is not fully consistent, and cannot be predicted, as the same metal with the same initial conditions (as much as it is possible to control them) initiates cavitation in one case, but it may be absent in another.

The recording principle of attaching the piezo elements outside of the melting chamber can be used to determine the cavitation onset. Furthermore, the proposed arrangement on the set-up enhances the low frequency signal allowing to more clearly recognize different harmonics related to the cavitation activity. Still some uncertainty about the cavitation form remains as the high frequency range is mechanically filtered out.

The strength of cavitation indeed depends on the purity of the material. The production method of the initial sample plays a significant role – more impure starting conditions

produce more intense cavitation. Additionally, a significant uncertainty exists regarding the influence of other processing factors. An example of sudden change of the spectrum and increase of low frequency noise by increasing the ambient pressure in the melting chamber has been demonstrated. Such effect is counterintuitive to cavitation description where external pressure acts against the cavity growth. A more in-depth investigation is needed to understand how other parameters influence the cavitation onset as well as its intensity.

In general, even the lowest P_A created by the 0.5 T magnet is sufficient to induce cavitation in different liquid metals, including the heavy elements. Yet, the recorded sound spectra often consist of weak subharmonics, that suggests a weak bubble response to the applied oscillating pressure field. This information about the minimum B_z required can be used to improve the processing conditions as the smallest cavitating bubble size can be estimated. From here, its resonance frequency can be obtained and then the processing frequency may be adjusted accordingly.

6. The microstructure analysis of the samples produced with a contactless cavitation treatment

In the following sections the results related to the dispersion of microparticles in high melting point metals are presented. Firstly, the basic introduction of the applied metallographic concepts is given, followed by showcasing selected micrographs. The chosen selection provides an overview and only representative samples, exemplarily demonstrating the main tendencies, will be shown. As the main focus of the work is to disperse ceramic particles inside high melting point metals, and since it is *a priori* in general unknown if a good dispersion can be obtained for a specific combination of metal and particles, many different reinforcements have been tested to identify the most prospective ones.

6.1. Analysis of the samples

The samples produced with the contactless cavitation treatment are on average 30 mm long with a diameter of 20 mm. As the tablet usually has a slightly lower density and there is empty space between the tablet and the top support, the end shape of the sample usually resembles to that of an hourglass. An embedded and polished sample is depicted in Figure 6.1. The samples are cut in half and the molten region is extracted from the whole sample using wire cutting. The specimen is then mounted using cold mounting resin and grinded and polished using subsequent finer abrasives. The grinding is started with a grit 80 and finished with a grit 2400 grinding paper. After removal of the waste, the specimen is polished with a diamond suspension of 6 µm, 3 µm and 1 µm. The markings in Figure 6.1 (*Top, Bottom, Right, Left, Middle*) correspond to the position on the sample and will be used to describe the location in the sample later in micrographs. *Top* and *Bottom* denote the approximate solid-liquid interface after the solidification – the boundary after which no particles can be found. *Left* and *Right* denote the edges of the free surface of the sample. If the particles are rejected by the matrix and pushed outwards during the solidification then an agglomeration layer is formed on these surfaces. *Middle* typically indicates a representative section of the whole bulk of the matrix, i.e. a micrograph from the middle has typical characteristics of all the volume.

Incident light microscopy is the method of choice for metallographic study – the specimen is illuminated from above trough an objective and then, depending on the employed technique (brightfield, darkfield, differential interference contrast, polarization), the sample can be examined. Leica DM6000 M optical microscope with a possible magnification of 1000 is used for the metallographic study. The image analysis and measurements are

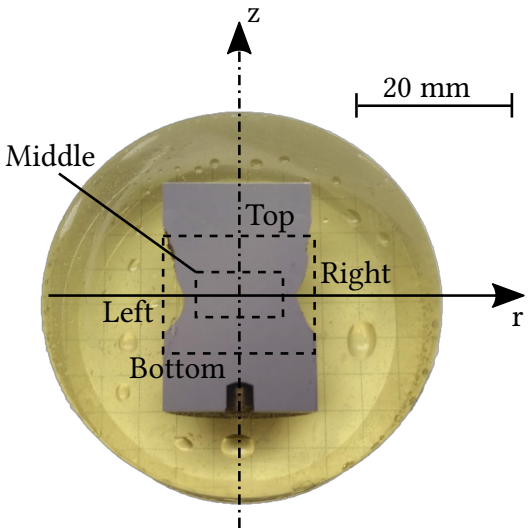

Figure 6.1.: A picture of a polished sample. *Top* and *Bottom* denote the approximate solid-liquid interface after the solidification, while *Left* and *Right* denote the edges of the free surface of the sample. *Middle* represents the bulk of the matrix.

performed with the image processing package Fiji. Since etching is not applied, the use of the microscope is limited to revealing information about particle dispersion and size, as well as porosity.

In scanning electron microscopy (SEM) an image is produced by a small focused beam of electrons scanning across the sample instead of using visible light. Main advantages over the light microscopy are much higher resolution (magnification of 10^6 times), depth of field and possibility of elemental analysis. Zeiss EVO 50 SEM is used with both, secondary electron and backscattered electron imaging capabilities. Bruker axs (advanced xray solutions) XFlash detector 4010 system is used to determine the elemental composition in the sample using energy-dispersive X-ray spectroscopy (EDX). SEM is operated with electron high tension of 15–20 kV, working distance of 15–20 mm, and a probe current of 0.5–1 nA. With these parameters the elemental composition is gathered from approximately 1 μm^3 surface volume in case of iron and steel.

6.2. Dispersion of oxides

Y_2O_3 is the most prospective reinforcement for producing ODS steels – an important material for fusion and fission reactors. The dispersion of the compound has been investigated in this work as well. 0.4 µm large Y_2O_3 particles have been melted using maximum current (1.3 kA) together with 1.4404 steel in the lowest DC field (0.5 T). Cavitation is applied for 24 minutes. Figure 6.2 (a) shows two large particle clusters (marked with solid arrows) inside the matrix. The nano-sized yttria create clearly visible agglomerates which then cluster in larger formations. While this, of course, is not a dispersed reinforcement phase, the particle clumps are in the matrix and not pushed to the edges, implying a weak

wettability (contact angle around 90°). As bad wetting behaviour (contact angle above 90°) of Y_2O_3 has been reported [115], such agglomeration inside the matrix, contrary to being pushed on the edges, suggests that even at low cavitation levels the dispersion can be improved by better wettability. In such case, the clustering can be reduced more if stronger cavitation is applied for a longer time. Yet, Y_2O_3 has not been researched further because of unavailable equipment, e.g. transmission electron microscopy, for nano-sized element examination.

Other oxides, i.e. CeO_2, TiO_2, Al_2O_3 and ZrO_2, have been successfully dispersed in steel to improve its mechanical properties by using spray casting as published in [36]. The reported success provides basis for testing these ceramics in steel using the proposed set-up as well. Nano-sized TiO_2 (0.02 µm) particle dispersion in 1.4404 steel has been investigated using processing in 0.5 T strong field for 23 minutes. The titania can be found as a thick (450 µm), agglomerated layer on the side edges of the matrix as can be seen in Figure 6.2 (b). The contact angle of the particles must be above 90° leading to such structuring. Similarly to Y_2O_3, individual particles cannot be observed microscopically, however, based on the visible amount excluded from the matrix, one can assume that there is no particle dispersion in the matrix. Therefore, TiO_2 can be considered to be impossible to use as a reinforcement in liquid state route.

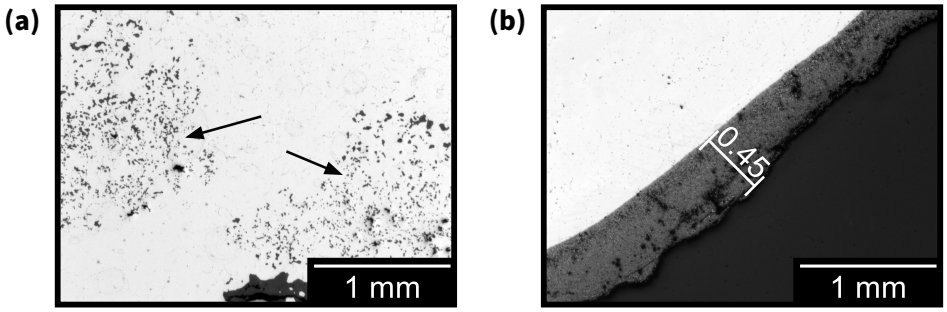

Figure 6.2.: Y_2O_3 particle (0.4 µm) clusters of large particle agglomerates marked with the solid arrows (a) in the middle of a steel matrix and TiO_2 particles (0.2 µm) expelled from the steel matrix creating a 450 µm thick shell around the sample (b). Micrograph of TiO_2 taken at the right side. Initial samples produced without SPS.

Nano-sized Al_2O_3 particles (0.02 µm) have been melted together with 1.4404 steel in a 0.5 T strong field for 17 minutes. The resulting matrix can be seen in Figure 6.3 (a). The inclusions are agglomerated and clustered in the middle of the matrix (black clumps in-between the solid arrows) creating a 1.5 mm wide belt through the sample. The agglomerated amount of particles corresponds to the amount inserted, therefore the rest of the matrix is considered empty. The same nanoparticles have also been processed in 3 T strong field for 30 minutes. Figure 6.3 (b) displays two larger clusters on the left edge of the sample (marked with the solid arrows). However, this is the only observable clustering of alumina in the whole sample. Comparing the agglomerated amount of (a) and (b) and taking into account that the initial inserted quantity is the same, the clustering with higher cavitation intensity is far lower. Consequently, larger amount of particles must be dispersed in the matrix. Yet, similarly as with previously described experiments, it is not possible to confirm this assumption because of the particle size.

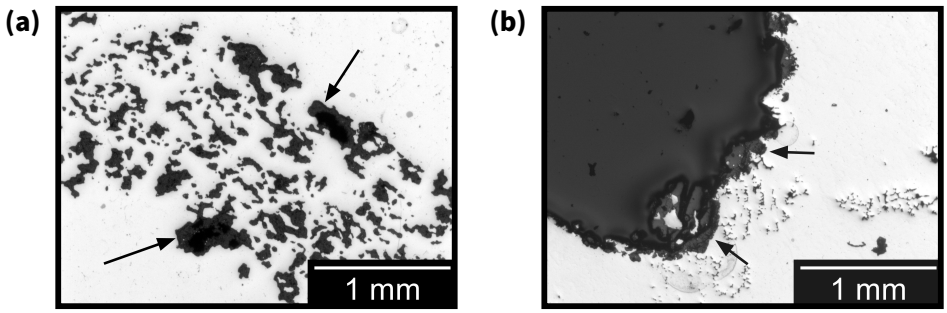

Figure 6.3.: Al_2O_3 particle agglomerations (black clumps in-between the solid arrows) in the middle of a steel matrix (a), processed in 0.5 T strong field for 17 minutes. Reduced agglomeration (black clusters at the left edge of the sample marked with arrows) when produced in 3 T strong field for 30 minutes (b). Initial samples produced with SPS.

Spherical Al_2O_3 particles (nominal size 0.8 µm) have been added to the iron. The resulting matrix of an experiment conducted in a 0.8 T strong field for 35 minutes is shown in Figure 6.4 (a) and (c). Some agglomerates can be found on the side edges, however, alumina is also well dispersed in the matrix – single particles can be found and are marked with solid arrows in (c). The size of these inclusions is larger than the nominal values inserted which can happen if the alumina has liquefied or dissolved and then precipitated in larger droplets. It is contradictory with published research ([102], [104]) where bad wetting (contact angle around 100-120°) is shown (conclusions about reactivity vary from non-reactive to weakly reacting system). Accordingly, it is the cavitation treatment that facilitates improved wetting behaviour. Applying 6 T strong field for 38 minutes still leaves considerable amount of agglomerates near the edges as shown in Figure 6.4 (b). Still, in the middle of the matrix the particulates have been reduced in size when compared to (c) as observable in (d), thus, following the expected behaviour – inclusion size is reduced with a more intense cavitation treatment.

The spherical alumina has also been added to nickel. Experimental results from melting in a 0.8 T strong magnet for 23 minutes are shown in Figure 6.5. Image (a) shows agglomeration of alumina on the right edge of the nickel matrix. Such clusters can be found on the both sides circumventing the sample. The enlarged dark field (DF) micrograph of this cluster (b) shows single particles. The size, similarly to alumina in an iron matrix, is larger than the initially inserted 0.8 µm. This implies a phase transformation taking place, i.e. the particles also react with nickel. While being clearly pushed out during the solidification, the wettability is better than with TiO_2 in steel shown in Figure 6.2 (b). Alumina particles, while being on the edge of the matrix, are separated by a layer of metal, thus, remaining single within the cluster. Different processing parameters, e.g. higher flow rate, could improve the dispersion.

Comparison of ZrO_2 (initial particle size 0.8 µm) dispersion in iron with small (0.8 T) (a,b,c) and large (5 T) (d) magnetic field can be seen in Figure 6.6. Melting is done for 35 and 40 minutes, respectively. The precipitates cluster in a thick layer at the top and bottom of the sample (bottom shown in (a), enlarged SEM image in (b)), yet, the wettability is good since the individual precipitates are separated by the matrix material. Furthermore, zirconia can also be found in the matrix (c), yet, it is obvious, that the particle size after

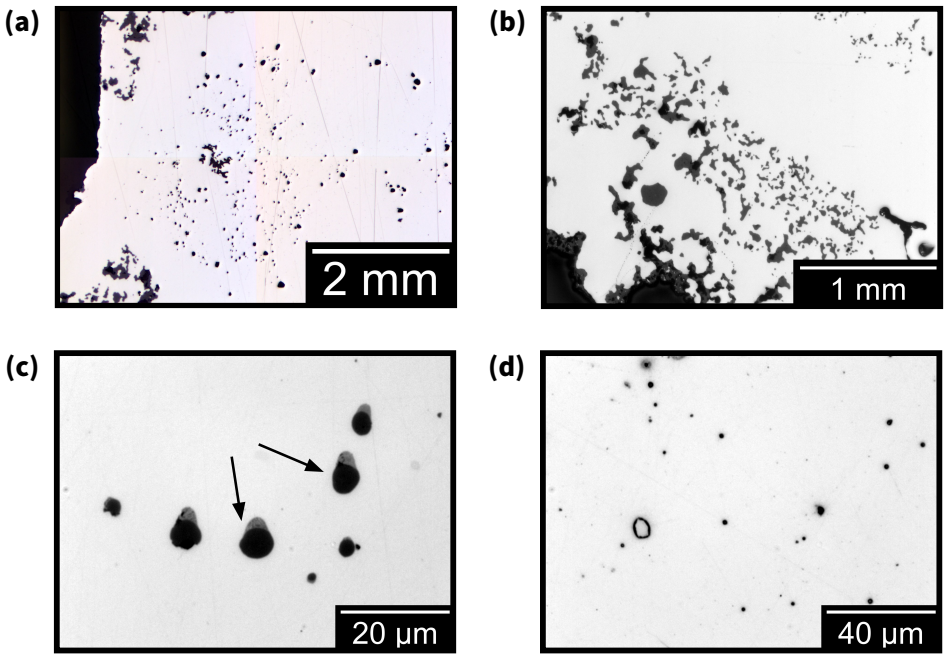

Figure 6.4.: Spherical Al_2O_3 particle (nominal size 0.8 µm) distribution in iron by applying 0.8 T for 35 minutes (a,c) and 6 T strong field for 38 minutes (b,d). Initial samples produced without SPS. Large particle clusters can be found on the edges in both cases (a,b). Single particles can be also found in the middle of the matrix – marked with solid arrows in (c) and the black dots in (d).

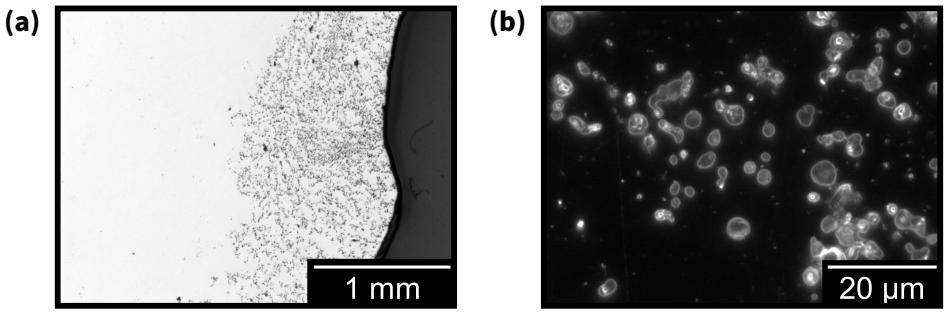

Figure 6.5.: Spherical Al_2O_3 particles (nominal size 0.8 µm) in nickel: particle agglomerates on the right edge of the sample (a) and dark field micrograph of single particles (b). Processing done in 0.8 T strong field for 23 minutes. Initial samples produced without SPS.

the experiment has increased from initial 0.8 µm to approximately 10 µm. The SEM image (b) reveals particulate change from the initially spherical to irregular droplet-like shapes. While it is not possible to give precise composition of these precipitates, the main element is Zr. The possible explanation for such change in the structure is melting of the particles – the ZrO_2 is not stable in the matrix. Dissolution or reaction of the elements in the current experiment, however, cannot be examined, yet, cavitation undoubtedly changes the thermodynamical stability. Therefore, interest lies if these precipitates can be reduced in size. Applying a stronger DC field (3 T) prevents the clustering at top and bottom (as in

(a)), thus, more particles are brought inside the matrix. The overall size of the precipitates (black dots in (d)) has been reduced as well.

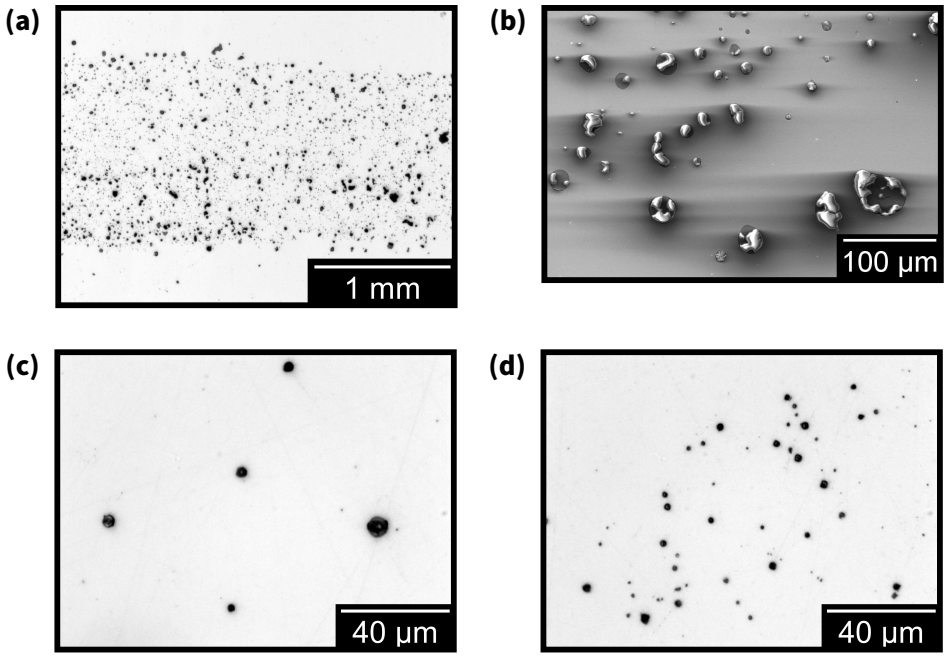

Figure 6.6.: ZrO_2 particles (nominal size 0.8 µm) in iron: overview of belt-like particle structure (a), enlarged SEM image of the belt (b) and view of the middle of the matrix (c) when sample processed with 0.8 T strong field for 35 minutes. Particle dispersion compared with processing in 3 T strong field for 40 minutes (d). Initial samples produced with SPS.

Dispersion of zirconia in 1.4404 steel has also been investigated. Figure 6.7 shows the resulting matrix produced in 0.8 T (a) for 120 minutes and 5 T (b) for 33 minutes. In both cases large agglomeration can be observed and the particles are pushed to the edges of the matrix, implying weaker wetting behaviour than in the case with iron. Therefore, it is concluded that the cavitation, irrespective of its intensity, does not improve dispersion of the zirconia in the steel grade used. Additionally, longer processing time does not affect the particle separation and/or homogenization of the precipitates, and it is clear that the ZrO_2 is completely rejected by the 1.4404 steel matrix.

CeO_2 particles (nominal size 5 µm) are added to iron and 1.4404 steel. Figure 6.8 shows ceria agglomeration in iron (a) (processed in 6 T strong field for 50 minutes) and 1.4404 steel (b) (processed in 5 T strong field for 35 minutes). The particles can be found on the edges of the matrix as well as agglomerated around inner cavities. While some small clusters are found inside the steel matrix as shown in the SEM/EDX micrographs (c,d), based on the the agglomerated amount, most of the particles are outside on the edges. It is understandable that CeO_2 is not a prospective compound to be used with the liquid state production route.

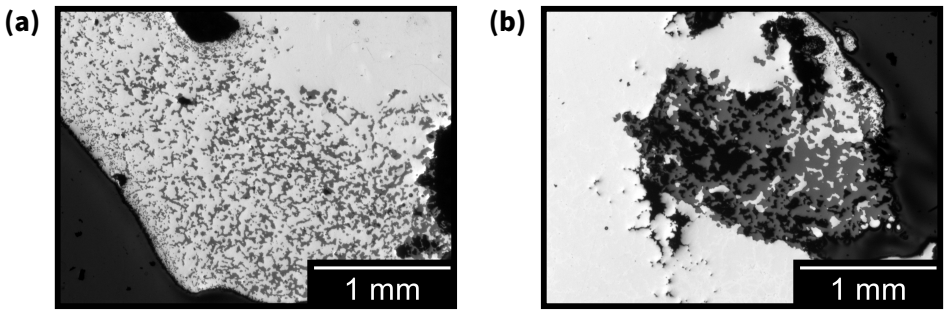

Figure 6.7.: ZrO_2 particles (nominal size 0.8 µm) in steel: processed in 0.8 T strong field for 120 minutes (a), processed in 5 T strong field for 33 minutes (b). Large agglomeration of the particles is observable at the edge of the sample in both cases. Initial samples produced with SPS.

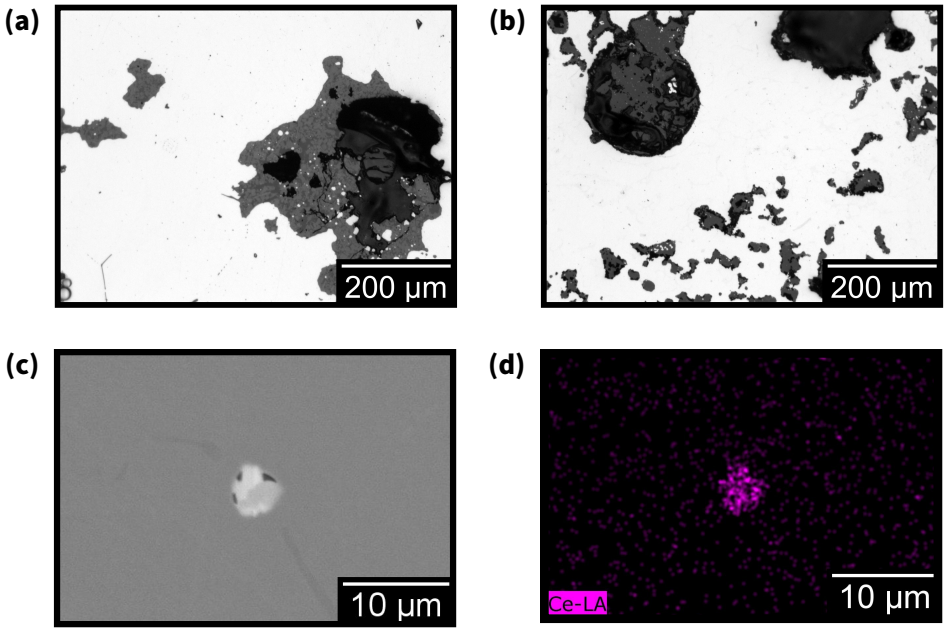

Figure 6.8.: CeO_2 particles (nominal size 5 µm) in iron processed in 6 T strong field for 50 minutes (a) and in steel processed in 5 T strong field for 35 minutes (b). Large agglomeration on the edges of inner cavities in the middle of the matrix observable in both cases. Images (c) and (d) show SEM/EDX analysis of a ceria particle inside a steel matrix. Initial samples produced with SPS.

6.3. Dispersion of carbides

TiC has been proposed as an excellent reinforcement in iron alloys because of its good wetting properties [105], [116]. Since good wettability is one of the key factors for successful particle dispersion, the possibility of using TiC as a reinforcement and improving its dispersion using cavitation treatment is examined.

Figure 6.9 shows TiC particle (nominal particle size 0.8 µm) dispersion in the middle of a 1.4404 steel matrix by applying 0.8 T (a) or 3 T (b) strong magnetic field. While in

both cases there are no large agglomerates the sample with lower magnetic field displays slightly larger, elongated precipitates (marked with empty arrows). In the case of 3 T the particles are more equisized, furthermore, smaller precipitates can be recognized (marked with empty arrows). The figures allow to compare the effect of processing time – the low field experiment has been conducted for 120 minutes while the high field experiment for 33 minutes. It is evident that higher magnetic field and, therefore, more intense cavitation, plays more important role than the treatment time.

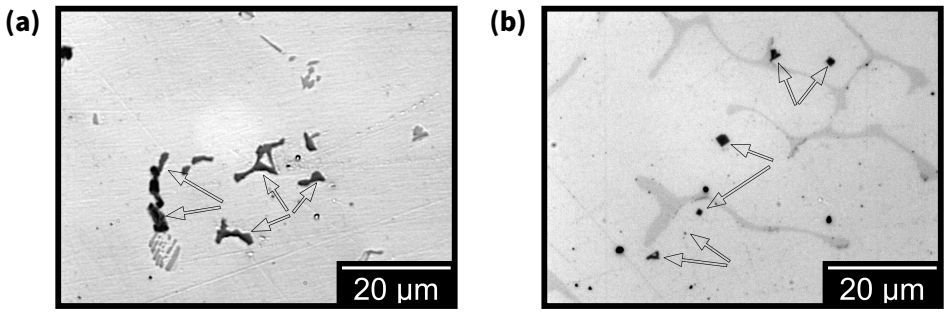

Figure 6.9.: TiC (initial particle size 0.8 µm) precipitates in the middle of a 1.4404 steel matrix (marked with empty arrows): processed in 0.8 T strong field for 120 minutes (a), processed in 3 T strong field for 33 minutes (b). Initial samples produced with SPS.

Comparison of TiC (initial particle size 0.8 µm) dispersion in the bulk of iron matrix with and without applied steady magnetic field is presented in Figure 6.10 (a) and (b), respectively. The particles (marked with empty arrows) without magnetic field have a larger size distribution, with largest particles in the range of 5 µm. On the other hand, melting in 3 T strong field with the cavitation treatment applied for 45 minutes yields smaller precipitates as can be seen in (b). Note that not all particles are marked with arrows, however, also not all of the black dots are particles in this case. In general TiC shows good dispersion in iron without cavitation as expected [105], yet, the cavitation treatment clearly reduces the size of the precipitates.

A clear difference between the initial and post-experiment particle size can be observed, both in steel and iron. The initial particle size of 0.8 µm does not remain such during the experiments – after the experiment the particles are considerably larger. The explanation for this behaviour, and also the good wetting properties, is the possible dissolving of the compound [105]. After dissolution the melt becomes supersaturated creating TiC precipitates during the processing. A further indication of such phenomenon is the morphology of the particles as the usual elongated shape can be recognized similar to other published works [117], [106]. While the exact mechanism is not clear in this experiment, the cavitation treatment can effectively reduce the size of TiC precipitates.

ZrC is one of the ultra high temperature ceramics (melting point around 3000 °C) and has very good wetting behaviour with iron and nickel [99], making it a good candidate for reinforcing. Around 1 µm large ZrC particles have been added to iron. Results from processing are shown in Figure 6.11: in 0.8 T in (a) and in 6 T in (b). Cavitation treatment has been applied for 35 minutes in the low field and 40 minutes in the high field. With a low magnetic field structures similar to Figure 6.6 (a) (the formation of precipitate layer at

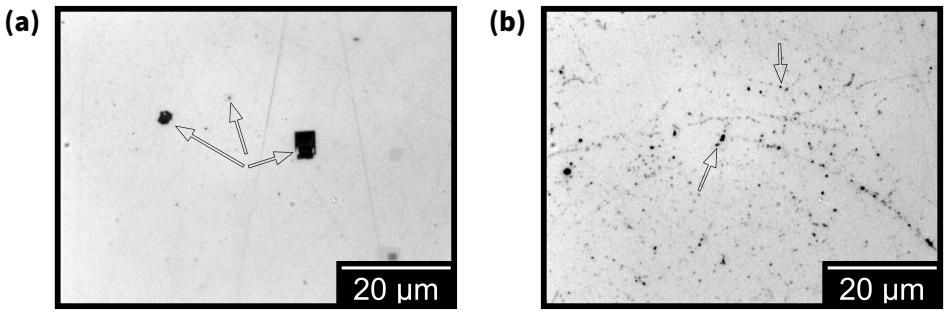

Figure 6.10.: Comparison of TiC (initial particle size 0.8 µm) dispersion in iron without DC field (a) and with 3 T strong magnetic field (b). Cavitation treatment applied for 45 minutes. TiC precipitates are marked with the empty arrows; most of the black dots in (b) are TiC. Initial samples produced with SPS.

the top and bottom of the matrix) have been found. The middle of the matrix has a large amount of spherical holes – presumably (based on the very low amount of particles found in the matrix) the particles are removed during the polishing phase (also known as particle pull-out). The holes tend to align along the grain boundaries. However, with an increased steady field, the droplet-like layer at the top and bottom part of the matrix is reduced as in the case of zirconia. Furthermore, the dark field image (b) reveals particles dispersed in a regular, rather equidistant manner giving an excellent distribution of the reinforcement phase.

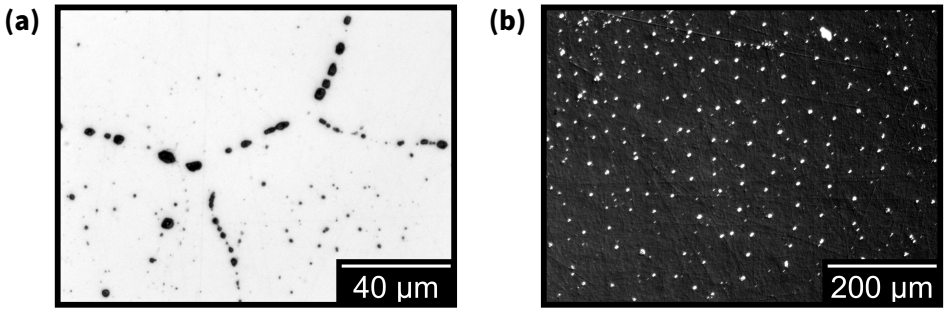

Figure 6.11.: ZrC particles (initial size 1 µm) processed with 0.8 T for 35 minutes in (a) and 6 T for 40 minutes in (b) (dark field image) in iron. The resulting matrix mostly consists of spherical holes that are left after the particles are removed during the polishing phase. Initial samples created without SPS.

The possibility to disperse the same TiC and ZrC in nickel has been investigated using 0.8 T strong field (cavitation treatment applied for 22 minutes). The results from these experiments are shown in Figure 6.12 (a) and (b). Small amount of single TiC precipitates can be found in the middle of the matrix. Yet, substantial part of the volume of the sample is dominated by large cavities (black structures in (a)) where TiC (marked with empty arrows) resides. It may be that these cavities are initially full with TiC droplets which are polished out during sample preparation. On the other hand, ZrC is clearly pushed out from the matrix as shown in (b) where the left side of the sample is shown. A 80 µm thick layer around the sample is created and no particles can be found inside the matrix. It is

clear that in the current configuration with the used processing parameters the carbides are not dispersible in the nickel matrix.

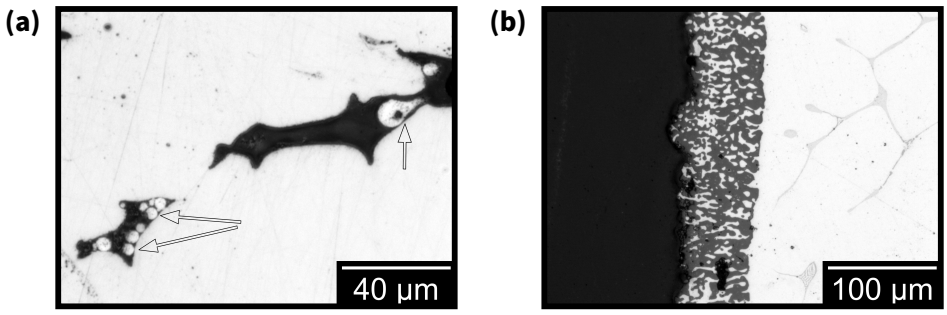

Figure 6.12.: TiC (initial particle size 0.8 µm) particulates (marked with empty arrows) in a cavity in nickel matrix in (a). ZrC particles (initial size 1 µm) pushed to the edge of the nickel matrix, creating a 80 µm thick layer around the sample in (b). ZrC micrograph taken at the left side. Both experiments conducted in 0.8 T magnetic field. Cavitation treatment applied for 22 minutes. Initial samples created without SPS.

6.4. Dispersion of nitrides

TiN shows good wettability and very low solubility in iron and steel [118]. Furthermore, TiN particles are widely used as grain refiners, and significantly increasing the concentration could lead to particles acting as a reinforcement phase. In-situ method for TiN reinforced iron production has already been successfully presented in [119]. This gives a solid reason to investigate cavitation assisted TiN dispersion in steel as well.

Figure 6.13 shows results of comparing TiN particle (initial size 0.8 µm) dispersion in 1.4404 steel using 0.5 T (a,c) or 3 T strong magnetic field (b,d). In the presented case the cavitation treatment is applied for 120 and 35 minutes, respectively. As expected, TiN shows excellent wettability even with a very weak cavitation treatment – the particles can be dispersed in the steel matrix. However, the particles tend to agglomerate in the case of lower magnetic field while much finer structures can be observed in the case with a higher applied cavitation intensity. Substantial differences exist between the particle phases as well. In low magnetic field processing particles can be found both in eutectic (empty arrows) and in solid (solid arrows) phases. Processing with a stronger cavitation the precipitates are purely in the eutectic phase (marked with empty arrows). The cavitation, with locally produced extreme conditions, supports the phase change. On the other hand, the agglomeration is also substantially reduced.

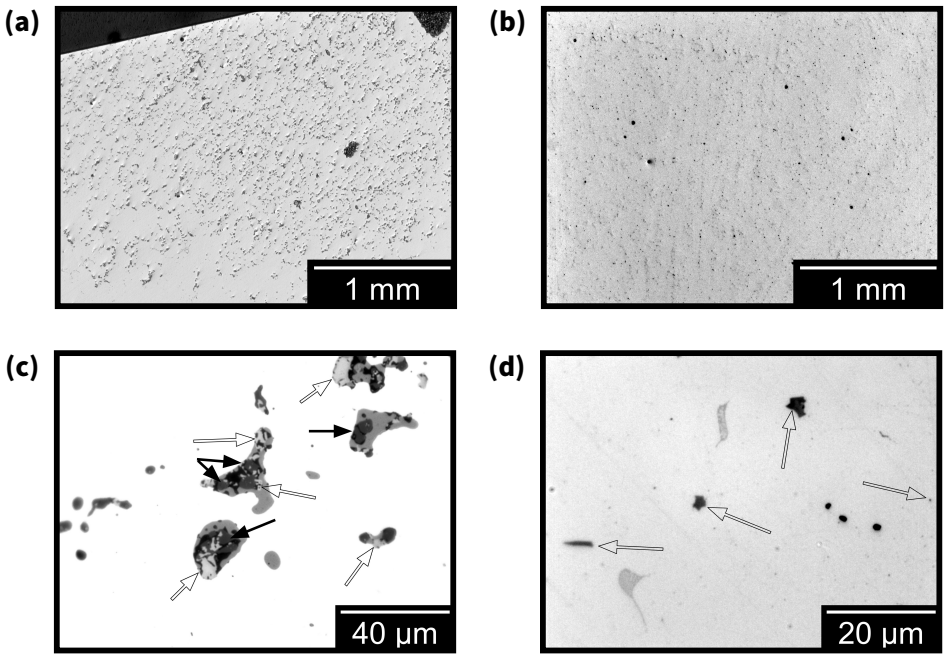

Figure 6.13.: Admixing of TiN particles (initial size 0.8 µm) in steel with 0.5 T magnetic field applied for 120 minutes in (a,c) and 3 T magnetic field applied for 33 minutes in (b,d). (a) and (b) show overview of the matrix while (c) and (d) show zoomed-in region in the middle. Empty arrows denote eutectic phase while solid arrows denote initially inserted particles. Initial samples produced with SPS.

6.5. Dispersion of borides

TiB_2 has been used to produce high modulus steels using in-situ production route [17]. Furthermore, dispersion of the compound has proven to be relatively good in iron and its alloys [107]. This gives justification to investigate the possibility of improving dispersion using the contactless cavitation treatment. Note that it has been shown that TiB_2 may dissolve and react with C inside the melt effectively creating TiC [107]. In such case also Fe_2B appears. Unfortunately, it is not possible to distinguish between B and C elements with the available characterization methods.

In Figure 6.14 comparison of TiB_2 particulate dispersion (nominal size 4 µm) in the middle of an iron matrix without (a,c) and with a 3 T large magnetic field (b,d) is shown. The melt is treated with cavitation for 45 minutes. Without cavitation treatment TiB_2 is stable inside the iron matrix for the duration of the experiment – solid, non-eutectic, but agglomerated particles can be seen in (c). A different result can be observed in a high magnetic field (b,d) – distinct grains appear (marked with black arrow). Furthermore, eutectic TiB_2 can be found in the matrix (marked with empty arrow), however, the amount of the eutectic particles is relatively low and not comparable with the inserted amount. The missing Ti- amount can be explained assuming a reaction happening between iron and TiB_2 creating Fe_2B (grains) and TiC (particles). Most likely cavitation facilitates this reaction either by increased temperature or by improving wetting.

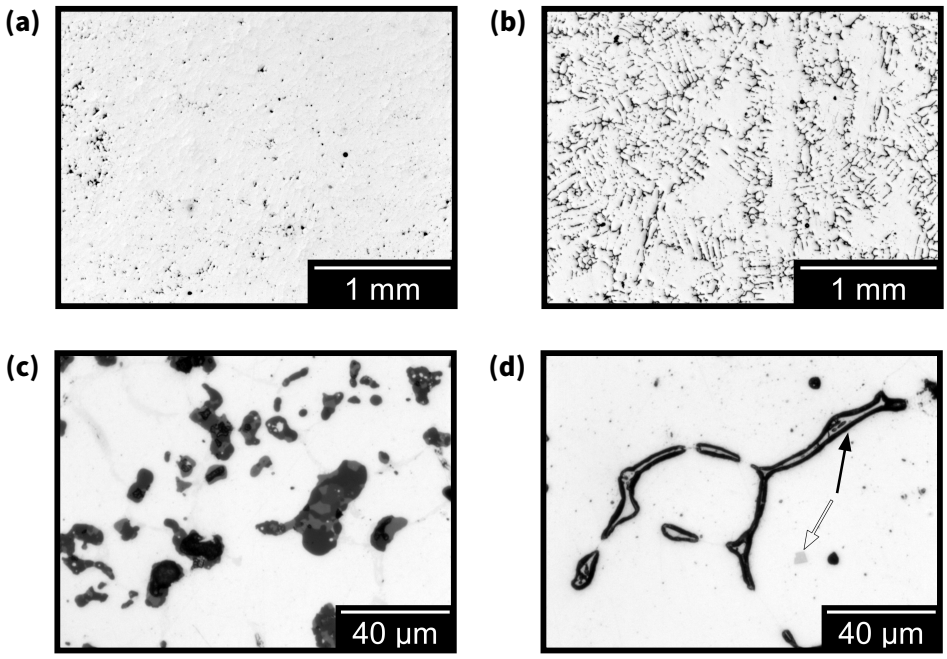

Figure 6.14.: TiB_2 particles (initial size 4 µm) in the middle of an iron matrix produced without magnetic field in (a,c) and in 3 T strong magnetic field for 45 minutes in (b,d). (a) and (b) show the difference of the matrix structure, (c) and (d) show zoomed-in middle of the matrix. Without cavitation strong particle clustering (black agglomerates in (c)) can be observed. With cavitation treatment single precipitates can be found throughout the matrix (marked with empty arrow) together with distinct grain boundaries (marked with solid arrow). Initial samples created with SPS.

Figure 6.15 shows results of TiB_2 particle (initial size 4 µm) dispersion in 1.4404 steel without (a) and with a 8 T large magnetic field (b). Without cavitation strong agglomeration of TiB_2 phase occurs and clusters as seen in (a) are found throughout the middle of the matrix. Applying 8 T magnetic field for 25 minutes is sufficient to destroy the particle clusters and disperse the TiB_2 precipitates (marked with empty arrows in (b)) in the matrix.

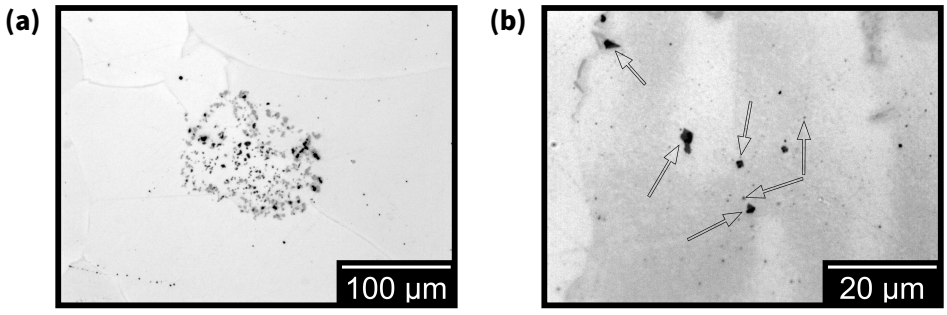

Figure 6.15.: TiB_2 particles (initial size 4 µm) in the middle of a steel matrix: produced without steady field (a) and in 8 T strong magnetic field for 25 minutes (b). Large particle clusters as in (a) are dispersed throughout the matrix. Processing with cavitation treatment leaves single precipitates (marked with empty arrows) in the middle of matrix (b). Initial samples created with SPS.

ZrB_2 is one of the ultra high temperature ceramics (melting point around 3000 °C) with a lower density than iron and steel, making it a good candidate for reinforcement. ZrB_2 particles (nominal size 5 µm) have been added to iron and processed using either 0.8 T or 4 T strong fields. Figure 6.16 (a) shows the resulting matrix with applying 0.8 T for 34 minutes. The low field experiment follows a similar pattern as the already described Zr-ceramics. Figure 6.16 (a) shows optical image of similar clusters situated at the top and bottom of the matrix as in Figure 6.6 (b) while the rest of the matrix is similar to Figure 6.6 (c). Applying stronger cavitation to the sample for the same processing time improves the dispersion – the clustering of (a) is avoided and single precipitates (the dark structures in (b)) can be observed inside the matrix. However, the obtained level of dispersion is worse than with other compounds making ZrB_2 less suitable for reinforcing heavy metals.

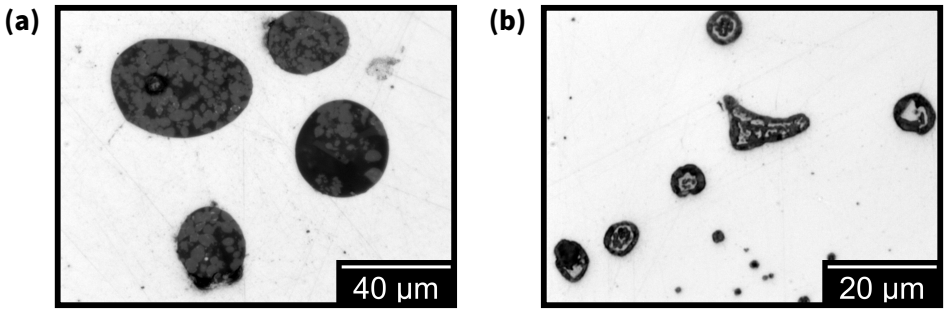

Figure 6.16.: ZrB_2 particles (nominal size 5 µm) in an iron matrix: samples obtained by processing in 0.8 T for 34 minutes in (a) and in 4 T for 34 minutes in (b). Large ZrB_2 agglomerates observable at the top in (a) in contrast with single precipitates in the middle in (b). Initial samples created without SPS.

Experiments have been conducted to investigate the dispersion of TiB_2 and ZrB_2 in nickel using 0.8 T strong field. The effect of applying cavitation treatment for 30 minutes follows a similar pattern as in experiments with TiC and ZrC. The results with TiB_2 and ZrB_2 are shown in Figure 6.17 (a) and (b). TiB_2 disperses better in nickel than TiC – more particles (marked with the empty arrows) can be found inside the matrix. Still, similar cavities as in Figure 6.12 (a) exist concentrating large amount of the reinforcement phase. ZrB_2 shows the same behavior as ZrC – it is completely pushed out of the matrix creating roughly the same 80 µm thick layer around the sample without any particle admixing.

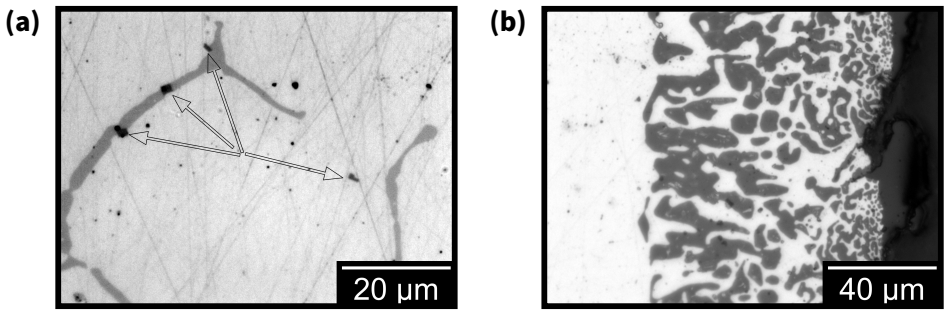

Figure 6.17.: TiB_2 particles (initial size 4 µm, marked with empty arrows) on a grain boundary and in the matrix in nickel (a). ZrB_2 particles (nominal size 4 µm) pushed to the side edge of a nickel matrix, creating a 80 µm thick layer around the sample. ZrB_2 micrograph taken at the right side. Both experiments conducted in 0.8 T magnetic field for 30 minutes. Initial samples created without SPS.

6.6. Synopsis about the particle dispersion in high melting point metals

Most oxide particles, i.e. TiO_2, Y_2O_3, CeO_2, show weak wettability and, therefore, weak dispersion. Yttria can be considered for future investigations because of particle agglomeration inside the 1.4404 steel matrix and, hence, stronger cavitation may improve the dispersion. On the other hand, TiO_2 and CeO_2 are clearly pushed to the edges of the metal matrix. While some ceria can be found inside, the amount is negligible compared with the amount pushed out. Al_2O_3 displays improved dispersion in steel and iron with an increased cavitation strength, while it is removed from the matrix in nickel. Lastly, ZrO_2 is completely rejected by 1.4404 steel matrix, however, good dispersion can be achieved in iron. It has been observed that alumina and zirconia are not thermodynamically stable during the cavitation treatment as traces of either liquefying or dissolving can be seen. However, the reaction taking place may have improved the wettability and consequently the dispersion of the precipitates.

Carbides exhibit excellent dispersion properties in iron and steel. While TiC can be distributed in iron even without cavitation treatment, applying sonication during the processing phase clearly shows a reduction of precipitate size. Similarly, ZrC shows improved distribution when stronger cavitation is used. On the other hand, TiC agglomerates in nickel and is weakly held by the matrix leaving large cavities during sample post-processing. Lastly, ZrC is completely rejected by the nickel matrix as it is pushed to the edges creating a shell around the sample.

From the nitrides group, dispersion of TiN into a 1.4404 steel matrix has been investigated. Similar to TiC, it is easily distributed without applying cavitation. Yet, a clear improvement in particle size can be observed as stronger cavitation reduces the size of the precipitates. However, stronger cavitation assists with a phase change from the cubic crystal (the initially inserted particles) to eutectic phase.

Borides show good dispersion properties, yet, it is possibly because of reactions taking place in iron and steel. Both TiB_2 and ZrB_2 can be dispersed and different cavitation

strengths influence the outcome. For example, no reaction of TiB_2 in iron can be observed, while with a strong sonication the microstructure is changed drastically – TiB_2 possibly transforms to TiC with the occurrence of Fe_2B phase. In 1.4404 steel high clustering can be observed without sonication. Strong cavitation prevents the agglomeration and TiB_2 precipitates are dispersed more evenly. ZrB_2 in iron exhibits similar properties as ZrC and ZrO_2 – the particles experience a phase change, yet, the agglomeration is reduced when cavitation is applied. TiB_2 particles are seemingly dispersible in a nickel matrix, however, preferably positioning on grain boundaries. On the other hand, ZrB_2 is completely removed from the nickel matrix and pushed to the edges of the sample.

A clear tendency can be observed by comparing the influence of melt treatment by no/low/high steady magnetic fields. It is clear that the cavitation created in a contactless way affects the particle dispersion. Even more, it has been demonstrated that a stronger cavitation, created by higher magnetic fields, disperses the reinforcements on a finer scale. In general, microparticles can be distributed in iron and 1.4404 steel, with the most promising ceramics being Ti- and Zr- compounds and Al_2O_3. In contrast, most of the reinforcements are rejected by the nickel matrix.

7. Summary and recommendations

7.1. Summary

Dispersion of ceramic particles into high melting point metals using a contactless magnetic treatment combines electrodynamics and magnetohydrodynamics, acoustics and signal processing, material processing and microstructure analysis. Here, a new investigative method for opaque fluids has been applied to study particle behaviour in liquid metals that additionally involves understanding of image processing and particle image velocimetry. The main aim of the present work is to further develop the contactless magnetic sonication in which pressure oscillations are created by a combination of suitable AC and DC magnetic fields, and to apply it to various particles and high temperature melts, such as steel, iron and nickel, in order to enable production of such metal matrix composites.

An approximation to describe the magnetic field distribution depending on the coil geometry in a semi-finite workpiece is developed. The simplified functions are then added to the Navier-Stokes equation to numerically obtain the basic flow in the system using the FEM solver in Mathematica 11.3. Furthermore, the oscillating force approximations allow to find the oscillating pressure amplitude distribution. The theoretical analysis shows that the obtainable peak pressure with the available DC magnets is barely sufficient for cavitation onset in heavy metals. Therefore, additional experiments have been carried in up to 8 T strong field in a superconducting magnet in the Dresden High Magnetic Field Laboratory (HLD) at HZDR. Lastly, the simplified formulas are used to describe the effect of the steady streaming and estimate the conditions when it has to be taken into account.

Neutron radiography has been employed to visualize the complex liquid metal two-phase flow similar to the one arising in the contactless cavitation set-up. Looking inside the liquid metal allows to get a better understanding about underlying phenomena that influence the particle dispersion. Two principal elements play the most important roles – wettability and flow characteristics. Firstly, it has been shown that non-wetted particles are impossible to admix in the liquid. To facilitate dispersion, a thin layer of liquid metal is mechanically applied to the particles. Secondly, even with significantly improved wetting a substantial flow rate (velocities in order of 100 mm s^{-1}) is required to draw the particles into the liquid metal because of the high terminal velocity of the inclusions.

Furthermore, visualization experiments of the liquid metal solidification and particle entrapment in a matrix have been conducted using neutron radiography. To track the solidification front, a simple algorithm based on PIV has been developed. Additionally, particle behaviour in the vicinity of the solidification front could be observed. A clear difference between two regimes has been noted – particles are not affected by a pure solidification front, while development of higher viscosity region highly increases the particle

entrapment rate. This allows to put forward a general hypothesis about prerequisites for successful reinforcement capturing. For introducing the particles into the melt the buoyancy has to be overcome which is enabled by high intensity stirring creating a turbulent flow ($Re > 10^4$). However, for the entrapment the particles have to be significantly slowed down which may happen in the higher viscosity zone. Still, these conditions are fulfilled only if the particles are well wetted by the liquid phase.

The principle of contactless cavitation treatment has been tested using the ultrasonic soldering approach – tin has successfully been joined with copper in the proposed set-up without any fluxing agents. As it is not possible to observe the cavitation directly, the sound emitted by multitude collapsing bubbles has been recorded and analyzed using multiple piezo elements. Such approach, while not giving full information about the cavitation, has demonstrated to be usable since the characteristic frequencies, i.e. sub- and ultraharmonics, are clearly distinguishable.

Different metals with different particles have been processed by superimposing various DC field strengths to the AC field during the induction melting process. It is shown that the magnetic field does not have to be large (~0.5 T) to reach the cavitation onset, even for steel and iron. Still, the response to the pressure oscillations is not consistent, and cannot be predicted. A high uncertainty about cavitation initiation has been observed – the same material with the same processing conditions creates cavitation in one case, but it may be absent in another. Furthermore, a higher amount of impurities in the initial sample provides a stronger cavitation response. Therefore, clearly the unmeasurable cavitation nuclei quantity plays the most important role – cavitation indeed is a measure of the purity of the liquid.

Cavitation treatment has a beneficial effect on the particle dispersion. Borides, carbides and nitrides can be well dispersed in iron and 1.4404 steel, and cavitation treatment reduces the agglomeration and breaks down the precipitates. However, relatively strong DC field (in order of 3 to 5 T) has to be applied for a noticeable effect. On the other hand, good particle distribution in nickel cannot be achieved. Oxides show mixed degree of dispersion – while some, e.g. CeO_2 or TiO_2, are completely rejected by the liquid, others, e.g. Al_2O_3 or ZrO_2, are kept in the matrix. In general, further research must be undertaken to get a comprehensive understanding of which particles from all the examined ones are the best candidates to be used as reinforcements in metal matrix composites.

7.2. Outlook

For contactless ultrasonic treatment to become a viable processing route, substantial further work is necessary. The basic research topics that have to be improved include material compatibility studies, cavitation measurement technique, adjustment of the procedure and the fundamental analytical description. After the knowledge has been improved, the focus can be shifted to assessing the feasibility of using the contactless treatment for improving other stages of metal manufacturing processes.

The first step of different material compatibility studies is straightforward – it is important to find such ceramics that are well wetted while at the same time do not react with the used liquid metal. Analysis and in-depth study of the available phase diagrams as well

as modelling the thermodynamic and phase properties using the Calphad (Calculation of phase diagrams) technique employing software can significantly narrow down the potential candidates. Still, experiments have to be conducted for validation. Regarding the matrix materials, first focus should be on testing iron and steel with an increased carbon content. Overall, it is reasonable to assume that the results obtained for iron and steel with Ti-, Zr and Al_2O_3 compounds are a good continuation point if the observed reactivity can be reduced. Furthermore, the used particle fraction is tiny compared to, e.g. high modulus steels. Therefore, it would be beneficial to add a higher amount of ceramics, even more if that can reduce the dissolved amount. As the wt% of ceramic is limited by the initial tablet production method (spark plasma sintering), in case of a higher fraction, insertion of particles remains an open issue.

Uncertainties exist regarding the recorded sound spectra and how exactly they relate to the cavitation activity and regimes as well as the oscillating pressure distribution inside the volume. Currently the understanding is based on two separate approaches. The oscillating pressure amplitude and topology can be calculated analytically using significant approximations in electromagnetics and fluid dynamics. On the other hand, the emitted sound by the cavitation activity is recorded, but it only provides basic information about the onset of the phenomenon. An important future milestone is to validate the simplified approach for finding pressure amplitude as well as to calibrate the piezo sensors. Essentially a basic, fundamental experiment has to be performed. If cavitation is applied to a low melting point metal, e.g. GaInSn, Sn or similar, it is possible to have a direct access to the melt. In such case a *cavitometer* can be employed, similar to [120], and oscillating pressure values can be directly measured and compared with the analytical solution. Furthermore, the signal recorded by the piezo sensors can be directly correlated with the actual pressure values in the melt, and this can then be used to estimate the cavitation activity in high melting point melts.

Regarding the overall procedure the presented approach needs to be improved as well. Most importantly, as solidification rate plays an important role regarding the final structure of the product as well as precipitation, it is of prime concern to control this process. Therefore, before continuation with composite production experiments with the same or similar set-up, a set of trials have to be performed to measure the solidification rate under different parameters with the metals in question. Furthermore, the knowledge about particle de- and reagglomaration is limited. The flow field is also increasingly damped at higher B_z possibly preventing particle homogenization. It is reasonable to investigate a periodic cavitation treatment – the steady magnetic field is applied periodically which gives maximum flow velocity to homogenize the volume as well as maximum separation force to disperse the particles in a successive manner. The question regarding particle de- and reagglomaration can also be further investigated in-situ in model experiments employing neutron radiography.

In general, as the creation of cavitation in a contacless way is proven to be achievable in high temperature melts other beneficial applications, such as ultrasonic degassing and structure refinement, can be explored. Eventually, a natural question about upscaling of the set-up arises. The current set-up is limited in size and not easy to upscale, yet the floating zone approach does not necessarily have to be used. Cavitation can be, without doubt, also produced in a dedicated crucible or employed during continuous casting.

The real limitations are the achievable field strengths – as it has been shown at 0.8 T is sufficient to get cavitation, but insufficient to affect the particle dispersion by a large extent. It is reasonable to state that around 3 T strong fields are necessary, which implies using superconducting magnets. Such room temperature open bore magnets can have a diameter of at least 300 mm, limiting the diameter of the workpiece to around 250 mm. Nevertheless, while the topic of contactless cavitation treatment of high temperature melts is just barely explored and some unknowns remain, it is reasonable to assume that the presented approach can be successfully employed to produce different composites. Whether that will facilitate a growth of steel composite market share remains to be seen.

Bibliography

[1] S. Rawal, "Metal-matrix composites for space applications," *The Journal of The Minerals, Metals and Materials Society*, vol. 53, no. 4, pp. 14–17, 2001.

[2] N. Chawla and K. K. Chawla, *Metal Matrix Composites*. Springer, New York, USA, 2013. ISBN: 9781461495482.

[3] A. Evans, C. S. Marchi, and A. Mortensen, *Metal Matrix Composites in Industry - An Introduction and a Survey*. Springer, Boston, USA, 2003. ISBN: 9781461504054.

[4] D. Miracle, "Metal matrix composites - from science to technological significance," *Composites Science and Technology*, vol. 65, no. 15-16, pp. 2526–2540, 2005.

[5] J. Kaczmar, K. Pietrzak, and W. Wlosiński, "Production and application of metal matrix composite materials," *Journal of Materials Processing Technology*, vol. 106, no. 1-3, pp. 58–67, 2000.

[6] Y. Yang, J. Lan, and X. Li, "Study on bulk aluminum matrix nano-composite fabricated by ultrasonic dispersion of nano-sized SiC particles in molten aluminum alloy," *Materials Science and Engineering A*, vol. 380, no. 1, pp. 378–383, 2004.

[7] G. Eskin and D. Eskin, *Ultrasonic Treatment of Light Alloy Melts*. CRC Press, Boca Raton, USA, 2015. ISBN: 9781466577992.

[8] A. Ferrari, "Fluid dynamics of acoustic and hydrodynamic cavitation in hydraulic power systems," *Proceedings of the Royal Society A: Mathematical, Physical and Engineering Sciences*, vol. 473, no. 2199, pp. 1–32, 2017. Art. no. 20160345.

[9] K. U. Kainer, *Metal Matrix Composites: Custom-made Materials for Automotive and Aerospace Engineering*. Wiley-VCH, Weinheim, Germany, 2006. ISBN: 9783527608270.

[10] J. Allison and G. Cole, "Metal-matrix composites in the automotive industry: Opportunities and challenges," *The Journal of The Minerals, Metals and Materials Society*, vol. 45, no. 1, pp. 19–24, 1993.

[11] N. Chawla and K. Chawla, "Metal-matrix composites in ground transportation," *The Journal of The Minerals, Metals and Materials Society*, vol. 58, no. 11, pp. 67–70, 2006.

[12] "Aluminum conductor composite reinforced technical notebook." `http://multimedia.3m.com/mws/media/5812680/electrical-markets.pdf`. Accessed 15.01.2019.

[13] C. Zweben, "Metal-matrix composites for electronic packaging," *The Journal of The Minerals, Metals and Materials Society*, vol. 44, no. 7, pp. 15–23, 1992.

[14] W. Harrigan, "Aluminum matrix composites 1970–2017," *Minerals, Metals and Materials Series*, no. 210809, pp. 3–18, 2018.

[15] H. Asanuma, "Development of metal-based smart composites," *The Journal of The Minerals, Metals and Materials Society*, vol. 52, no. 10, pp. 21–25, 2000.

[16] D. Mukhopadhyay, F. Froes, and D. Gelles, "Development of oxide dispersion strengthened ferritic steels for fusion," *Journal of Nuclear Materials*, vol. 258-263, no. Part 2, pp. 1209–1215, 1998.

[17] H. Springer, C. Baron, A. Szczepaniak, V. Uhlenwinkel, and D. Raabe, "Stiff, light, strong and ductile: nano-structured high modulus steel," *Scientific Reports*, vol. 7, no. 1, pp. 1–6, 2017. Art. no. 2757.

[18] I. Grants, G. Gerbeth, and A. Bojarevičs, "Contactless magnetic excitation of acoustic cavitation in liquid metals," *Journal of Applied Physics*, vol. 117, no. 20, pp. 1–7, 2015. Art. no. 204901.

[19] H. A. Hassan and J. J. Lewandowski, "Fracture toughness and fatigue of particulate metal matrix composites," in *Comprehensive Composite Materials II* (P. W. Beaumont and C. H. Zweben, eds.), vol. 4, pp. 86 – 136, Elsevier, Amsterdam, Netherlands, 2018. ISBN: 9780081005347.

[20] W. Miller and F. Humphreys, "Strengthening mechanisms in particulate metal matrix composites," *Scripta Metallurgica et Materiala*, vol. 25, no. 1, pp. 33–38, 1991.

[21] A. Mouritz, *Introduction to Aerospace Materials*. Woodhead Publishing Limited, Cambridge, UK, 2012. ISBN: 9780857095152.

[22] E. Mohammad Sharifi, F. Karimzadeh, and M. Enayati, "Fabrication and evaluation of mechanical and tribological properties of boron carbide reinforced aluminum matrix nanocomposites," *Materials and Design*, vol. 32, no. 6, pp. 3263–3271, 2011.

[23] T. Schubert, B. Trindade, T. Weißgärber, and B. Kieback, "Interfacial design of Cu-based composites prepared by powder metallurgy for heat sink applications," *Materials Science and Engineering A*, vol. 475, no. 1-2, pp. 39–44, 2008.

[24] S. Gorsse and D. Miracle, "Mechanical properties of Ti-6Al-4V/TiB composites with randomly oriented and aligned TiB reinforcements," *Acta Materialia*, vol. 51, no. 9, pp. 2427–2442, 2003.

[25] L.-Y. Chen, J.-Q. Xu, H. Choi, M. Pozuelo, X. Ma, S. Bhowmick, J.-M. Yang, S. Mathaudhu, and X.-C. Li, "Processing and properties of magnesium containing a dense uniform dispersion of nanoparticles," *Nature*, vol. 528, no. 7583, pp. 539–543, 2015.

[26] M. F. Ashby and E. M. Maine, "Design aspects of metal matrix composite usage," in *Comprehensive Composite Materials II* (P. W. Beaumont and C. H. Zweben, eds.), vol. 4, pp. 554 – 572, Elsevier, Amsterdam, Netherlands, 2018. ISBN: 9780081005347.

[27] K. Tanaka and T. Saito, "Phase equilibria in TiB_2-reinforced high modulus steel," *Journal of Phase Equilibria*, vol. 20, no. 3, pp. 207–214, 1999.

[28] C. Baron, H. Springer, and D. Raabe, "Effects of Mn additions on microstructure and properties of Fe–TiB_2 based high modulus steels," *Materials and Design*, vol. 111, pp. 185–191, 2016.

[29] T. Okuda and M. Fujiwara, "Dispersion behaviour of oxide particles in mechanically alloyed ODS steel," *Journal of Materials Science Letters*, vol. 14, no. 22, pp. 1600–1603, 1995.

[30] S. Ukai and M. Fujiwara, "Perspective of ODS alloys application in nuclear environments," *Journal of Nuclear Materials*, vol. 307-311, no. Part 1, pp. 749–757, 2002.

[31] F. Bergner, I. Hilger, J. Virta, J. Lagerbom, G. Gerbeth, S. Connolly, Z. Hong, P. Grant, and T. Weissgärber, "Alternative fabrication routes toward oxide-dispersion-strengthened steels and model alloys," *Metallurgical and Materials Transactions A: Physical Metallurgy and Materials Science*, vol. 47, no. 11, pp. 5313–5324, 2016.

[32] I. Gheorge and H. Rack, "Powder processing of metal matrix composites," in *Comprehensive Composite Materials* (A. Kelly and C. Zweben, eds.), vol. 3, pp. 679 – 700, Elsevier, Amsterdam, Netherlands, 2000. ISBN: 9780080429939.

[33] C. M. Cepeda-Jiménez and M. T. Pérez-Prado, "Processing of nanoparticulate metal matrix composites," in *Comprehensive Composite Materials II* (P. W. Beaumont and C. H. Zweben, eds.), vol. 4, pp. 313 – 330, Elsevier, Amsterdam, Netherlands, 2018. ISBN: 9780081005347.

[34] I. Ibrahim, F. Mohamed, and E. Lavernia, "Particulate reinforced metal matrix composites - a review," *Journal of Materials Science*, vol. 26, no. 5, pp. 1137–1156, 1991.

[35] A. Mortensen and I. Jin, "Solidification processing of metal matrix composites," *International Materials Reviews*, vol. 37, no. 1, pp. 101–128, 1992.

[36] M. Hasegawa and K. Takeshita, "Strengthening of steel by the method of spraying oxide particles into molten steel stream," *Metallurgical Transactions B*, vol. 9, no. 3, pp. 383–388, 1978.

[37] D. Eskin, I. Tzanakis, F. Wang, G. Lebon, T. Subroto, K. Pericleous, and J. Mi, "Fundamental studies of ultrasonic melt processing," *Ultrasonics Sonochemistry*, vol. 52, pp. 455–467, 2019.

[38] Y. Li and T. Zhou, "Achieving Al melt/carbon and Al-Ti melts/carbon interfaces wetting via ultrasonic couple processing," *Metallurgical and Materials Transactions A: Physical Metallurgy and Materials Science*, vol. 44, no. 7, pp. 3337–3343, 2013.

[39] A. Farmer, A. Collings, and G. Jameson, "Effect of ultrasound on surface cleaning of silica particles," *International Journal of Mineral Processing*, vol. 60, no. 2, pp. 101–113, 2000.

[40] O. Kudryashova and S. Vorozhtsov, "On the mechanism of ultrasound-driven deagglomeration of nanoparticle agglomerates in aluminum melt," *The Journal of The Minerals, Metals and Materials Society*, vol. 68, no. 5, pp. 1307–1311, 2016.

[41] T. Leighton, *The Acoustic Bubble*. Academic Press, London, UK, 1994. ISBN: 9780124419209.

[42] E. Neppiras, "Acoustic cavitation series: part one. Acoustic cavitation: an introduction," *Ultrasonics*, vol. 22, no. 1, pp. 25–28, 1984.

[43] E. Neppiras, "Acoustic cavitation," *Physics Reports*, vol. 61, no. 3, pp. 159–251, 1980.

[44] R. Apfel, "Acoustic cavitation," *Methods in Experimental Physics*, vol. 19, no. C, pp. 355–411, 1981.

[45] L. Crum, "Acoustic cavitation series: part five rectified diffusion," *Ultrasonics*, vol. 22, no. 5, pp. 215–223, 1984.

[46] M. Fitzgerald, V. Gripping, and J. Sullivan, "Chemical effects of ultrasonics-"hot spot" chemistry," *The Journal of Chemical Physics*, vol. 25, no. 5, pp. 926–933, 1956.

[47] K. Suslick, D. Hammerton, and R. Cline, "The sonochemical hot spot," *Journal of the American Chemical Society*, vol. 108, no. 18, pp. 5641–5642, 1986.

[48] K. Suslick, Y. Didenko, M. Fang, T. Hyeon, K. Kolbeck, W. McNamara III, M. Mdleleni, and M. Wong, "Acoustic cavitation and its chemical consequences," *Philosophical Transactions of the Royal Society A: Mathematical, Physical and Engineering Sciences*, vol. 357, no. 1751, pp. 335–353, 1999.

[49] I. Tzanakis, D. Eskin, A. Georgoulas, and D. Fytanidis, "Incubation pit analysis and calculation of the hydrodynamic impact pressure from the implosion of an acoustic cavitation bubble," *Ultrasonics Sonochemistry*, vol. 21, no. 2, pp. 866–878, 2014.

[50] J. Mi, D. Tan, and T. Lee, "In situ synchrotron x-ray study of ultrasound cavitation and its effect on solidification microstructures," *Metallurgical and Materials Transactions B: Process Metallurgy and Materials Processing Science*, vol. 46, no. 4, pp. 1615–1619, 2015.

[51] L. Montesano, A. Pola, M. Tocci, M. Gelfi, and G. La Vecchia, "Damaging of ultrasonic horn for semisolid feedstock production," *Solid State Phenomena*, vol. 285 SSP, pp. 240–246, 2019.

[52] D. Eskin and I. Tzanakis, "High-frequency vibration and ultrasonic processing," *Springer Series in Materials Science*, vol. 273, pp. 153–193, 2018.

[53] H. Yan, Z.-X. Huang, and H.-X. Qiu, "Microstructure and mechanical properties of CNTs/A356 nanocomposites fabricated by high-intensity ultrasonic processing," *Metallurgical and Materials Transactions A: Physical Metallurgy and Materials Science*, vol. 48, no. 2, pp. 910–918, 2017.

[54] M. Shen, X. Wang, C. Li, M. Zhang, X. Hu, M. Zheng, and K. Wu, "Effect of submicron size SiC particles on microstructure and mechanical properties of AZ31B magnesium matrix composites," *Materials and Design*, vol. 54, pp. 436–442, 2014.

[55] S. Lü, P. Xiao, S. Wu, and X. Fang, "Preparation and squeeze casting of nano-SiCP/A356 composite assisted with ultrasonic vibration process," *Materials Science Forum*, vol. 879, pp. 1188–1193, 2017.

[56] C. Chen, Z. Guo, J. Luo, W. Wang, and J. Hao, "Effects of ultrasonic treatment on microstructure and properties of Al-based composites reinforced by in situ Al_2O_3 nanoparticles," *High Temperature Materials and Processes*, vol. 35, no. 2, pp. 169–175, 2016.

[57] V. Meti, S. Shirur, J. Nampoothiri, K. Ravi, and I. Siddhalingeshwar, "Synthesis, characterization and mechanical properties of AA7075 based MMCs reinforced with TiB_2 particles processed through ultrasound assisted in-situ casting technique," *Transactions of the Indian Institute of Metals*, vol. 71, no. 4, pp. 841–848, 2018.

[58] Q. Gao, S. Wu, S. Lü, X. Xiong, R. Du, and P. An, "Improvement of particles distribution of in-situ 5 vol% TiB_2 particulates reinforced Al-4.5Cu alloy matrix composites with ultrasonic vibration treatment," *Journal of Alloys and Compounds*, vol. 692, pp. 1–9, 2017.

[59] P. Bhingole, G. Chaudhari, and S. Nath, "Processing, microstructure and properties of ultrasonically processed in situ MgO-Al_2O_3-$MgAl_2O_4$ dispersed magnesium alloy composites," *Composites Part A: Applied Science and Manufacturing*, vol. 66, pp. 209–217, 2014.

[60] M. Shen, R. Yang, M. Zhang, T. Ying, and K. Nie, "Effects of SiCp parameters on microstructures, interface structure and mechanical property of Mg bulk composites produced by ultrasonic vibration processing," *Transactions of the Indian Institute of Metals*, vol. 71, no. 6, pp. 1343–1350, 2018.

[61] X. Wang, N. Wang, L. Wang, X. Hu, K. Wu, Y. Wang, and Y. Huang, "Processing, microstructure and mechanical properties of micro-SiC particles reinforced magnesium matrix composites fabricated by stir casting assisted by ultrasonic treatment processing," *Materials and Design*, vol. 57, pp. 638–645, 2014.

[62] G. Eskin and D. Eskin, "Production of natural and synthesized aluminum-based composite materials with the aid of ultrasonic (cavitation) treatment of the melt," *Ultrasonics Sonochemistry*, vol. 10, no. 4-5, pp. 297–301, 2003.

[63] R. Harichandran and N. Selvakumar, "Effect of nano/micro B_4C particles on the mechanical properties of aluminium metal matrix composites fabricated by ultrasonic cavitation-assisted solidification process," *Archives of Civil and Mechanical Engineering*, vol. 16, no. 1, pp. 147–158, 2016.

[64] J. Lan, Y. Yang, and X. Li, "Microstructure and microhardness of SiC nanoparticles reinforced magnesium composites fabricated by ultrasonic method," *Materials Science and Engineering A*, vol. 386, no. 1-2, pp. 284–290, 2004.

[65] H. Choi, M. Jones, H. Konishi, and X. Li, "Effect of combined addition of Cu and aluminum oxide nanoparticles on mechanical properties and microstructure of Al-7Si-0.3Mg alloy," *Metallurgical and Materials Transactions A: Physical Metallurgy and Materials Science*, vol. 43, no. 2, pp. 738–746, 2012.

[66] E. Taberlet and Y. Fautrelle, "Turbulent stirring in an experimental induction furnace," *Journal of Fluid Mechanics*, vol. 159, pp. 409–431, 1985.

[67] T. Beinerts, A. Bojarevičs, I. Bucenieks, Y. Gelfgat, and I. Kaldre, "Use of permanent magnets in electromagnetic facilities for the treatment of aluminum alloys," *Metallurgical and Materials Transactions B: Process Metallurgy and Materials Processing Science*, vol. 47, no. 3, pp. 1626–1633, 2016.

[68] M. Ščepanskis, M. Sarma, P. Vontobel, P. Trtik, K. Thomsen, A. Jakovičs, and T. Beinerts, "Assessment of electromagnetic stirrer agitated liquid metal flows by dynamic neutron radiography," *Metallurgical and Materials Transactions B: Process Metallurgy and Materials Processing Science*, vol. 48, no. 2, pp. 1045–1054, 2017.

[69] C. Vivès, "Effects of forced electromagnetic vibrations during the solidification of aluminum alloys: Part I. solidification in the presence of crossed alternating electric fields and stationary magnetic fields," *Metallurgical and Materials Transactions B: Process Metallurgy and Materials Processing Science*, vol. 27, no. 3, pp. 445–455, 1996.

[70] J. B. Wilgen, R. A. Kisner, G. M. Ludtka, G. M. Ludtka, and R. Jaramillo, "High magnetic field ohmically decoupled non-contact technology," May 2009. Patent No. US7534980B2.

[71] R. A. Kisner, O. Rios, A. M. Mellin, G. M. Ludtka, G. M. Ludtka, and J. B. Wilgen, "EMAT enhanced dispersion of particles in liquid," November 2016. Patent No. US9504973B2.

[72] V. Bojarevics, G. Djambazov, and K. Pericleous, "Contactless ultrasound generation in a crucible," *Metallurgical and Materials Transactions A: Physical Metallurgy and Materials Science*, vol. 46, no. 7, pp. 2884–2892, 2015.

[73] J. Davies, *Conduction and Induction Heating*. Energy Engineering Series, Peter Peregrinus Limited, London, UK, 1990. ISBN: 9780863411748.

[74] M. Kennedy, *Magnetic Fields and Induced Power in the Induction Heating of Aluminium Billets*. KTH Royal Institute of Technology, Stockholm, Sweden, Licentiate dissertation, 2013.

[75] I. Grants and G. Gerbeth, "Stability of melt flow during magnetic sonication in a floating zone configuration," *Physical Review Fluids*, vol. 3, no. 6, pp. 1–14, 2018. Art. no. 063902.

[76] J. J. Valencia and P. N. Quested, "Thermophysical properties," in *Casting (ASM Handbook Vol. 15)*, pp. 468–481, ASM International, Materials Park, USA, 2008. ISBN: 9780871707116.

[77] C. Ho and T. Chu, "Electrical resistivity and thermal conductivity of nine selected AISI stainless steels," pp. 1–50, Thermophysical and Electronic Properties Information Analysis Center, West Lafayette, USA, 1977. Report no. 45.

[78] I. Tzanakis, G. Lebon, D. Eskin, and K. Pericleous, "Characterisation of the ultrasonic acoustic spectrum and pressure field in aluminium melt with an advanced cavitometer," *Journal of Materials Processing Technology*, vol. 229, pp. 582–586, 2016.

[79] H. Peng, Y. Wang, R. Jiang, X. Li, R. Li, and L. Zhang, "Numerical simulation of ultrasonic field within the large-scale Al alloy melts treated by scalable sonotrodes," *AIP Advances*, vol. 9, no. 9, pp. 1–9, 2019. Art. no. 095015.

[80] C. E. Brennen, *Cavitation and Bubble Dynamics*. Cambridge University Press, Cambridge, UK, 2013. ISBN: 9781107338760.

[81] D. Shu, B. Sun, J. Mi, and P. Grant, "A high-speed imaging and modeling study of dendrite fragmentation caused by ultrasonic cavitation," *Metallurgical and Materials Transactions A: Physical Metallurgy and Materials Science*, vol. 43, no. 10, pp. 3755–3766, 2012.

[82] I. Tzanakis, W. Xu, D. Eskin, P. Lee, and N. Kotsovinos, "In situ observation and analysis of ultrasonic capillary effect in molten aluminium," *Ultrasonics Sonochemistry*, vol. 27, pp. 72–80, 2015.

[83] L. Xiaochun, Y. Yang, and D. Weiss, "Theoretical and experimental study on ultrasonic dispersion of nanoparticles for strengthening cast aluminum alloy A356," *Metallurgical science and technology*, vol. 26, no. 2, pp. 12–20, 2008.

[84] E. Brandes and G. Brook, *Smithells Metals Reference Book: Seventh Edition*. Butterworth-Heinemann, Oxford, UK, 1992. ISBN: 0750636246.

[85] L. Jordan and J. Eckman, "Determination of oxygen and hydrogen in metals by fusion in vacuum," *Industrial and Engineering Chemistry*, vol. 18, no. 3, pp. 279–282, 1926.

[86] K.-S. Im, K. Fezzaa, Y. J. Wang, X. Liu, J. Wang, and M.-C. Lai, "Particle tracking velocimetry using fast x-ray phase-contrast imaging," *Applied Physics Letters*, vol. 90, no. 9, pp. 1–3, 2007. Art. no. 091919.

[87] S.-J. Lee and G.-B. Kim, "X-ray particle image velocimetry for measuring quantitative flow information inside opaque objects," *Journal of Applied Physics*, vol. 94, no. 5, pp. 3620–3623, 2003.

[88] E. Lehmann, P. Vontobel, and L. Wiezel, "Properties of the radiography facility NEUTRA at SINQ and its potential for use as european reference facility," *Nondestructive Testing and Evaluation*, vol. 16, no. 2-6, pp. 191–202, 2001.

[89] M. Ščepanskis, R. Nikoluškins, A. Bojarevičs, T. Beinerts, V. Geža, A. Jakovičs, and K. Thomsen, "Liquid metal flow induced by counterrotating permanent magnets in rectangular crucible," in *Proceedings of the 11th International PAMIR Conference on Fundamental and Applied MHD, Riga, Latvia*, vol. 1, pp. 278–282, 2014.

[90] A.-E. Sommer, M. Nikpay, S. Heitkam, M. Rudolph, and K. Eckert, "A novel method for measuring flotation recovery by means of 4 D particle tracking velocimetry," *Minerals Engineering*, vol. 124, pp. 116–122, 2018.

[91] T. Lappan, M. Sarma, S. Heitkam, P. Trtik, D. Mannes, K. Eckert, and S. Eckert, "Neutron radiography of particle-laden liquid metal flow driven by an electromagnetic induction pump," *Magnetohydrodynamics*, vol. 56, no. 2-3, pp. 167–176, 2020.

[92] Y. Plevachuk, V. Sklyarchuk, S. Eckert, G. Gerbeth, and R. Novakovic, "Thermophysical properties of the liquid Ga-In-Sn eutectic alloy," *Journal of Chemical and Engineering Data*, vol. 59, no. 3, pp. 757–763, 2014.

[93] A. Cramer, C. Zhang, and S. Eckert, "Local flow structures in liquid metals measured by ultrasonic doppler velocimetry," *Flow Measurement and Instrumentation*, vol. 15, no. 3, pp. 145–153, 2004.

[94] S. Eckert and G. Gerbeth, "Velocity measurements in liquid sodium by means of ultrasound doppler velocimetry," *Experiments in Fluids*, vol. 32, no. 5, pp. 542–546, 2002.

[95] M. Kirpo, A. Jakovičs, E. Baake, and B. Nacke, "Analysis of experimental and simulation data for the liquid metal flow in a cylindrical vessel," *Magnetohydrodynamics*, vol. 43, no. 2, pp. 161–172, 2007.

[96] D. Musaeva, E. Baake, A. Köppen, and P. Vontobel, "Application of neutron radiography for in-situ visualization of gallium solidification in travelling magnetic field," *Magnetohydrodynamics*, vol. 53, no. 3, pp. 583–593, 2017.

[97] B. Willers, S. Eckert, U. Michel, I. Haase, and G. Zouhar, "The columnar-to-equiaxed transition in Pb-Sn alloys affected by electromagnetically driven convection," *Materials Science and Engineering A*, vol. 402, no. 1-2, pp. 55–65, 2005.

[98] L. Ramqvist, "Wetting of metallic carbides by liquid copper, nickel, cobalt and iron," *Int. J. Powder Met.*, vol. 1, no. 4, pp. 2–21, 1965.

[99] G. Yasinskaya, "The wetting of refractory carbides, borides, and nitrides by molten metals," *Soviet Powder Metallurgy and Metal Ceramics*, vol. 5, no. 7, pp. 557–559, 1966.

[100] A. Amadeh, S. Heshmati-Manesh, J. Labbe, A. Laimeche, and P. Quintard, "Wettability and corrosion of TiN, TiN-BN and TiN-AlN by liquid steel," *Journal of the European Ceramic Society*, vol. 21, no. 3, pp. 277–282, 2001.

[101] C. Xuan, K. Nakajima, H. Shibata, and P. Jönsson, "Wetting and spreading behavior of liquid iron on single crystal TiO_2 substrate," *Materials Letters*, vol. 258, pp. 1–4, 2020. Art. no. 126778.

[102] C. Xuan, H. Shibata, S. Sukenaga, P. Jönsson, and K. Nakajima, "Wettability of Al_2O_3, MgO and Ti_2O_3 by liquid iron and steel," *ISIJ International*, vol. 55, no. 9, pp. 1882–1890, 2015.

[103] C. Xuan, H. Shibata, Z. Zhao, P. Jönsson, and K. Nakajima, "Wettability of TiN by liquid iron and steel," *ISIJ International*, vol. 55, no. 8, pp. 1642–1651, 2015.

[104] Z. Amondarain, L. Kolbeinsen, and J. Arana, "Wetting behavior of sintered nanocrystalline powders by armco Fe and 22CrNiMoV_5-3 steel grade using sessile drop wettability technique," *ISIJ International*, vol. 51, no. 5, pp. 733–742, 2011.

[105] B. Terry and O. Chinyamakobvu, "Dispersion and reaction of TiC in liquid iron alloys," *Materials Science and Technology*, vol. 8, no. 5, pp. 399–405, 1992.

[106] T. Kattamis and T. Suganuma, "Solidification processing and tribological behavior of particulate TiC-ferrous matrix composites," *Materials Science and Engineering A*, vol. 128, no. 2, pp. 241–252, 1990.

[107] B. Terry and O. Chinyamakobvu, "Dispersion and reaction of TiB_2 in liquid iron alloys," *Materials Science and Technology*, vol. 8, no. 6, pp. 491–499, 1992.

[108] A. Szczepaniak, H. Springer, R. Aparicio-Fernández, C. Baron, and D. Raabe, "Strengthening Fe – TiB_2 based high modulus steels by precipitations," *Materials and Design*, vol. 124, pp. 183–193, 2017.

[109] I. Tzanakis, G. Lebon, D. Eskin, and K. Pericleous, "Characterizing the cavitation development and acoustic spectrum in various liquids," *Ultrasonics Sonochemistry*, vol. 34, pp. 651–662, 2017.

[110] J. Song, K. Johansen, and P. Prentice, "An analysis of the acoustic cavitation noise spectrum: The role of periodic shock waves," *Journal of the Acoustical Society of America*, vol. 140, no. 4, pp. 2494–2505, 2016.

[111] E. Cramer and W. Lauterborn, "Acoustic cavitation noise spectra," *Applied Scientific Research*, vol. 38, no. 1, pp. 209–214, 1982.

[112] V. Ilyichev, V. Koretz, and N. Melnikov, "Spectral characteristics of acoustic cavitation," *Ultrasonics*, vol. 27, no. 6, pp. 357–361, 1989.

[113] "WACKER AK 35 linear silicone fluids." `https://www.wacker.com/h/en-us/medias/WACKER-AK-35-en-2019.11.05.pdf`. Accessed 15.12.2019.

[114] P. Vianco, F. Hosking, and J. Rejent, "Ultrasonic soldering for structural and electronic applications: Fundamental experiments and two case studies illustrate the feasibility of ultrasonic activation for fluxless solder processing," *Welding Journal*, vol. 75, no. 11, pp. 343–355, 1996.

[115] K. Verhiest, S. Mullens, J. Paul, I. De Graeve, N. De Wispelaere, S. Claessens, A. Debremaecker, and K. Verbeken, "Experimental study on the contact angle formation of solidified iron-chromium droplets onto yttria ceramic substrates for the yttria/ferrous alloy system with variable chromium content," *Ceramics International*, vol. 40, no. 1, Part B, pp. 2187–2200, 2014.

[116] J. V. Naidich, "The wettability of solids by liquid metals," in *Progress in surface and membrane science* (D. Cadenhead and J. Danielli, eds.), vol. 14, pp. 353–484, Academic Press, New York, USA, 1981. ISBN: 9781483219790.

[117] H. Springer, R. Aparicio Fernandez, M. Duarte, A. Kostka, and D. Raabe, "Microstructure refinement for high modulus in-situ metal matrix composite steels via controlled solidification of the system Fe-TiB_2," *Acta Materialia*, vol. 96, pp. 47–56, 2015.

[118] P. Ghosh, C. Ghosh, and R. Ray, "Precipitation in interstitial free high strength steels," *ISIJ International*, vol. 49, no. 7, pp. 1080–1086, 2009.

[119] C. Wang, H. Gao, Y. Dai, X. Ruan, J. Shen, J. Wang, and B. Sun, "In-situ technique for synthesizing Fe-TiN composites," *Journal of Alloys and Compounds*, vol. 490, no. 1-2, pp. L9–L11, 2010.

[120] I. Tzanakis, M. Hodnett, G. Lebon, N. Dezhkunov, and D. Eskin, "Calibration and performance assessment of an innovative high-temperature cavitometer," *Sensors and Actuators, A: Physical*, vol. 240, pp. 57–69, 2016.

List of publications

Journal articles

T. Lappan, M. Sarma, S. Heitkam, P. Trtik, D. Mannes, K. Eckert, and S. Eckert, "Neutron radiography of particle-laden liquid metal flow driven by an electromagnetic induction pump," *Magnetohydrodynamics*, vol. 56, no. 2-3, pp. 167–176, 2020. DOI: 10.22364/mhd.56.2-3.8

R. Baranovskis, M. Sarma, M. Ščepanskis, T. Beinerts, A. Gaile, S. Eckert, D. Räbiger, E.H. Lehmann, K. Thomsen, and P. Trtik, "Investigation of particle dynamics and solidification in two-phase system by neutron radiography," *Magnetohydrodynamics*, vol. 56, no. 1, pp. 43-50, 2020. DOI: 10.22364/mhd.56.1.4

S. Heitkam, M. Rudolph, T. Lappan, M. Sarma, S. Eckert, P. Trtik, E. Lehmann, P. Vontobel, and K. Eckert, "Neutron imaging of froth structure and particle motion," *Minerals Engineering*, vol. 119, pp. 126-129, 2018. DOI: 10.1016/j.mineng.2018.01.021

M. Sarma, I. Grants, A. Bojarevics, and G. Gerbeth, "Magnetically induced cavitation for the dispersion of particles in liquid metals," in *Metal-Matrix Composites Innovations, Advances and Applications* (T. Srivatsan, Y. Zhang and W. Harrigan, eds), *The Minerals, Metals and Materials Series*, pp. 183-192, 2018. DOI: 10.1007/978-3-319-72853-7_ 12

M. Sarma, I. Grants, I. Kaldre, A. Bojarevics, and G. Gerbeth, "Casting technology for ODS steels - dispersion of nanoparticles in liquid metals," *IOP Conference Series: Materials Science and Engineering*, vol. 228, art. no. 012020, 2017. DOI: 10.1088/1757-899X/228/1/012020

M. Ščepanskis, M. Sarma, P. Vontobel, P. Trtik, K. Thomsen, A. Jakovics, and T. Beinerts, "Assessment of electromagnetic stirrer agitated liquid metal flows by dynamic neutron radiography," *Metallurgical and Materials Transactions B: Process Metallurgy and Materials Processing Science*, vol. 48, no. 2, pp. 1045-1054, 2017. DOI: 10.1007/s11663-016-0902-8

V. Dzelme, M. Ščepanskis, V. Geža, A. Jakovičs, and M. Sarma, "Modelling of liquid metal stirring induced by four counter-rotating permanent magnets," *Magnetohydrodynamics*, vol. 52, no. 4, pp. 461-470, 2016.

M. Sarma, M. Ščepanskis, A. Jakovičs, K. Thomsen, R. Nikoluškins, P. Vontobel, T. Beinerts, A. Bojarevičs, and E. Platacis, "Neutron radiography visualization of solid particles in stirring liquid metal," *Physics Procedia*, vol. 69, pp. 457-463, 2015. DOI: 10.1016/j.phpro.2015.07.064

M. Ščepanskis, M. Sarma, R. Nikoluškins, K. Thomsen, A. Jakovičs, P. Vontobel, T. Beinerts, A. Bojarevičs, and E. Platacis, "A report on the first neutron radiography experiment for dynamic visualization of solid particles in an intense liquid metal flow," *Magnetohydrodynamics*, vol. 51, no. 2, pp. 257-265, 2015.

Conference papers

M. Sarma, I. Grants, A. Bojarevics, and G. Gerbeth, "Magnetically induced cavitation for the dispersion of particles in liquid metals," *TMS2018 Metal-Matrix Composites Innovations, Advances and Applications: An SMD Symposium in Honor of William C. Harrigan, Jr.* in Phoenix (USA), March 11-15, 2018.

M. Sarma, G. Gerbeth, I. Grants, I. Kaldre, and A. Bojarevics, "Magnetically induced cavitation for the dispersion of nanoparticles in liquid metals," *XVIII International UIE-Congress on Electrotechnologies for Material Processing* in Hannover (Germany), June 6-9, 2017.

M. Sarma, S. Miran, I. Grants, and G. Gerbeth, "Dispersion of nanoparticles in steel melt by superimposed steady and alternating magnetic fields," *International Conference on Heating by Electromagnetic Sources HES-16* in Padova (Italy), May 24-27, 2016.